STATIONARY DIGITAL TOMOSYNTHESIS: IMPLEMENTATION, CHARACTERIZATION, AND IMAGE PROCESSING TECHNIQUES

Christina R. Inscoe

A dissertation submitted to the faculty at the University of North Carolina at Chapel Hill in partial fulfillment of the requirements for the degree of Doctor of Philosophy in the Department of Applied Physical Sciences in the College of Arts and Sciences.

Chapel Hill
2018

Approved by:

Otto Zhou

Jianping Lu

Yueh Lee

David Lalush

Richard Superfine

ABSTRACT

Christina R. Inscoe: Stationary digital tomosynthesis: implementation, characterization, and image processing techniques
(Under the direction of Otto Zhou)

The use of carbon nanotube cathodes for x-ray generation was pioneered and perfected by our team in the Applied Nanotechnology Laboratory at the University of North Carolina at Chapel Hill. Over the past decade, carbon nanotube (CNT) x-ray source technology has matured and translated into multiple pre-clinical and clinical devices. One prominent implementation of CNT x-ray technology is called tomosynthesis. The purpose of this project is to develop and characterize the latest iteration, stationary intraoral tomosynthesis, and develop a low-dose, scatter reduction technique for breast and chest tomosynthesis.

The first portion of this project was to develop and evaluate a new quasi-3D imaging modality for dental imaging. My work consists of experiments which dictated the design parameters and subsequent system evaluation of the dedicated s-IOT clinical prototype system currently installed in the UNC Department of Oral and Maxillofacial Radiology. Experiments were performed to determine optimal source array geometry and system configuration. The system was fabricated by our commercial partner then housed in our research lab for characterization and software development. After installation in the SOD, I performed additional system characterization. Four pre-clinical imaging studies have been performed in collaboration with several dentists using phantoms, extracted teeth, and cadaveric dentition. The system has now been vetted and is ready for patient use.

The second portion of this project consists of development of an image processing technique for scatter correction. The primary sampling scatter correction (PSSC) is a beam pass technique to measure the primary transmission through the patient and calculate the scatter profile for subtraction. Though developed for breast and chest tomosynthesis, utilization in mammography and chest radiography are also demonstrated in this project.

This dissertation is composed of five chapters. Chapters one and two provide the basics of x-ray generation and evolution of carbon nanotube x-ray source technology in our lab at UNC. Chapter three focuses on stationary intraoral tomosynthesis. The first section provides background information on dental radiology and project motivation. Sections 3.2 and 3.3 detail my work. Chapter four introduces scatter, providing motivation for the primary sampling scatter correction (PSSC) image processing method, detailed in chapter five.

For HHR

ACKNOWLEDGEMENTS

The work presented in this thesis provides only a glimpse into the accomplishments and capabilities of our research team at UNC. I have been honored to participate in the development of the CNT x-ray source evolution, made possible by my boss and mentor, Dr. Otto Zhou. Dr. Zhou invited me to join the team as his laboratory manager in 2006. Being both a full-time staff employee of UNC and graduate student afforded excellent on-the-job training. Dr. Zhou is an amazing scientist with great business sense, only exceeded by his kindness and humility. I would like to thank Dr. Zhou. It is because of him that I have been able to complete this thesis work while concurrently helping to run our lab and raising a family.

Dr. Jianping Lu has also served as my mentor, guiding me through research on all fronts, particularly in the scatter correction portion of this thesis. Dr. Lu provides invaluable feedback and expertise on computation, mathematics, physics, and simulations. Because I am an experimentalist at heart, with tendencies to measure or build, Dr. Lu's strong theoretical physics background provides a complementary counterweight with which we sometimes actually start with a simulation. I would like to thank Dr. Lu for being a wonderful mentor and an irreplaceable part of this thesis work.

Dr. Yueh Lee, faculty in Radiology, has been a major influence on the clinical direction of our research lab since his days as a medical student. Our relationship with him has enabled the development of stationary breast and chest imaging with human trials. Dr. Lee has most recently pushed the development of an orthopedic imaging system and enabled our first

musculoskeletal reader study. His depth and breadth of knowledge of medical devices and radiological applications allows him to provide us with clinically relevant applications. He has helped me with so many tasks in and out of the lab and out of the scope of this thesis. Regarding thesis work, he has become increasingly involved in the scatter correction portion of the project and is working to secure funding for clinical exploration. He has written an IACUC protocol for the porcine imaging and used his connections to gain access to the animal used in chapter 5. Dr. Lee brings many things to the table, but perhaps the most important is the attitude that there are many more things to explore and the sky is the limit. I would like to thank Dr. Lee for all of his contributions.

I would like to thank Dr. David Lalush for participating on the committee and giving me a strong footing in medical imaging in his course over a decade ago. The textbook is tattered, as I still reference it frequently. Dr. Lalush is an imaging expert and has provided constructive feedback on this dissertation. I hope we will find a project for future collaboration.

I would like to thank Dr. Richard Superfine for agreeing to participate on this thesis committee and ensuring the credibility of this thesis work. As the outsider to our standard committee roster, Dr. Superfine required convincing of the quality and nature of my work. Because of him, I worked harder and generated more results to include in this project. Dr. Superfine also serves as the chair of the Department of Applied Physical Sciences and driving force behind the Be A Maker spaces on campus, one of which I have used for fabricating research devices.

There are many past and present members of our research group that I wish to thank for contributing not only to this work, but to the body of knowledge I have acquired as a scientist.

Connor Puett, Taylor Gunnell, Soha Bazyar, Alex Billingsley, and Harrison Jacobs currently comprise our small, but mighty group, arguably one of the best we have ever had. Gongting Wu, Andrew Tucker, and Jing Shan are former students who contributed to the scatter correction portion of this thesis. Many other students have passed through our lab over the years and I have worked alongside most and learned from every one of them: Laurel Burk, Xiomara Calderón-Colón, Jabari Calliste, Guohua Cao, Pavel Chtcheprov, Rachel Ger, Emily Gidcumb, Allison Hartman, Sherry Leeper, Zhijun Liu, Matthew McIntosh, Tuyen Phan, Alexander Primmesnig, Xin Qian, Ramya Rajaram, Danae Eleni Souliouti, Shabana Sultana, Satoshi Tomo, Peng Wang, Sigen Wang, Guang Yang, Jian Zhang, and Lei Zhang.

The dental portion of this thesis work, and perhaps the s-IOT project itself, would not have occurred without the involvement of our wonderful collaborators in the UNC School of Dentistry, whom I wish to thank. Dr. Enrique Platin is a wonderful person and his ideas and enthusiasm for s-IOT have been the driving force behind our translation into his clinic. Dr. Andre Mol has provided his expertise in the conception and development of s-IOT. Dr. Angela Broome has taken on the daunting task of Principal Investigator and has worked tirelessly to ensure success of our patient study. Dr. Lars Gaalass, formerly of UNC SOD, currently at UMN, assisted in the conception and has ongoing interest and applications for s-IOT. He and Dr. Michael Regan Anderson (UMN) have provided root fracture samples that are helping to clarify the clinical utility of the s-IOT. Each of these dentists has been an indispensable part of our collaboration.

Throughout my time in the research lab, we have collaborated with several corporate partners. Most recently, the team at XinVivo has built the s-IOT system presented in chapter 3. Andrew Tucker is the project manager and a former student of our group. Tim Capo, Jesse

Dean, and Juliana Burney have worked tirelessly to fabricate the final clinical prototype system. I would also like to thank our collaborators at Carestream Health and Hologic. Brian McElroy of Hologic has been particularly helpful in diagnosis and repair of our breast imaging systems.

I would like to thank the funding agencies involved in this work. The dental project was supported by the Improving Human Health Awards from the NCTraCS which is the academic home of the NIH Clinical and Translational Science Award (CTSA) at UNC (Grant #IHHAR21506), and by XinVivo. The scatter correction project was supported by the Center for Cancer Nanotechnology Excellence at UNC which was funded by the National Cancer Institute under grant number U54CA119343.

I would also like to thank Ms. Heather Moser of the UNC Mammography Department for her assistance in acquiring the FFDM images

The Radiation Safety Division of the Department of Environment, Health, and Safety has been an incredible help in this thesis work as well as in my role as lab manager. Mark Brueckner, Bradford Taylor, Steve Guarino, Aaron Gunsales, and Mike Soles have all contributed to the success of our lab. The collaborative nature of our relationship has ensured a safe and compliant research atmosphere. Their assistance with dosimetric characterizations of our systems is not always part of their job, but they are willing to assist above and beyond the call of duty. I would like to thank all of them, particularly Mark Brueckner.

The Physics Instrument Shop has fabricated devices for this project and every other project I have worked on since coming to UNC. I wish to thank them, as their expertise, professionalism, and friendship have been priceless.

I would like to thank Dr. Sean Washburn and Dr. Nalin Parikh for encouraging my work since the very beginning. Their support and guidance has made the culmination of this thesis work a little easier.

Dr. Duane Deardorff hired me as lab manager in the UNC Department of Physics and Astronomy in 2002 and graciously allowed me to transition to research when the opportunity arose. I would like to thank Duane, without his involvement, I may never have come to UNC or finished a PhD.

Dr. Andrew Graham was my mentor and friend in my days as an undergraduate at Appalachian State University. He gave me my first job in the Physics Department and taught me countless phenomena and a true love of experimental physics. Though he created a job to keep me at ASU, he told me of a job at Elon, which I would eventually take, then later gave my name to Duane. Much like myself, he completed his PhD at a later stage in life, and was a huge Tarheel fan. Andy passed away due to a brain tumor in 2008, but would have enjoyed seeing me reach this point. I am thankful for all he has done for me.

I would also like to thank Dr. Joseph Pollock and Dr. Marian Peters, who were also large influences from ASU. Their support and encouragement steered me through my bachelor's degree.

My parents, Mike and Nancy, have supported me throughout my long and illustrious career as a student. It is with their strength, perseverance, and ingenuity that I balance the demands of work, school, and family. Thank you for teaching me that anything is possible.

Finally, I would like to thank my husband, Kevin, and my children, Ashley and Connor, who have tried their best to give me the space and free time to complete this dissertation and

thesis work. Though the children do not quite grasp the magnitude of this undertaking now, my hope is that it will seem achievable when their time comes. For them I try to set a good example and instill the value of education. They also serve as a constant reminder of the importance of time management, as life goes on despite your deadlines.

PREFACE

This purpose of this work is to provide a review of the evolution of carbon nanotube x-ray source development over the past decade, including my own personal contributions to this success story. My role as lab manager in the Applied Nanotechnology Laboratory has allowed me the unique opportunity to participate in this process from perfection of the cathode deposition process to system integration and human clinical trials. Many of my scientific contributions have been incorporated into student research projects and publications over the years, with some of the more humble students privately crediting me for as much as half of their PhD. Experience in this supporting role has taught me more about instrumentation, imaging, and troubleshooting than any coursework I have completed. The interdisciplinary nature of our work means students, including myself, rarely come to the table with all of the tools and experience needed to complete their project. As we have charted new territory in medical imaging and radiotherapy, technical and regulatory issues have arisen for which there is no clear answer. Facing these challenges has forced me to develop a broad skillset with which I can now rise to any occasion in the laboratory environment.

TABLE OF CONTENTS

LIST OF TABLES

LIST OF FIGURES

LIST OF ABBREVIATIONS

2D: Two-dimensional

3D: Three-dimensional

ACR: American College of Radiology

ADS-POCS: Adaptive steepest descent projection onto convex sets

AEC: Automatic exposure control

ALARA: As low as reasonably achievable

BR3D: Breast radiography three-dimensional

BRIC: Biomedical Research Imaging Center

C: Contrast

CAD: Computer-aided design

CBCT: Cone beam computed tomography

CCD: Charged coupled devices

CIRS: Computerized Imaging Reference Systems

CMOS: Complementary metal oxide semiconductor

CNT: Carbon nanotube

CT: Computed tomography

DCT: Digital chest tomosynthesis

DQE: Detective quantum efficiency

DXTTR: Dental x-ray teaching and training replica

EHS: Environment, Health, and Safety

FDA: Food and Drug Administration

FFDM: Full field digital mammography

FOV: Field of view

f-SPR: Filtered scatter-to-primary ratio

FW15%: Full-width-fifteen percent

FWHM: Full-width-half-max

GE: General Electric

GPU: Graphical processing unit

HVL: Half-value layer

I: Intensity

μ-CT: Micro computed tomography

MC: Monte Carlo

MTF: Modulation transfer function

MWNT: Multi-walled nanotube

NIST: National Institute of Standards and Technology

P: Primary

PC: Personal computer

PhD: Doctor of philisophy

PSD: Primary sampling device

PSP: Photostimulable phosphor plate

PSSC: Primary sampling scatter correction

QA: Quality assurance

ROI: Region of interest

RMI: Radiation Measurements, Inc.

S: Scatter

SART: Simultaneous algebraic reconstruction technique

s-DBT: Stationary digital breast tomosynthesis

s-DCT: Stationary digital chest tomosynthesis

SDD: Source-detector distance

SdNR: Signal difference-to-noise ratio

s-DOT: Stationary digital orthopedic tomosynthesis

SI: Scatter interpolation

SID: Source-to-image distance

SNR: Signal-to-noise ratio

SOD: School of Dentistry; Source-to-object distance

SOP: Standard operating procedure

SPR: Scatter-to-primary ratio

SWNT: Single walled nanotube

s-IOT: Stationary intraoral tomosynthesis

T: Total

TACT: Tuned aperture computed tomography

UMN: University of Minnesota

UNC: University of North Carolina

XCP: Extension cone paralleling

LIST OF PUBLICATIONS

Refereed articles:

1. E. Gunnell, D. Franceschi, **C. Inscoe**, A. Hartman, J. Goralski, A. Ceppe, B. Handly, C. Sams, L. Fordham, J. Lu, O. Zhou, Y. Lee, "Initial clinical evaluation of stationary digital chest tomosynthesis in adult patients with cystic fibrosis", European Radiology (submitted), March 2018

2. **C. Inscoe,** E. Platin, S. Mauriello, A. Broome, A. Mol, L. Gaalaas, M.W. Regan Anderson, C. Puett, J. Lu, and O. Zhou, "Characterization of a stationary intraoral tomosynthesis system", Medical Physics 17-1624 (under review), January 2018

3. C. Puett, **C. Inscoe,** Y. Lee, O. Zhou, and J. Lu, "A phantom-based study exploring the effects of different scatter correction approaches on the reconstructed images generated by contrast-enhanced stationary digital breast tomosynthesis", Journal of Medical Imaging 17296, January 2018

4. C. Puett, **C. Inscoe,** A. Hartman, J. Calliste, D. Franceschi, J. Lu, O. Zhou, and Y. Lee, "An update on carbon nanotube-enabled X-ray sources for biomedical imaging", Wiley Interdisciplinary Reviews: Nanomedicine and Nanobiotechnology 10(1), 2018

5. S. Bazyar, **C. Inscoe,** E. O'Brien, O. Zhou, and Y. Lee "Minibeam radiotherapy with small animal irradiators; in vitro and in vivo feasibility studies", Physics in Medicine and Biology 62(23), 2017

6. S. Bazyar, **C. Inscoe,** T. Benefield, L. Zhang, J. Lu, O. Zhou, and Y. Lee, "Neurocognitive sparing of desktop microbeam irradiation", Radiation Oncology 12:127, 2017; doi:10.1186/s13014-017-0864-2

7. G. Wu, **C. Inscoe,** J. Calliste, J. Shan, Y. Lee, O. Zhou, and J. Lu, "Estimating scatter from sparsely measured primary signal", Journal of Medical Imaging 4(1), 2017

8. H. Yuan, L. Zhang, J. Frank ,**C. Inscoe,** L. Burk, M. Hadsell, Y. Lee, J. Lu, S. Chang, and O. Zhou, "Treating brain tumor with microbeam radiation generated by a compace carbon-nanotube-based irradiator: initial radiation efficacy study", Radiation Research 184 (3): 322-333, 2015; doi: 10.1667/RR13919.1

9. L. Zhang, H. Yuan, **C. Inscoe,** P. Chtcheprov, M. Hadsell, Y. Lee, J. Lu, S. Chang, and O. Zhou, "Nanotube x-ray for cancer therapy: a compact microbeam radiation therapy system for brain tumor treatment", Expert Review of Anticancer Therapy, vol. 14, no. 12, pp. 1411–1418, 2014

10. P. Chtcheprov, L. Burk, H. Yuan, **C. Inscoe,** R. Ger, M. Hadsell, J. Lu, L. Zhang, S. Chang, and O. Zhou, "Physiologically gated microbeam radiation using a field emission x-ray source array", Medical Physics 41(8): 081705, 2014; doi: 10.1118/1.4886015

11. E. Gidcumb, B. Gao, J. Shan, **C. Inscoe,** J. Lu, and O. Zhou, "Carbon nanotube electron field emitters for x-ray imaging of human breast cancer", Nanotechnology 25(24), 2014

Conference proceedings:

12. S. Mauriello, E. Platin, A. Broome, **C. Inscoe**, A. Mol, J. Patel, "Use of stationary digital intraoral tomosynthesis (sIOT) for bitewing radiography", IADR 2018 (upcoming)

13. Y. Lee, E. Gunnell, **C. Inscoe**, C. Puett, J. Lu, O. Zhou, "Initial clinical evaluation of gated stationary digital chest tomosynthesis", SPIE Medical Imaging 1057317 2018

14. C. Puett, **C. Inscoe**, R. Hilton, A. Mol, E. Platin, J. Lu, O. Zhou, "Stationary digital intraoral tomosynthesis: demonstrating the clinical potential of the first-generation system", SPIE Medical Imaging 1057313, 2018

15. **C. Inscoe,** G. Wu, D. Souliouti, E. Platin, A. Mol, L. Gaalaas, M. Regan Anderson, A. Tucker, S. Boyce, J. Shan, B. Gonzales, J. Lu, and O. Zhou, "Stationary intraoral tomosynthesis for dental imaging", SPIE Medical Imaging 10132, 2017

16. C. Puett, J. Calliste, G. Wu, **C. Inscoe,** Y. Lee, O. Zhou, and J. Lu, "Contrast enhanced imaging with a stationary digital breast tomosynthesis system", SPIE Medical Imaging 1013225, 2017; doi: 10.1117/12.2254348

17. **C. Inscoe,** G. Wu, J. Shan, Y. Lee, O. Zhou, and J. Lu, "Low dose scatter correction for digital chest tomosynthesis", SPIE Medical Imaging 941248, 2015

18. G. Wu, **C. Inscoe**, J. Calliste, Y. Lee, O. Zhou, and J. Lu, "Adapted fan-beam volume reconstruction for stationary digital breast tomosynthesis", SPIE Medical Imaging 94123J, 2015

19. P. Chtcheprov, **C. Inscoe**, L. Burk, R. Ger, H. Yuan, J. Lu, S. Chang, and O. Zhou, "High resolution X-ray fluorescence imaging for a microbeam radiation treatment planning system", SPIE Medical Imaging 90334C, 2014; doi: 10.1117/12.2043604

20. S. Xu, **C. Inscoe,** J. Lu, O. Zhou, Y. Chen "Pre-computed backprojection based penalized-likelihood (PPL) reconstruction with an edge-preserved regularizer for stationary Digital Breast Tomosynthesis." SPIE Medical Imaging 903359, 2014

21. **C. Inscoe,** A. Tucker, O. Zhou, and J. Lu, "Demonstration of a scatter correction technique in digital breast tomosynthesis", SPIE Medical Imaging 86680H, doi: 10.1117/12.2008044 2013

22. A. Tucker, C. Kuzmiak, **C. Inscoe,** Y. Lee, J. Lu, and O. Zhou, "Feasibility of stationary digital breast tomosynthesis as an effective tool for patients with augmentation mammoplasty", Proc. SPIE 8668, 86685Q (2013)

Patent

23. J. Lu, J. Shan, Y. Lee, O. Zhou, J. Calliste, **C. Inscoe,** P. Chtcheprov, and A. Tucker, "Systems and related methods for stationary digital chest tomosynthesis (s-dct) imaging", US14886842 Pending

CHAPTER 1: X-RAY GENERATION AND IMAGING

1.1 X-ray Generation

1.1.1 Discovery

In 1895, Wilhelm Roentgen inadvertently discovered the x-ray during experimentation with a Crooke's tube. [1] A Crooke's tube is an early variety of residual gas discharge tube, with which an electron beam can be generated. Roentgen observed that a scintillator screen in the vicinity of the tube had been exposed without the use of visible light and that this new ray could penetrate dense objects. [2] Though the mechanism behind the x-ray was not fully understood at the time, the clinical implications of his discovery were immediately obvious, with research and implementation spreading rapidly and ultimately revolutionizing medicine and dentistry. [3] [4]

1.1.2 X-ray source architecture

In 1913, William Coolidge invented the x-ray tube and the fundamental design has remained largely unchanged over the past 100 years. The Coolidge tube was comprised of two electrodes mounted in a glass vacuum tube. Rather than relying on the somewhat unstable electron production from gas discharge, the Coolidge tube contained a thin tungsten wire cathode. [2] Tungsten was chosen for the filament for its high melting point and resistivity. The high melting point and large atomic number, Z, also make it a good choice for the anode material, as the intensity of the beam is proportional to Z. [4] Electrons generated at the cathode are accelerated through a large potential and bombard the anode. The electrons decelerate rapidly when they reach the anode, releasing energy as x-ray photons, referred to as Bremsstrahlung and characteristic x-ray radiation. Because much of the energy is realized in the form of heat on the anode, thermal loading of the material is always a consideration. Modern x-ray tubes often

incorporate rotation or a cooling mechanism in the anode assembly to allow for greater tube current. [2] Additional electrodes are also incorporated to focus the electron beam into a small focal spot on the anode resulting in better image resolution. Though a point source x-ray beam would provide the greatest spatial resolution, thermal constraints of the anode preclude the use of highly focused beams. To reduce the heat loading, yet provide a reasonable focal spot, the anode is placed at an angle with respect to the electron beam. The effective focal spot, as viewed from the tube exit window, is much smaller than the actual area of bombardment on the anode. [4] A photo of a modern analytical x-ray tube (Nonius, Inc.) is shown in figure 1-1. The physical characteristics are very similar to Coolidge's original design.

Figure 1-1: Photo of an analytical x-ray tube (Nonius, Inc.)

1.1.3 Thermionic x-ray generation

Traditional x-ray sources generate their electron supply via thermionic emission, similar to an incandescent light bulb. A thoriated tungsten filament is installed within the cathode assembly. When current is passed through the filament, resistance and temperature increase rapidly, generating free

electrons. The presence of thorium on the filament surface exponentially increases the number of electrons produced at much lower temperatures than those required for pure tungsten. [5] This cloud of electrons is available for acceleration toward an anode for x-ray production. The number of free electrons increases with temperature, and therefore filament current directly drives the total tube current.

Thermionic emitters have been a fundamental component of nearly all x-ray devices since their inception. They are reliable, have a clinically acceptable life span, and can produce tube currents up to 1200mA. [1] Two notable drawbacks to the use of thermionic emitters include the generation of heat and the temporal resolution for cathode warm up, cool down, and system discharge. The implementation of grid switching has improved upon the temporal response to some degree. [2] Thermionic filaments are also somewhat limited in size and shape due to their emission mechanism. Manipulation of the electron beam via addition of magnetic focusing structures is required to achieve the smallest focal spots. [2]

1.1.4 Field emission x-ray generation

Though tungsten emitters are the most commonly used cathode in x-ray sources, other mechanisms exist for electron production. In a phenomenon known as field emission, some cathodes generate electrons without heat, when moderate voltage is applied. The behavior of these emitters is described by the Fowler-Nordheim equation, for which the material must have a very low work function or high field enhancement factor. [2] The use of Spindt-type field emitters [6] for x-ray generation has been explored, but material interactions, such as sputtering and degradation within the tube, have hindered their utilization in medical imaging. [2]

1.2 X-ray interactions in matter

There are numerous mechanisms by which photons can interact with matter, depending on the photon energy and number and type of particles encountered. The energy range for diagnostic x-ray imaging applications is ~15-140keV, so interactions are primarily due to the photoelectric effect and Compton scatter.

1.2.1 Photoelectric effect

The photoelectric effect occurs when a photon interacts with an atom to transfer a quantity of energy sufficient to knock an electron out of its orbit. The photon is completely absorbed by the atom and the electron propagates with energy equal to the incident photon energy minus the binding energy of its shell. The shell then contains a hole which is back filled by an electron from a higher orbit, releasing an additional photon, or characteristic x-ray. The characteristic x-rays can cause the release of additional electrons in outer shells, or Auger electrons. [1]

1.2.2 Compton scatter

The Compton Effect occurs when a photon trajectory is affected by interaction with outer shell, or valence, electrons. Only a portion of the incident energy is lost to the ejected Compton electron, and the Compton photon changes direction and continues propagation at lower energy. Depending on its energy, the Compton photon can initiate subsequent Compton or photoelectric interactions.

1.2.3 Attenuation

The macroscopic effect of these photon interactions is that an x-ray beam traversing any medium will lose some intensity, or be attenuated. The degree of attenuation due to absorption and scattering of photons is largely dependent on the density of the medium and the energy of the beam. Roentgen discovered that the amount a beam is attenuated in a homogenous substance is proportional to the distance traversed. This relationship is described in equation 1-1, where I is the intensity of the incident beam, x is the distance traversed, and μ is the linear attenuation coefficient. [4]

Equation 1-1: $-\frac{dI}{I} = \mu dx$

The integral form of equation 1-1 is shown below in equation1- 2, where I_0 is the incident x-ray intensity and I is the transmitted intensity.

Equation 1-2: $I = I_0 e^{-\mu x}$

As μ is a coefficient proportional to the density of the material, this relationship is also expressed using the mass absorption coefficient, μ/ρ, and density, ρ, as shown in equation 1-3. [4]

Equation 1-3: $I = I_0 e^{-(\frac{\mu}{\rho})\rho x}$

It is the differential attenuation of materials that makes x-ray imaging possible. The photoelectric effect contributes largely to the image contrast, with the probability of an event proportional to Z^4. Compton interactions tend to result in image degradation, which will be discussed in detail in chapter four.

The interaction of charged particles and high energy photons within the body, or radiation dose, is undesirable and increases the lifetime chance of developing cancer. It is therefore critical to minimize the dose to patients and radiological operators.

1.3 X-ray imaging

The benefit of x-ray images was apparent to Roentgen immediately after his discovery. Over one hundred years later, researchers still strive to improve upon the quality of x-ray images and create new medical, dental, and industrial applications.

1.3.1 X-ray detection

A robust, high resolution x-ray source is only as useful as the receptor used to measure it. Early x-ray images were obtained using scintillator screens. Using the same principle, intensifying screens and radiographic film are still in use today. [1] The development of electronic receptors, such as charged-coupled devices (CCDs) and complementary metal-oxide-semiconductor (CMOS) detectors, has enabled the creation of advanced x-ray devices and new applications that are difficult or impossible with traditional receptors.

The quality of a detector can be defined by several metrics. The ability to stop and count each incident photon is a basic property of detectors known as quantum efficiency. The ability to convey that information into a high quality image is known as detective quantum efficiency (DQE) and is defined by the input and output signal-to-noise ratio (SNR) (Equation 1-4).

Equation 1-4: $DQE = \left(\frac{SNR_{out}}{SNR_{in}}\right)^2$

Another fundamental property of a detector is the resolution, dictated by the size of the pixels and the mechanism for x-ray detection. Direct detectors count photons directly without an intermediate step. Indirect detectors incorporate a scintillator to convert the x-rays to visible light. This can result in some loss of resolution due to the quality and composition of the scintillator.

Some modern applications of x-ray require a detector that can provide a fast frame rate. The image should be acquired and read out to a pc at a rapid rate without leaving any afterglow, or ghosting, in the scintillator.

1.3.2 Planar radiography

The acquisition of two-dimensional (2D) x-ray images, called projection or planar radiography, is a staple of medical and dental practices. In planar radiography, the x-ray source is placed at a distance of ~20-180cm from the detector with the patient near, or touching the detector. The beam is collimated to the region of interest and a short pulse of x-ray radiation is generated, passing differentially through the patient, to the detector. The resulting image is a 2D representation of the 3D volume traversed by the beam. Depending on the source-to-detector distance (SDD), some anatomical features may be distorted by magnification. Other features of interest may be obscured by the superposition of bone or tissue in the beam path. Despite these limitations, x-ray is widely used not only for diagnostic, but also for screening applications.

1.3.3 Computed tomography

Computed tomography (CT) is a three-dimensional (3D) modality that eliminates the problem of anatomical superposition by acquiring 2D projection images from many different angles and utilizing a reconstruction algorithm to compute a 3D representation of anatomy, presented as a collection of slice images. CT is a valuable tool in medicine and dentistry, but requires a large radiation dose. It is therefore used only for applications in which 2D imaging has been deemed unusable.

1.3.4 Limited angle tomography and tomosynthesis

Limited angle tomography, or tomosynthesis, is a quasi-3D modality using reduced angular coverage, fewer projection images, and lower dose than CT. Projection images are acquired by moving an x-ray source in an arc or line about a fixed object and detector. If the precise geometrical relationship between source and detector is known, the images can be manipulated to provide depth information about the object. The radiologist can scroll through the slice information, eliminating superposition of out-of-plane features. Tomosynthesis imaging has flourished in the past ten years, with FDA-approved devices for breast and chest imaging showing promising results. [7] The relatively low radiation dose, cost, and ease-of-use make tomosynthesis an attractive alternative to fill the void between 2D and CT regarding both image quality and dose.

CHAPTER 2: CARBON NANOTUBE-BASED X-RAY SOURCES

2.1 Carbon nanotube cathodes

The discovery of the carbon nanotube (CNT) by Sumio Iijima in 1991 [8] sent researchers around the world into a frenzy to synthesize and find novel applications for this unusual new structure. CNTs are comprised of cylindrical graphene sheets, forming a tubular structure of nanoscale diameter. A single-wall nanotube (SWNT) is comprised of only one sheet of graphene, but CNTs more commonly consist of multiple sheets termed multi-wall nanotube (MWNT), ranging from two to approximately forty layers. [9] CNTs can be synthesized in several ways, such as chemical vapor deposition or laser ablation, and can reach 10um in length. The small diameter and relatively long length give CNTs a very high aspect ratio and atomically sharp tip. These properties yield a large field enhancement factor when voltage is applied, and are therefore excellent field emitters. [10]

Ten years ago, researchers in our group at UNC perfected a process to create robust CNT cathodes for field emission applications. [11] Using sophisticated photolithography and deposition techniques, substrates were fabricated and coated with CNTs via electrophoretic deposition. Many CNT suspension recipes were compared to optimize adhesion, deposition rate, and current density. After annealing and activation, the cathodes were qualified in an evacuated testing chamber with phosphor screen to visualize the emitter distribution. They also underwent rigorous current-voltage (I-V) cycling and lifetime tests to ensure stability and uniformity amongst a cohort. [10] The CNT cathode deposition technology developed in our lab has been licensed and commercialized by a UNC start-up company, Xintek, Inc.

One of the first applications of CNT field emission cathodes in our lab was microscopic image-guided microbeam cellular irradiation. This implementation used the cathode to generate an electron beam to target individual cancer cells within a petri dish. [12] Though effective for in-vitro studies, the short mean free path of electrons in air makes them an impractical choice for in-vivo studies. A more useful approach is to use the CNT cathodes for x-ray production.

2.2 Carbon nanotube x-ray sources

Over the past twelve years, our research group has incorporated the CNT cathode into many different x-ray devices. Early systems used a single cathode in a vacuum chamber (Figure 2-1a) utilizing a rotation stage for the object to perform pre-clinical micro-computed tomography (μ-CT) imaging. [13] The next steps were development of a high resolution μ-CT device for small animal imaging [14] with prospective physiological gating capability. [15] This system incorporated a more portable x-ray source, in a small stainless steel chamber (Figure 2-1b), mounted on a rotating gantry. Figure 2-1c is the complete system, shown with integrated radiation shielding, designed and constructed by our team at UNC. Figure 2-2a is a photo of a commercial CNT x-ray source being marketed in an FDA-approved imaging device from CareStream called the DRX-Revolution Nano mobile x-ray system (Figure 2-2b).

.

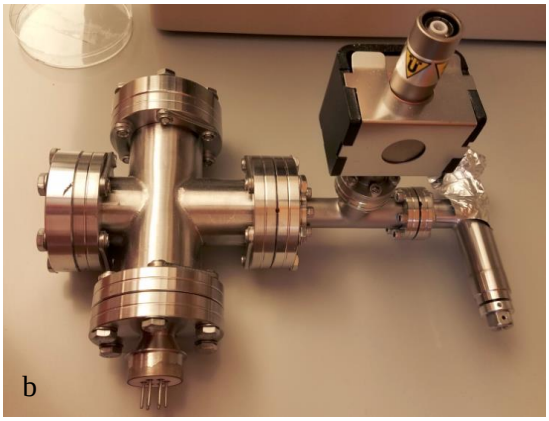

Figure 2-1: a) An early CNT x-ray source constructed in a large vacuum chamber; b) A CNT-based micro-focus x-ray tube incorporated into (c) a micro-CT system with integrated shielding for small animal imaging designed and constructed at UNC.

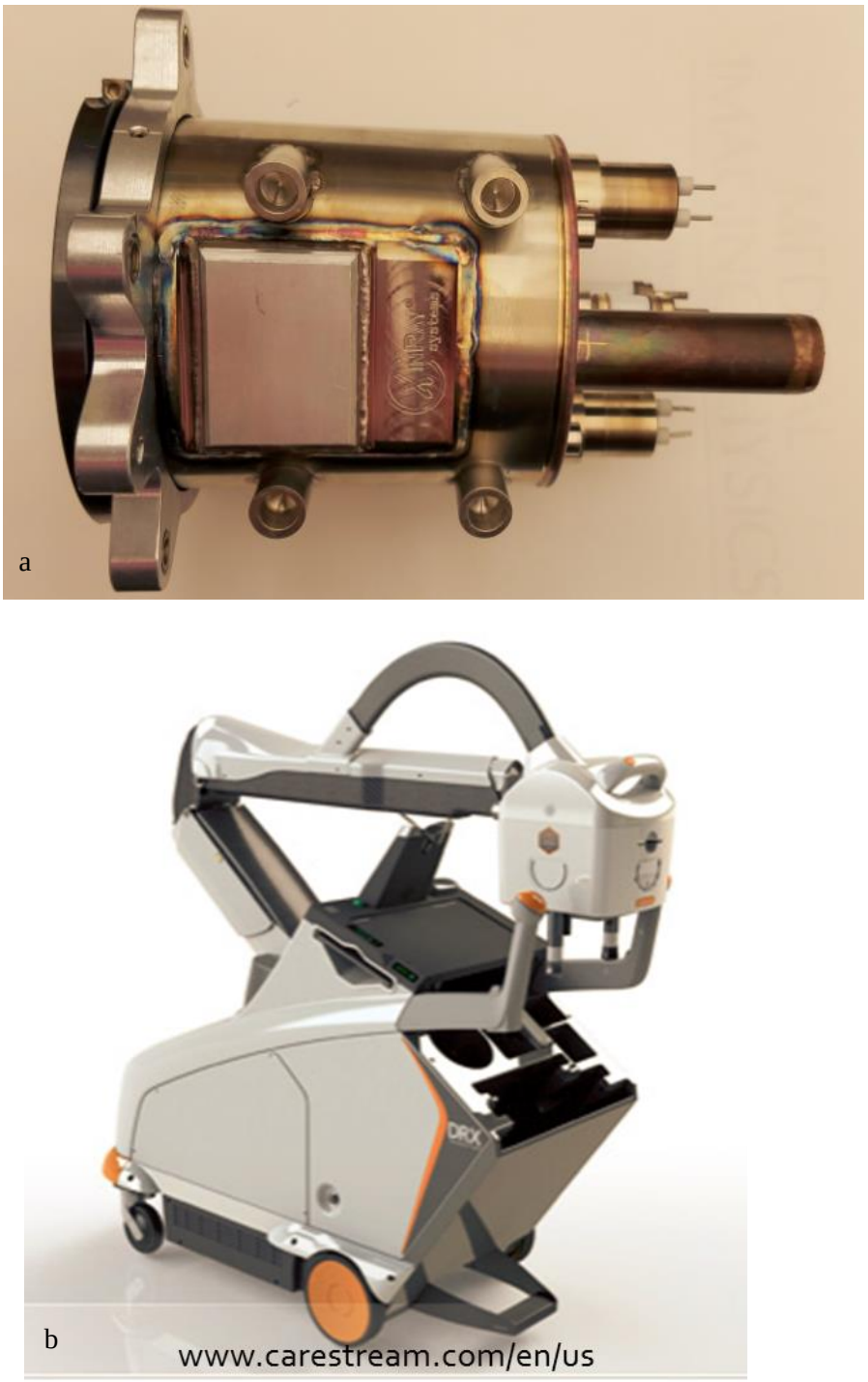

Figure 2-2: A commercially-available x-ray tube (a) and system (b) based on CNT source technology developed in our lab at UNC.

2.3 Carbon nanotube x-ray source arrays

The success of the early CNT x-ray sources prompted concurrent evolution into other x-ray devices. Because the emission mechanism does not generate heat on the cathode, multiple devices can be constructed in close proximity, allowing for construction of spatially-distributed, multi-beam field emission x-ray source arrays [16]. Several multi-beam field emission x-ray source arrays were constructed in our lab for radiation therapy [17] [18] and imaging [19]. Two of the first CNT x-ray source arrays developed in our lab are shown in figure 2-3. The source array technology and designs have been licensed and commercialized by Xinray Systems. A recently fabricated x-ray source array is shown in Figure 2-3b.

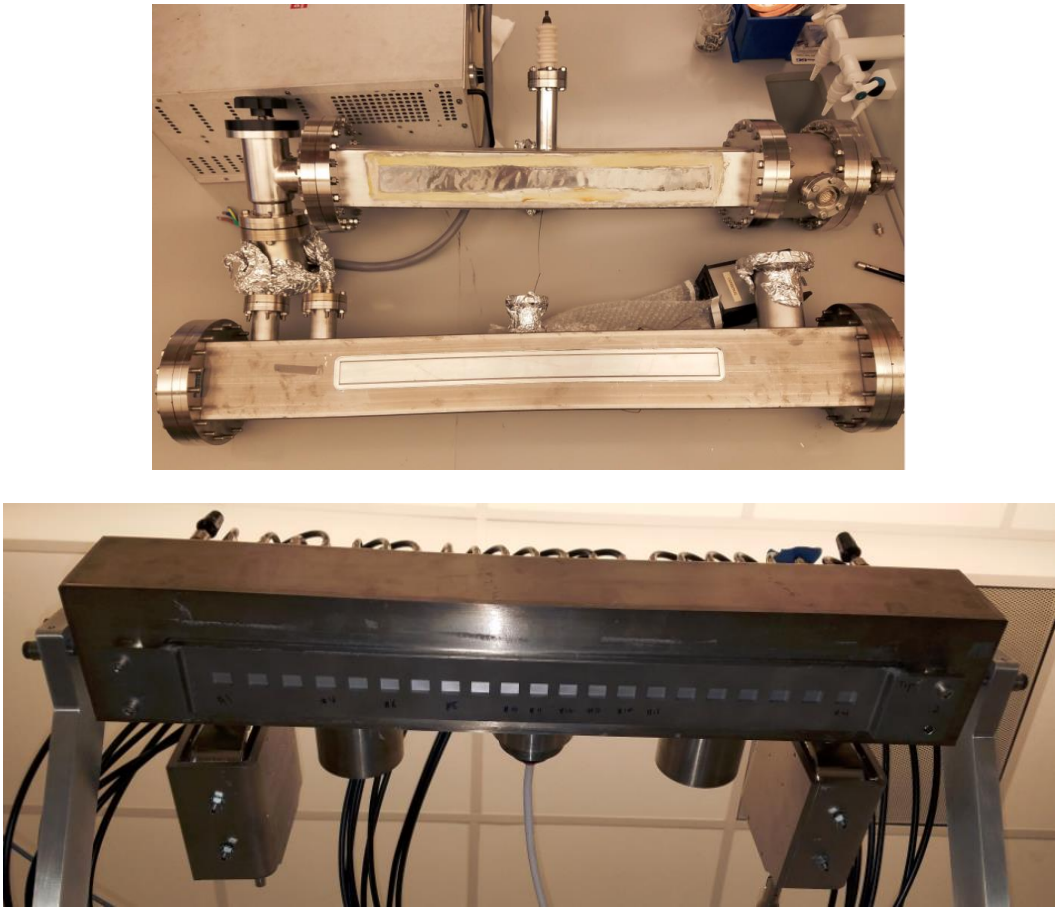

Figure 2-3: a) Photo of two of the first CNT linear x-ray source arrays fabricated in our lab at UNC; b) Photo of a recently fabricated CNT x-ray source array from Xinray Systems.

2.4 Stationary tomosynthesis systems

For nearly a century, researchers have been exploring the manipulation of 2D images to gain depth information and combat the problem of structure superposition. CT is the only true 3D modality and its accurate presentation of anatomical relationships has made it an indispensable component of radiology. A series of planar radiographs are acquired in a circular or helical configuration and processed by an algorithm to calculate a 3D volumetric representation without magnification, distortion, or superposition. This added utility comes at the cost of additional patient radiation dose, in some cases 100x that of planar radiography. Expensive system hardware, physical size, and computational overhead are additional drawbacks to CT. Use is therefore limited to diagnostic applications for which 2D imaging has been deemed inadequate.

As the utilization of x-ray imaging in medicine and dentistry has expanded, awareness of the harmful effects of radiation has increased. Radiation safety regulatory agencies demand that imaging is performed with a dose that is as low as reasonably achievable (ALARA). The fundamental mechanism of x-ray attenuation means there is a minimum exposure required in an image to ensure adequate photon statistics. Reduction of exposure and dose in 2D radiography is primarily dependent on the detector efficiency and to some degree the beam quality and scatter reduction. In CT, additional factors such as the angular coverage and number of projections affect the total resulting dose. Limited angle tomography has been proposed as serioscopy [20], laminography [21] [22], dynamic tomography [23], and most commonly, tomosynthesis [24]. These techniques were shown to provide some depth resolution using multiple 2D images. Clinical implementation of tomosynthesis was previously hindered by the requirement of precise source/receptor relationships and receptor and computer technology. Successful application required serial exposure of radiographic films, placed in a known geometry, with no patient motion, limiting clinical practicality. Recent advancements in source, detector, and computer technology have helped to reduce the dose in both 2D and CT imaging and are now spawning a renewed interest in tomosynthetic applications.

Tomosynthesis is currently experiencing rapid growth in clinical implementation due to the appeal of gleaning 3D information with a relatively low radiation patient dose. Though the potential applications of tomosynthesis are essentially limitless, the slightly elevated radiation dose and layer of complexity are not always warranted. There are many clinical tasks for which a standard 2D radiograph is well suited and considered to be the gold standard. The successful translation of tomosynthetic imaging requires finding a true clinical need for improvement in screening and/or diagnostic capability.

Until recently, accomplishing tomosynthesis required physical motion of a conventional x-ray tube, often through a line or an arc, to acquire projection images from different viewing angles. Using source array architecture, an object can be imaged from multiple angulations quickly and without any mechanical motion, eliminating motion blur due to the moving focal spot. System scan time is not limited by source motion, but primarily by detector frame rate. A fast detector can therefore reduce total scan time and resulting patient discomfort and motion. Elimination of source and patient motion result in higher resolution tomosynthesis slice images than conventional tomosynthesis systems [25]. Task-specific CNT-enabled stationary tomosynthesis devices have been developed for breast [26] and chest [27] imaging and are now enrolling patients in human studies.

2.4.1 Stationary digital breast tomosynthesis (s-DBT)

The stationary digital breast tomosynthesis system (s-DBT) was created by retrofitting a distributed x-ray source array (Xinray Systems, Morrisville, NC) onto a Selenia Dimensions gantry (Hologic, Inc., Bedford, MA) (figure 2-4a) [26] [28] [29] [25] [30]. This was motivated by the desire to produce a system with higher resolution and a faster scan time than commercially available systems by eliminating X-ray source motion and focal spot blur. A duplicate of this system is installed in the Mammography Department at the UNC Hospitals and is being utilized for Institutional Review Board (IRB) approved clinical trials Figure 2-4b is a computer-aided design (CAD) drawing of the breast

imaging system, with representative x-ray beams shown emanating from the source array and impinging on the breast compression paddle and detector.

.

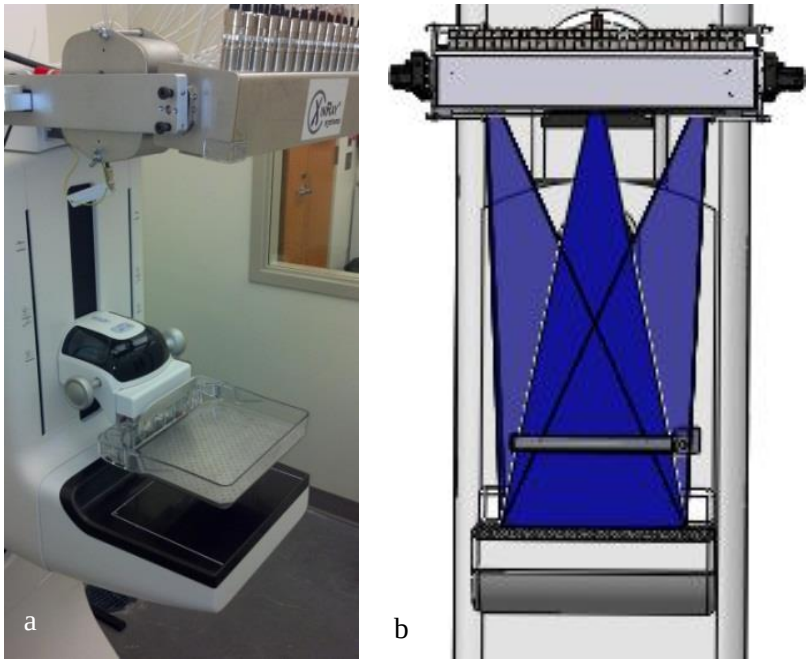

Figure 2-4: a) Photo of s-DBT system; b) CAD drawing illustrating three representative x-ray beams emanating from the source array.

2.4.2 Stationary digital chest tomosynthesis (s-DCT)

Digital chest tomosynthesis (DCT) is a modality providing some of the depth information found in CT with a ten-fold reduction in dose. DCT systems acquire images at multiple angles for quasi-3D reconstruction. Studies have shown that DCT is capable of visualizing 5mm+ lung nodules as effectively as CT and has potential to become a screening tool for lung cancer. [31] DCT systems currently in use employ a single, moving source to acquire multiple images. Our group has recently demonstrated the feasibility of stationary DCT (s-DCT) utilizing a stationary x-ray source array. [32] [33] [27] Compared to the regular DCT technology, s-DCT can potentially improve image quality by minimizing image blur caused by source and patient motion with faster data acquisition and respiratory gating. Figure 2-5 is a

photo of the s-DCT system installed in the Biomedical Research Imaging Center (BRIC) in Marsico Hall at UNC.

Figure 2-5: s-DCT system installed in BRIC, Marsico Hall, UNC

2.4.3 Stationary digital orthopedic tomosynthesis (s-DOT)

The most recent pre-clinical application of our CNT x-ray source technology is stationary digital orthopedic tomosynthesis (s-DOT) for joint imaging. Figure 2-6a shows the benchtop prototype system. Phantom and animal specimen studies (figures 2-6b and c) have been performed with promising results.

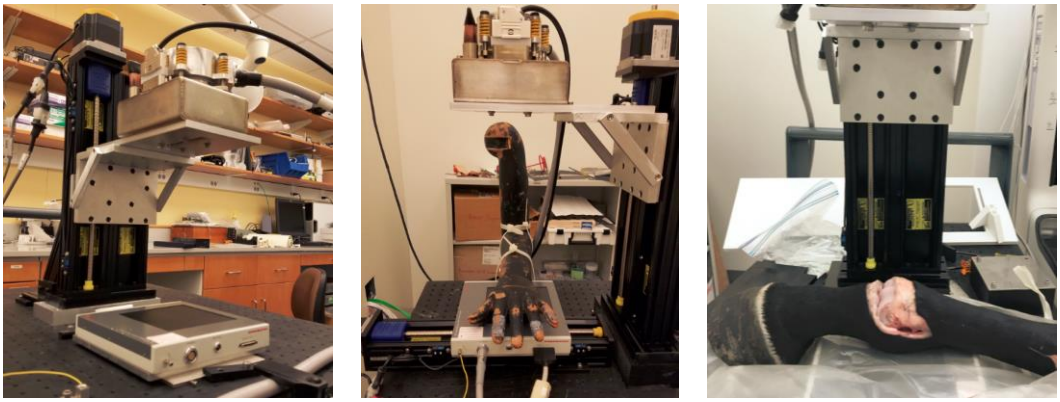

Figure 2-6: a) Prototype stationary digital orthopedic tomosynthesis (s-DOT) system; b) s-DOT with arm phantom positioned for detector translation; c) s-DOT with equine limb positioned for AP fetlock imaging.

CHAPTER 3: STATIONARY INTRAORAL TOMOSYNTHESIS

3.1 Dental radiography

3.1.1 Two-dimensional intraoral radiography

Exploration into the clinical utility of dental radiography began shortly after the discovery of the x-ray, with dental imaging devices evolving at a pace similar to medical radiography [3]. Two-dimensional (2D) intraoral radiography is currently the most commonly used imaging tool in dental clinics, often considered to be an indispensible component of dental screening and diagnosis, and the gold standard for caries detection. Improved efficiency of intraoral receptors, including film, photostimulable phosphor plates, and digital detectors, has greatly reduced the amount of radiation required to obtain images of diagnostic quality. Unfortunately, the features of interest within the dental anatomy are often obscured by superposition of bone, teeth, restorations, and dental hardware. This superposition is a fundamental limitation due to the 2D nature of projection radiography and results in low diagnostic accuracy for many tasks [37]. Sensitivity of caries detection ranges from 40 to 70%, depending on the accessibility of the lesion [38], [39]. Root fracture detection is another application of 2D intraoral radiography that is lacking sensitivity, with features often obscured by adjacent anatomy [3], [40], [41].

3.1.2 Cone beam computed tomography

Cone-beam CT (CBCT) has been incorporated into many dental clinics for treatment planning, including endodontic treatment, implant site assessment, and evaluation of temporomandibular joint disorders. [3] Though valuable for diagnostic applications, CBCT is not appropriate as a screening tool.

The increased radiation dose to the patient, clinician time, and equipment cost outweigh the marginal increase in sensitivity for caries detection [42].

3.1.3 Tuned aperture computed tomography (TACT) and tomosynthesis

In the late 1990s, Webber et al. explored a limited-angle intraoral tomography technique referred to as Tuned Aperture Computed Tomography (TACT) [43] [44] [45]. TACT utilizes an intraoral detector and a standard 2D x-ray source to acquire projection images of a single region of interest at various angularities. Use of a fiducial marker [43], [46] on the buccal surface of the tooth allows calculation of source/detector geometry. A reconstruction algorithm generates slice images containing some depth information. TACT demonstrated improved sensitivity in the detection of root fractures and periodontal bone loss over conventional 2D intraoral imaging and was found to be useful during evaluation of implant sites and third molar impaction [47] [48] [49] [50] [51] [52] [53] [54] [55]. Investigations of TACT for caries detection produced varying results [52] [53] [54] [55] [56]. Although TACT clearly demonstrated the clinical benefits of tomosynthetic dental imaging and resulted in several patented technologies, it was never translated for clinical use, due to its technical limitations including the long imaging time and the use of the fiducial marker. Tomosynthesis has also been explored by use of a rotating-gantry, or C-arm, for x-ray source translation to precisely define the geometrical relationship with a fixed intraoral [57] or extraoral detector [58], [59]. Systems have also been proposed that utilize mounting fixtures for source translation around a pre-defined path with a fixed focal point [60]. Hindered by source and receptor capabilities and computational power of the era, TACT and tomosynthesis were great ideas ahead of their time. Twenty years of evolution in source, receptor, and computer technology revives an imperative to investigate dental applications of tomosynthesis.

3.1.4 Stationary intraoral tomosynthesis

Recognizing the potential implications of source array technology in dental imaging, stationary intraoral tomosynthesis (s-IOT) was proposed through a collaboration between our research team and dentists in the UNC School of Dentistry (SOD) [61]. The idea was assessed using an existing benchtop system using a CNT-source array (XinRay Systems, Morrisville, NC), dental phantoms and extracted teeth, and a standard intraoral detector (SuniRay2, Suni Medical Imaging, Inc.) [35]. Various angular spans and dose distributions were explored to define the optimal imaging configuration. Using this benchtop device, a preliminary reader study compared the detection sensitivity of s-IOT and standard 2D intraoral radiography for interproximal caries in extracted human teeth, using μ-CT images as the ground truth. Eight experienced dentist readers were 36% more likely to identify a carious lesion when viewing images generated by s-IOT compared to standard 2D intraoral radiography [34]. Encouraged by this statistically-significant finding, a spin-off company was formed, XinVivo, Inc. (Morrisville, NC), to commercialize the technology. Using system parameters determined by our team at UNC, XinVivo has designed and constructed a clinical prototype for use in the dental clinic. The UNC IRB has approved the use of the device for a patient trial evaluating caries detection [62]. This work details the preliminary work leading to the development of the s-IOT device. It also provides a full system characterization of the completed system with demonstrations of the potential range of its clinical application prior to human studies.

3.2 Preliminary work

3.2.1 System description

The s-IOT benchtop system is comprised of a linear x-ray source array (XinRay Systems, Inc., Research Triangle Park, NC) and a digital intraoral detector (Suni Medical Imaging, Silicon Valley, CA). The source array contains 75 individually-switchable focal spots, with 4mm spacing between adjacent

spots. A subset of focal spots was used in this study with an average focal spot size of 2.5mm x 0.5mm. As this is larger than what is used in a typical intraoral imaging system, the SDD was increased from 30-40cm, typically used in dental imaging, to 84-88cm to achieve a comparable system resolution of 10.05 cycles/mm. [35] The intraoral detector is a size 2 sensor (35.2mm x 25.2mm) with 33um pixel size. The typical source configuration used 7 or 15 beams. Figure 3-1a is a photo of the hardware and figure 3-1b is a diagram of the device configuration, showing representative X-ray beams emitting from the source array and impinging upon the sample and detector.

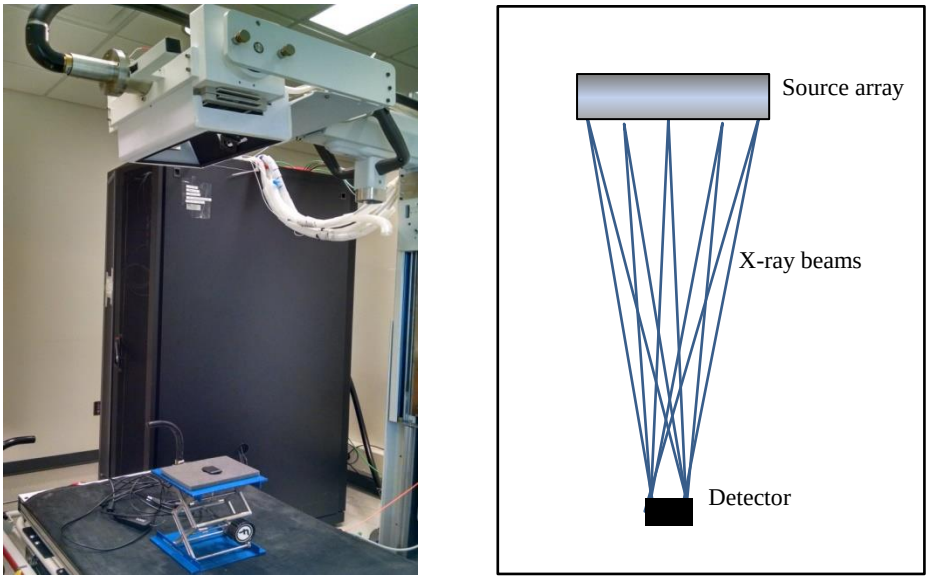

Figure 3-1: a) photo of s-IOT hardware for feasibility study; b) diagram of system configuration with representative x-ray beams.

3.2.2 Phantom and specimen imaging

A dental quality assurance phantom (RMI 501A, Radiation Measurements, Inc.), containing teeth embedded in maxillary bone, was imaged for initial evaluation (Figure 3-2a). The RMI phantom contains three segments of metal mesh, four thicknesses of bone mimic, and a human maxillary specimen with teeth containing metallic fillings and simulated caries lesions.

An IRB-approved *ex vivo* study was also carried out using 29 extracted human teeth containing natural caries. The specimens were covered with a 1cm thickness of dental wax to mimic soft tissue attenuation. Figure 3-2b is a sketch of the imaging configuration with the specimen lying on the intraoral detector and covered with the tissue-simulating wax slab. The s-IOT projection images were obtained at a tube voltage of 70kVp with 5mA of tube current per source. The exposure time was calculated to correspond to a total dose similar to that used for digital radiography using a D-speed film. Source-detector geometry was calculated from images of a phantom containing multiple stainless steel spheres. Standard 2D radiographs were acquired using a state-of-art clinical intraoral x-ray device at the UNC Dental Clinic with both digital detector and photostimulable phosphor plate (PSP) for comparison to tomosynthesis slices. Micro-CT scans of each sample were also acquired and used as a ground truth reference. Eight experienced dental radiologists were recruited as observers.

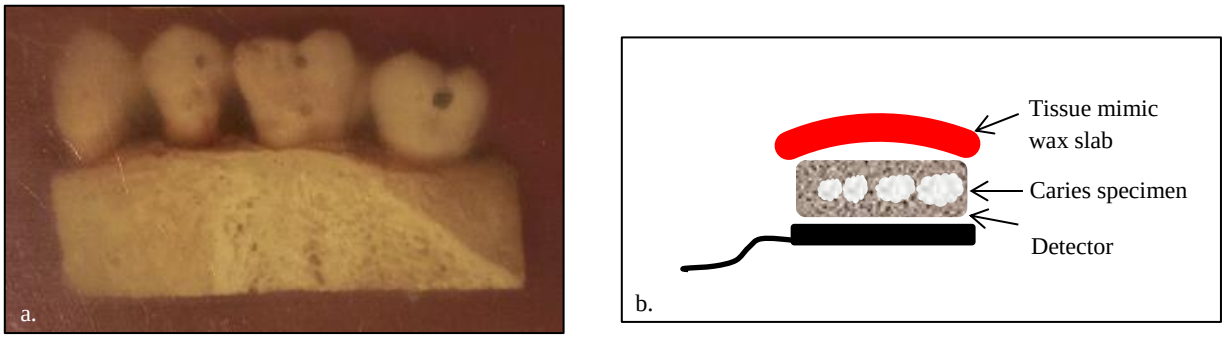

Figure 3-2:a) RMI dental quality assurance phantom; b) diagram of imaging configuration for specimen samples

3.2.3 Image reconstruction

Reconstruction refers to the processing steps by which the 2D information available from the projection views is used to mathematically construct a 3D image space displayed for viewing. Images were reconstructed using a simultaneous algebraic reconstruction technique (SART) iterative algorithm with total variance regularization. The reconstruction method is based on a modification of the adaptive-steepest descent projection onto convex sets (ASD-POCS) method. [63] [64] Reconstruction slices represent a thickness of 0.5mm, with a total of sixty slices, or 3cm of reconstructed volume.

Reconstruction was performed on a standard four-core personal computer (PC) with low-end graphical processing unit (GPU), requiring only 30 seconds per dataset.

3.2.4 System optimization

Specimens were imaged at multiple exposure levels corresponding to clinically acceptable levels for 2D intraoral imaging. Various beam configurations and dose distributions were also explored in order to determine the optimal parameters for construction of the clinical prototype. Dental radiologists reviewed the reconstruction slice images to validate image quality. Quality was assessed by visual examination of the dentino-enamel junction and ability to isolate interproximal surfaces and cusps in the occlusal plane.

3.2.5 Results

3.2.5.1 Phantom imaging

Reconstructed slices of both the phantom and the specimens contain a level of detail that is not present in 2D images. Caries lesions were visualized as well as root fractures. Overlapping root structure is clearly separated and allows easy visualization of palatal (third root) features. An example of this is shown in Figure 3, which are images of a maxillary first molar in the RMI phantom containing caries, fractures and a metallic filling. Figure 3-3a) is the 2D intraoral image. Figures 3-3b) and c) are tomosynthesis reconstruction slices of the same tooth at different depths. The caries lesion and filling exhibit high contrast in tomosynthesis slice images in comparison to the 2D image. Two fracture features can be identified in a reconstructed slice image (Figure 3-3c), but are obscured in the 2D intraoral image. The palatal root, which is difficult to visualize in the 2D image, is also very clear in the reconstructed image. Fine structures within the alveolar bone are also visualized better in tomosynthesis slice images. Figure 3-4 is a sketch of the maxillary first molar, indicating the orientation of image acquisition (left)

and a rotated distal view indicating the locations of the two reconstruction slices (right). Plane 1, through the buccal roots, is shown in figure 3-3b and plane 2, through the palatal root, is shown in figure 3-3c. Figure 3-3d depicts an ROI through asimulated caries lesion. This region was evaluated in both the 2D image as well as the reconstruction slice in the plane of focus. A plot profile of this region (figure 3-3e) reveals that the s-IOT slice provides better feature contrast and higher SNR.

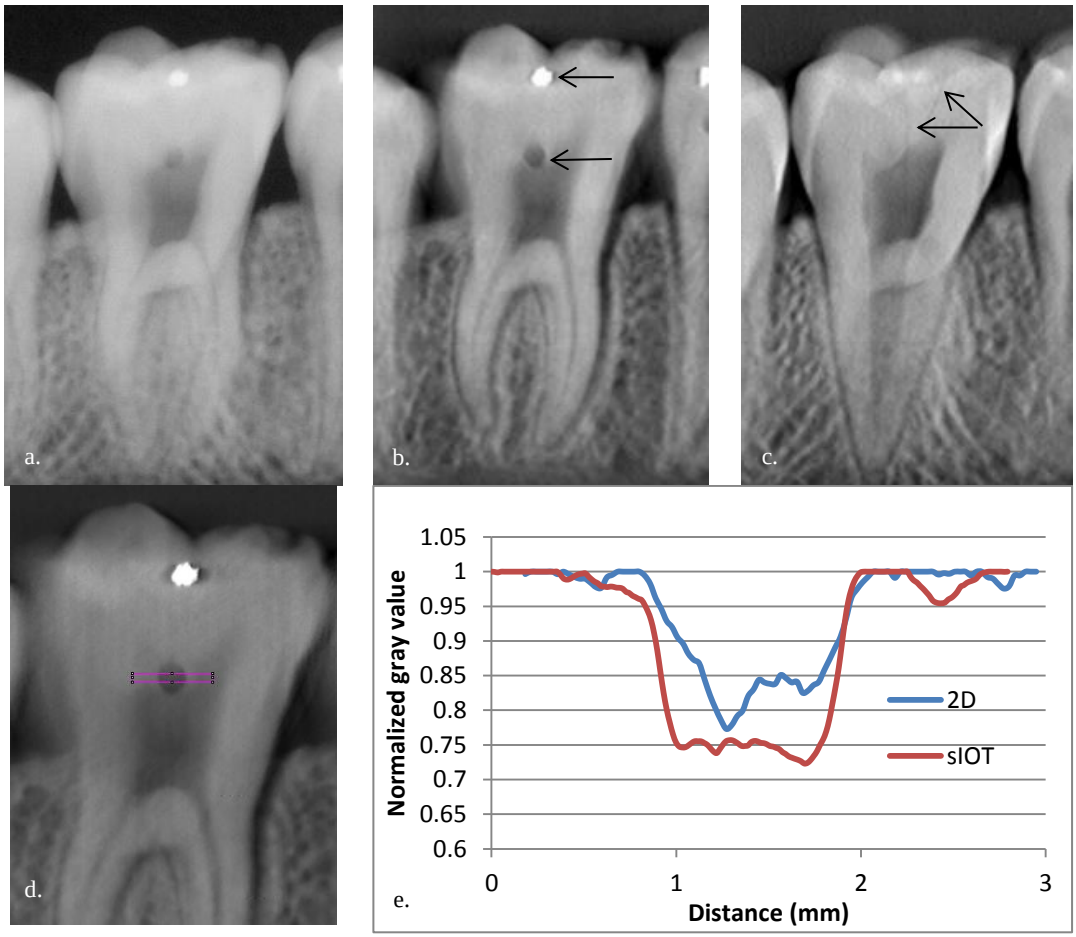

Figure 3-3: a) 2D image of a tooth in the RMI phantom containing a metallic filling, caries and fractures; b) Reconstructed tomosynthesis slice in the plane of the filling and the caries lesion; c) Reconstructed tomosynthesis slice in the plane of the fractures. Note the increased detail in the lesions (arrows) and alveolar bone in b) and c). The palatal root is visible in c), but is obscured in the 2D image. Figure 3-3d depicts an ROI through a caries lesion, with plot profiles of the 2D and s-IOT images shown in 3-3e.

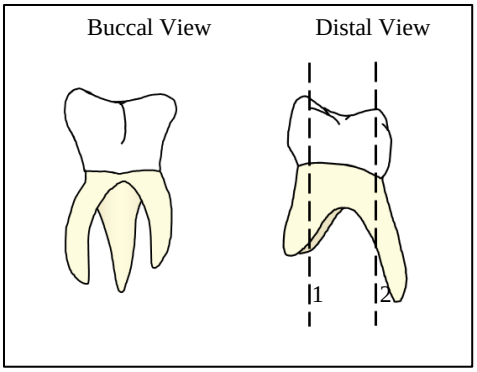

Figure 3-4: Anatomical sketch of a maxillary first molar. Images were acquired in the buccal-lingual direction (left). Location of reconstruction planes through the buccal roots (1) and palatal root (2) are indicated in the distal view of the molar (right).

3.2.5.2 Specimen imaging

The specimens containing real caries lesions were compared to their 2D counterparts in a reader study at the UNC School of Dentistry. The preliminary results of the observer study show a remarkable increase in sensitivity as compared to 2D intraoral x-ray without a sacrifice in specificity for detection of interproximal caries. Sample images are shown in figure 3-5. [34] The 2D intraoral images, taken with digital detector and PSP images are shown in comparison to the tomosynthesis reconstruction slice. Arrows indicate visible caries lesions, with more revealed in the tomosynthesis slice. Axial slices from micro-CT images give the ground truth lesion status.

3.2.5.3 System optimization

Specimen scans were performed with multiple imaging configurations, total dose, and dose distributions. Dental radiologists reviewed the results and a collective determination of final design parameters was made based on image quality and system complexity. Image quality was evaluated by examination of the dentino-enamel junction and capability to isolate occlusal and interproximal surfaces of interest. Using a standard clinical source-to-detector distance of 40cm, it was determined that seven sources spanning an angular range of 12 degrees produced adequate signal-to-noise ratio at a dose

equivalent to one D-speed film exposure. This source geometry would allow production of an x-ray source similar in form to a standard clinical 2D intraoral device.

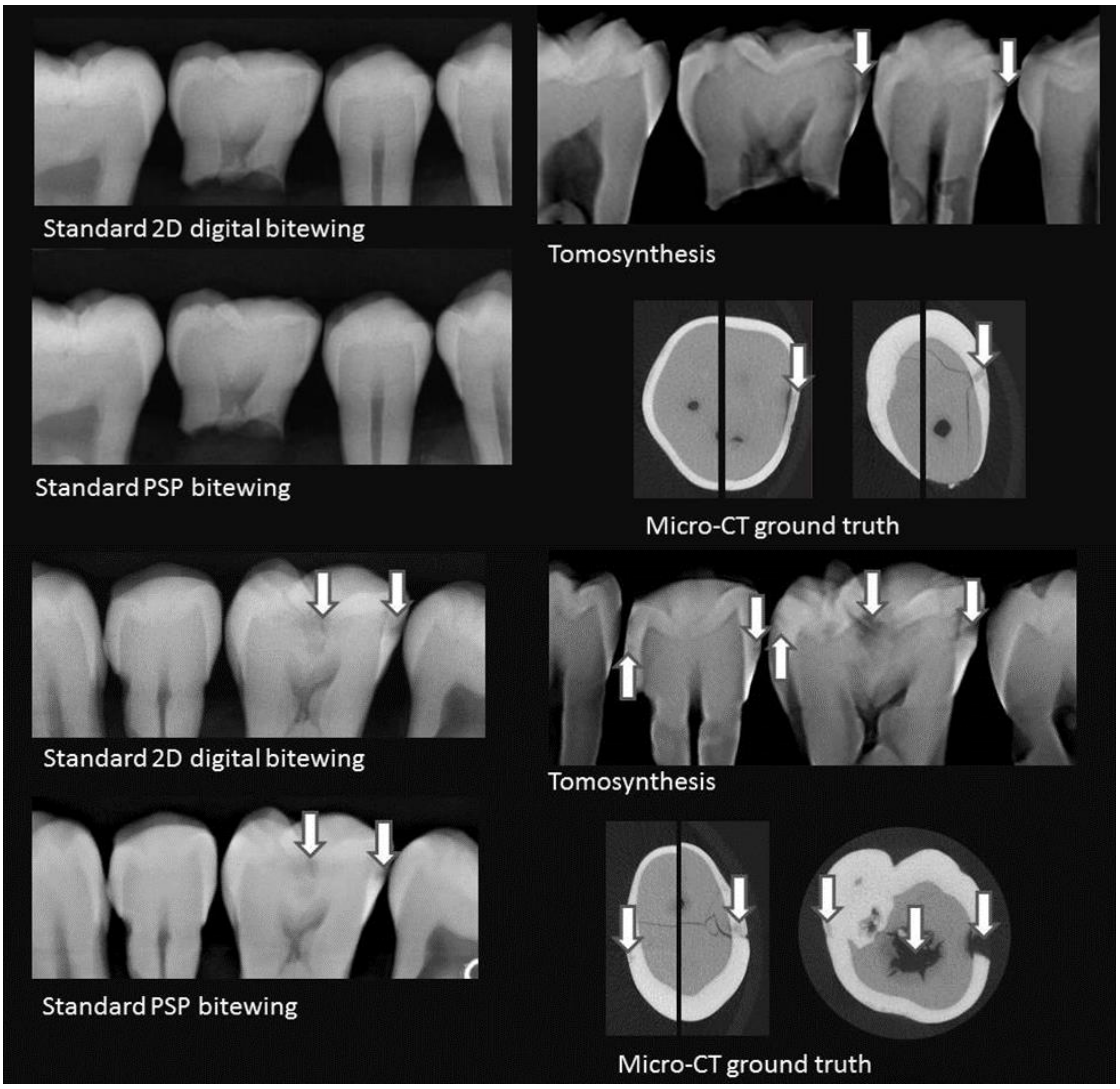

Figure 3-5: Comparison of other 2D intraoral bitewing images with s-IOT using extracted teeth. 2D intraoral images were acquired using a direct digital sensor and photostimulable phosphor (PSP). Micro-CT axial images display ground truth lesion status. Arrows on the 2D and s-IOT images indicate visible caries lesions. Arrows on the micro-CT images indicate confirmed lesions. [34] (Figure source: Mol, et al. [34])

3.2.6 Conclusions

In this study we demonstrated the feasibility of intraoral tomosynthesis using a CNT x-ray source array and an intraoral detector. The system produces a series of projection images of the teeth from a limited range of viewing angles by electronically activating the individual CNT x-ray beams without mechanically moving the source, the detector, or the specimen. The reconstructed images show improved visualization of the anatomy compared to 2D intraoral x-ray. The technology also showed a significant

increase in the sensitivity for detection of inter-proximal caries as compared to 2D intraoral x-ray, the current gold standard for caries detection, without sacrificing the specificity or increasing in the radiation dose. The image acquisition time of the present bench-top system is limited by the frame-rate of the current commercial intraoral sensor. With the next generation detector technology and development of dedicated CNT x-ray source array for intraoral imaging, the total tomosynthesis imaging time is expected to be reduced to the level sufficient for patient imaging.

System geometry was optimized using existing equipment in our research lab at UNC to dictate final design parameters for the clinical prototype fabricated at XinVivo. Specimen images were acquired using various imaging geometries and exposure levels. The reconstruction slice images were reviewed by our colleagues in the UNC SOD for sharpness of the DEJ and individualization of the proximal surfaces and tooth cusps. Final design parameters were based on the conclusions that seven sources spanning a twelve degree range would provide adequate image quality at exposure similar to 2D intraoral. This would achieve the desired form factor of a 2D source and a similar clinical workflow for patient screening.

3.3 s-IOT clinical prototype

3.3.1 System description

The first generation s-IOT clinical prototype system (XinVivo, Inc.) was designed to mimic a typical 2D intraoral x-ray device currently used in dental clinics (Figure 3-6a) using parameters determined by our team at UNC. After fabrication, the s-IOT system was installed in our research lab for my initial characterization and evaluation. The system was subsequently installed in the Department of Oral and Maxillofacial Radiology in the UNC School of Dentistry where I completed the characterization and system evaluation. Pre-clinical studies were performed in collaboration with various dentists and the system hardware and software were iteratively refined in conjunction with XinVivo engineers prior to patient imaging.

The CNT x-ray source array with an x-ray collimator is mounted on an articulating arm attached to the wall. A customized bitewing holder magnetically couples a standard digital intraoral detector to the exit window of the collimator and maintains a fixed source-to-image distance (SID) of 400mm, which creates an optimum geometry for the source array and satisfies the required separation between the x-ray source and patient. The operator specifies the imaging parameters using a graphical interface (Figure 3-6b) and a customized electronic switching system adjusts the x-ray output and synchronizes each exposure with the integration window of the digital detector.

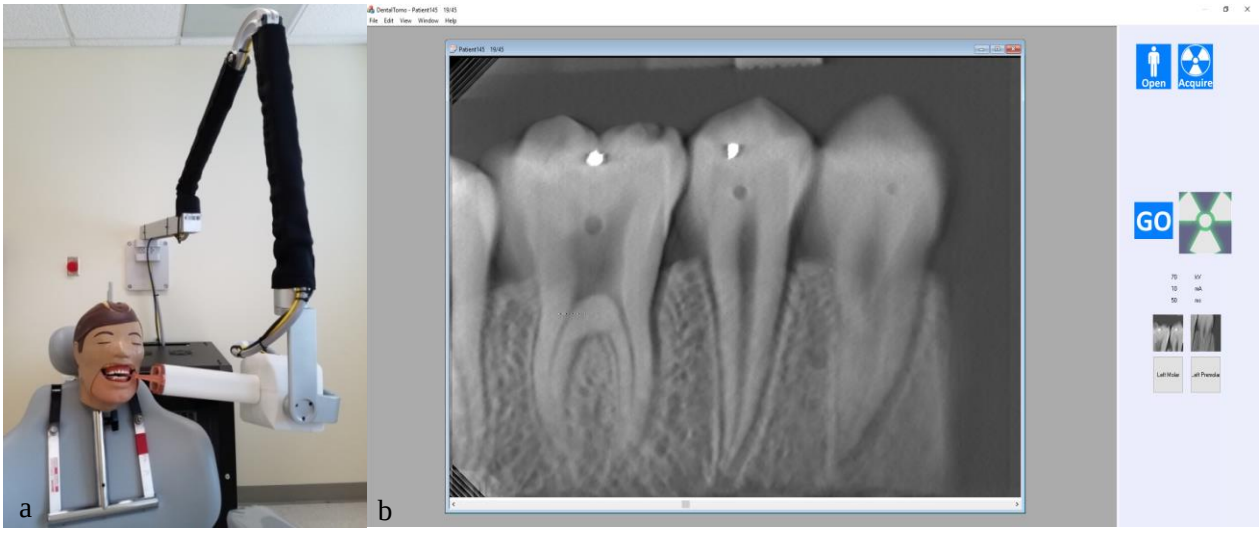

Figure 3-6: a) The first generation s-IOT clinical prototype (XinVivo, Inc.) installed in the UNC Dental Clinic. b) The s-IOT graphical user interface (GUI) for image acquisition.

3.3.1.1 The CNT x-ray source array

The s-IOT x-ray tube is similar to a conventional dental tube in terms its physical appearance, dimensions, tube voltage, and current. However, unlike the standard single source tube, the s-IOT tube contains seven individually addressable, spatially distributed x-ray emitting focal spots, providing an angular span of approximately 12 degrees at the optimized SID of 400mm. The x-ray tube operates at an anode voltage of 70kV, with each x-ray source configured to produce 7mA of tube current. The exit window provides 2mm of aluminum filtration. These parameters are similar to those used in conventional 2D intraoral radiography. The beam on-time for each source is variable, producing a range of exposure levels. The source array is equipped with a collimator cone to limit each x-ray exposure to the detector

active area only. Figure 3-7 is a computer-aided design model of the s-IOT source array with the collimator cone and bitewing detector holder.

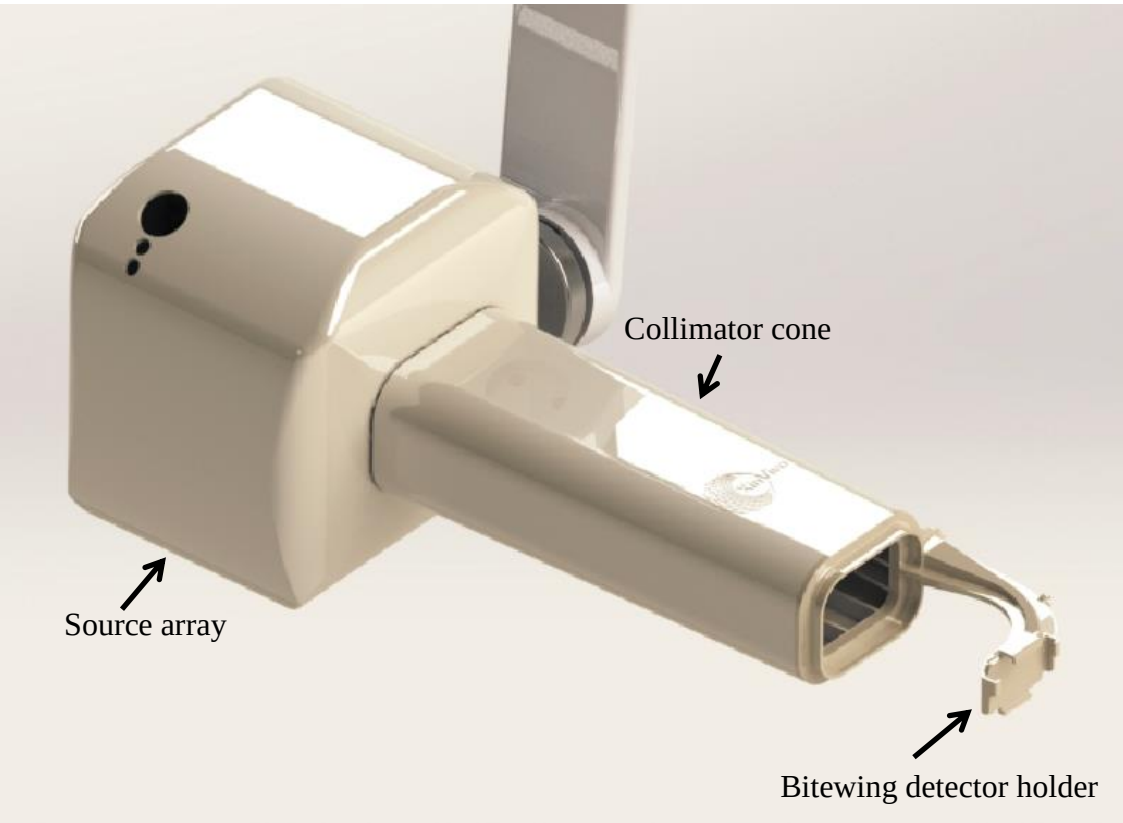

Figure 3-7: s-IOT system computer-aided design model illustrating the source-detector geometry and collimator configuration.

3.3.1.2 X-ray detection

The s-IOT system utilizes an adult (size-2) digital intraoral CMOS x-ray sensor with an active area of 35.52 x 26.64 mm (1920 x 1440 pixels, each measuring 18.5um x 18.5um). The sensor is mounted in a custom holder, which magnetically couples to the end of the collimator cone to maintain the desired source-detector geometric relationship, with a frame rate of 1.3 cycles/second.

3.3.1.3 Geometric calibration

Maintaining a precise alignment and optimized distance between the x-ray sources and detector is critical for tomosynthesis reconstruction. The s-IOT system currently utilizes the manufacturing

specifications of the source array geometry, collimator, and detector holder to define the source-detector geometry.

3.3.2 Image processing

3.3.2.1 Projection image correction

The s-IOT image processing software accepts projection images sequentially from the detector and utilizes a library of previously acquired images to perform gain and offset corrections. The corrected projections are saved and displayed in real time, so that the operator can confirm that the specific area of interest is in the field-of-view (FOV). These corrected projections are used to reconstruct the 3D image space.

3.3.2.2 Reconstruction

The s-IOT system uses a proprietary simultaneous algebraic reconstruction technique developed by XinVivo with a computational time of approximately 10 seconds when performed on a standard PC equipped with a low-end GPU [63]. In this s-IOT system, reconstruction is performed immediately following the scan and displayed for the clinician. The result is presented as a stack of reconstructed image slices through which the reader scrolls. Each reconstruction stack contains 45 image slices, with each slice representing 0.5mm of object thickness.

3.3.3 System characterization

3.3.3.1 Tube current verification

System output of the source array was verified by measurement of the tube current. The amplitude and pulse width was measured for each source in the array with an oscilloscope (TDS2001C, Tektronix, Inc.) using the analog output of the anode power supply. The tube current and pulse width for each x-ray source was measured with an oscilloscope and found to be uniform with nearly square profiles. The average current amplitude was 7.2mA, slightly exceeding the manufacturer-set value of 7mA by <3%. The pulse widths (exposure times) of each source were uniform. Figure 3-8 is a profile plot displaying tube current of each x-ray source when pulsed at 50 ms during a complete tomosynthesis scan.

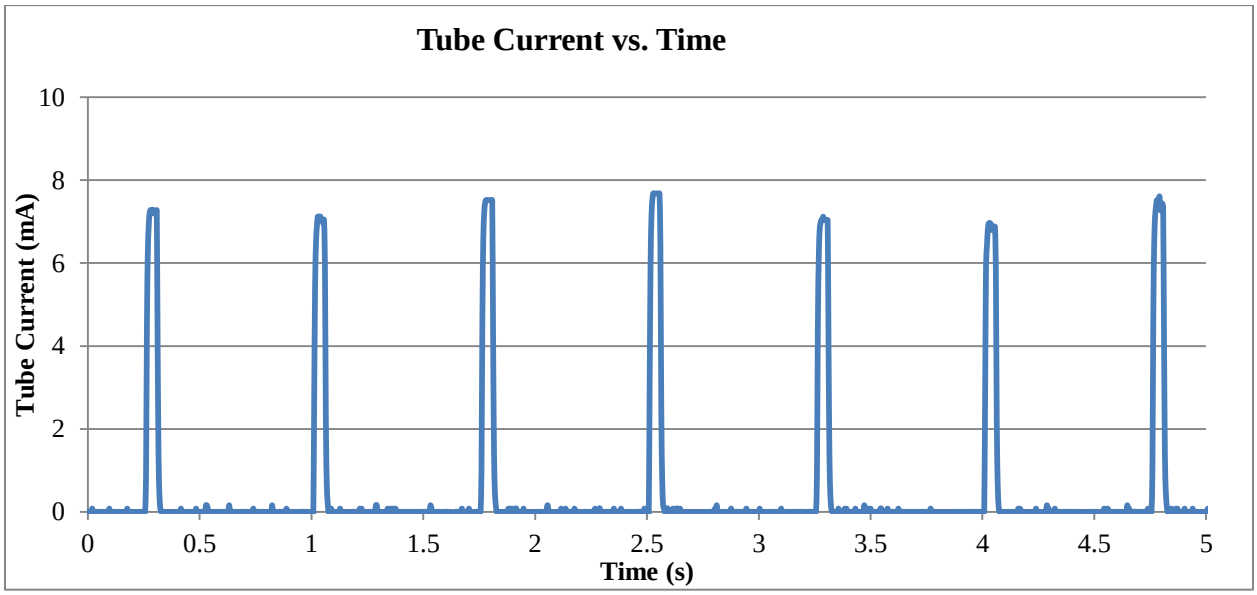

Figure 3-8: Pulse profiles of tube current for each x-ray source in one tomosynthesis scan (50ms per exposure).

3.3.3.2 Focal spot size

The focal spot size of the system was evaluated using a pinhole method similar to IEC 60336. [65] An x-y translation stage was utilized to align a series of apertures (EXVC Collimator Kit, Amptek,

Inc.) to each focal spot in the source array. The source-to-pinhole distance was 4.6cm and pinhole-to-detector distance was 20.7cm, yielding a magnification factor of 4.5. Images were acquired of the magnified focal spot using a flat panel digital sensor (C7940DK-02, Hamamatsu Corp.) with 50 um pixel size. A diagram of the pinhole apparatus is shown in figure 3-9a, with a sample image of the central focal spot shown in figure 3-9b. Plot profiles of the spot in the x-direction (3-9c) and y-direction (3-9d) confirm a slight anisotropy, with the larger dimension in the scanning direction (3-9d). Full-width-half-max (FWHM) measurements of the focal spots averaged 1.00mm in the width (scanning) direction and 640um in the length (orthogonal) direction. The full width at 15% max (FW15%) was also evaluated, as is typically used to cite focal spot size. The average FW15% was 1.34mm in the scanning direction and 1.28mm in the orthogonal direction.

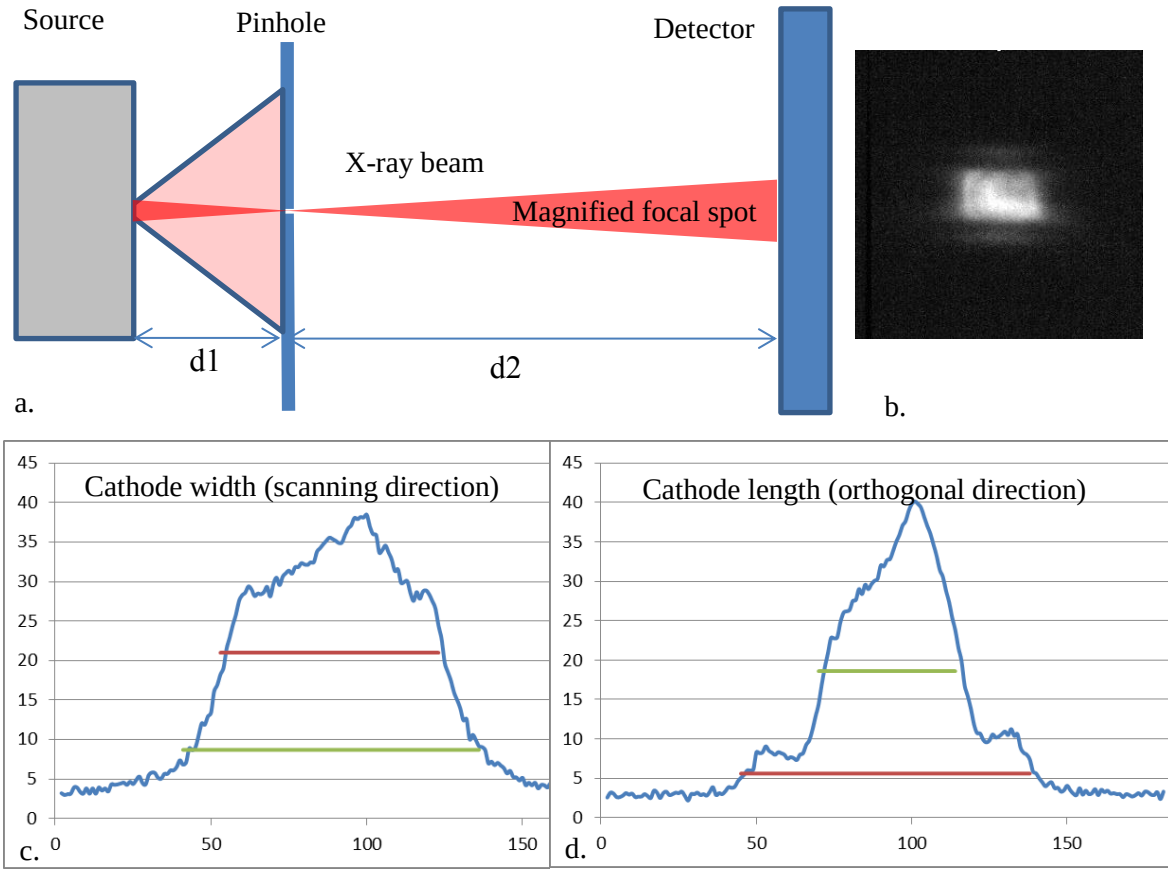

Figure 3-9: a)Diagram of pinhole focal spot apparatus; b) Image of central focal spot in x-ray source array; c) Plot profile in the x-direction (scanning direction); d) Plot profile in the y-direction

3.3.3.3 Resolution

The system resolution was evaluated by determination of the modulation transfer function (MTF) and imaging a line pair phantom. The MTF was determined using a 100um-thick tungsten edge positioned at 1cm from the active detector layer at a slight angulation [66] and imaged in two orientations, both parallel and orthogonal to the spatial distribution of x-ray sources (figure 3-10a). Image gray levels were sampled to define the edge spread function (ESF), from which the MTF curve was calculated and the 10% MTF determined. The line pair phantom (Cardinal Health, Model 07-539) was also imaged in both parallel (figure 3-10b) and orthogonal orientations to the source array at 1cm from the detector surface. The MTF and line pair evaluations were performed on central projection images and plane-of-focus reconstruction slices.

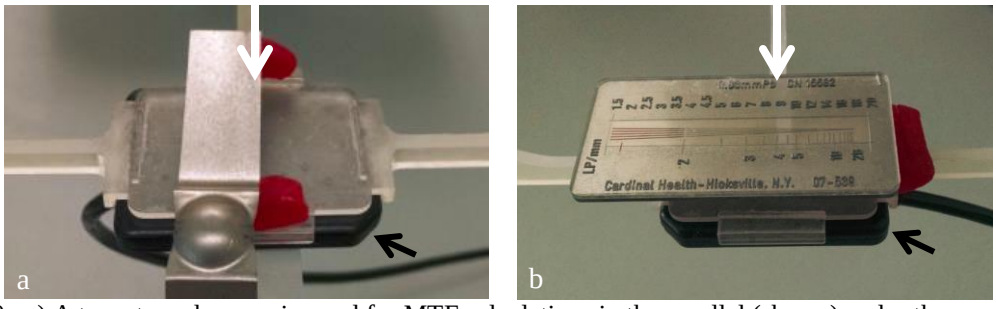

Figure 3-10: a) A tungsten edge was imaged for MTF calculations in the parallel (shown) and orthogonal directions. b) A line pair phantom was imaged to validate image resolution in both parallel and orthogonal (shown) directions. The detector, indicated with a black arrow, is mounted in the specimen holder. The direction of incident radiation is indicated with a white arrow.

The modulation transfer function (MTF) of the system was calculated for both the scanning (parallel to the x-ray source array) and orthogonal directions in both projection images as well as reconstruction slices. The projection images from the central x-ray beam demonstrate a 10% MTF at 9.1 and 9.3 cycles/mm, in the scanning and orthogonal directions, respectively. Similar results were obtained from the peripheral x-ray sources. The 10% MTF in the reconstruction slice containing the in-focus tungsten edge was calculated to be 9.0 and 8.1 cycles/mm in the scanning and orthogonal directions, respectively. MTF plots are shown in figure 3-11 with dashed lines indicating the 10% cutoff value.

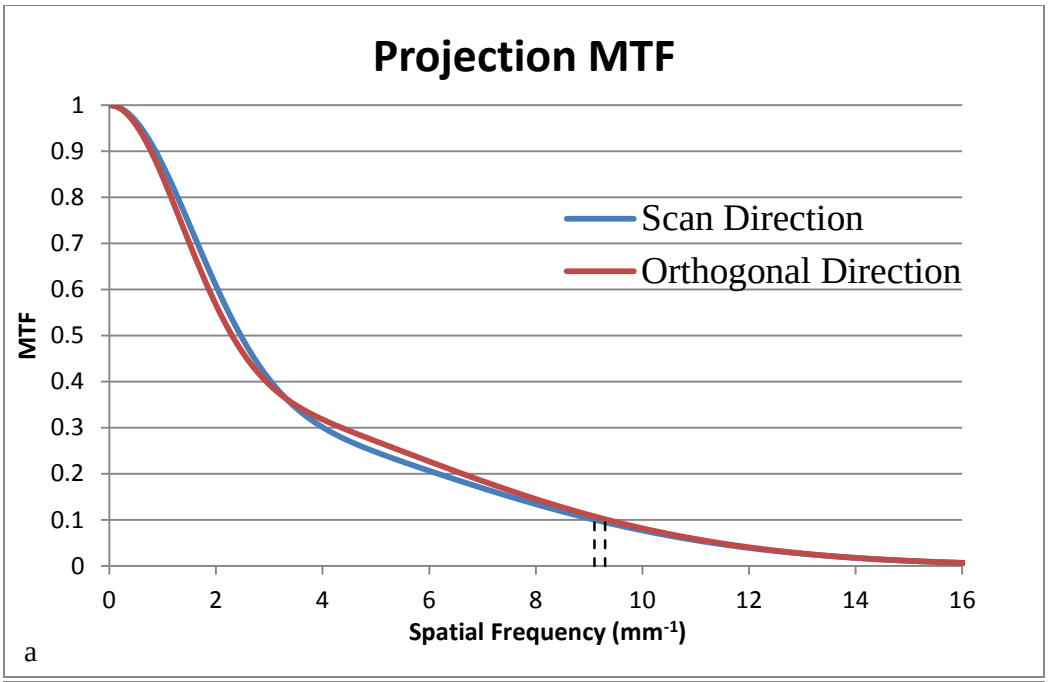

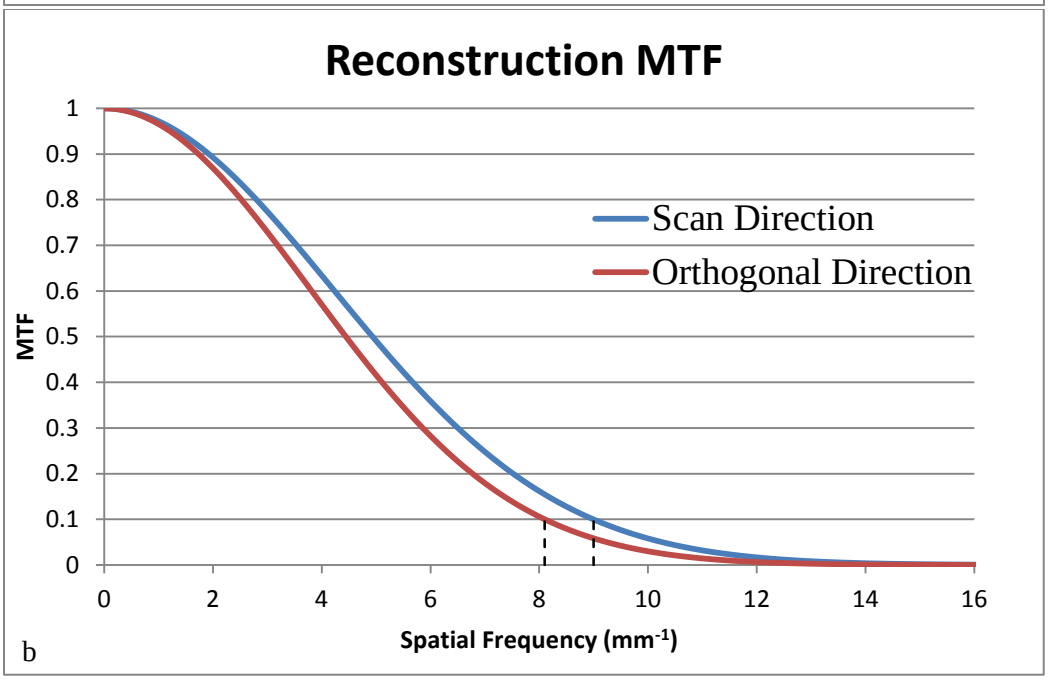

Figure 3-11: Projection (a) and reconstruction (b) MTF in both scan and orthogonal directions. Dashed lines indicate the 10% cutoff values.

From the line pair phantom measurement the system was found to have visual distinction >11 line pairs per mm (lp/mm) in the scanning direction, and >12 lp/mm in the orthogonal direction. Line pair resolution was consistent amongst all projection images of each cohort. The reconstruction slices in which

the phantom was in-focus were also assessed and found to have >8 lp/mm in both the scanning and orthogonal directions. Figure 3-12a shows a sample line pair projection image (inverted) with a region of interest defined at 11 line pairs, approaching the upper limit of line pair distinction. A plot profile of this region reveals local contrast of approximately 10% (3-12b).

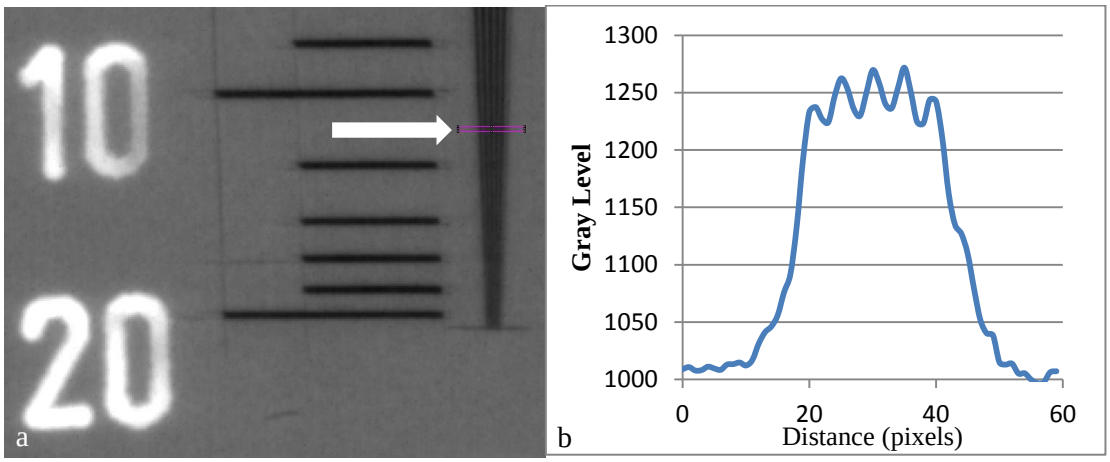

Figure 3-12: a) Cropped projection image of the line pair phantom, oriented orthogonal to the scanning direction. The arrow indicates the region of interest at 11 line pairs per millimeter, corresponding to the plot in figure b.

3.3.3.4 Dosimetry

Dosimetric characterization was carried out using a dosimeter (Accu-Pro, Radcal Corporation). An accessory sensor (Accu-kV, Radcal Corporation) and aluminum standards were used to measure the half-value layer (HVL) to verify the presence of adequate beam filtration and appropriate tube voltage. Actual pulse widths and skin entrance doses were measured using an ion chamber (Model 10x6-6, Radcal Corporation) with digitizer (Model 9660, Radcal Corporation). The system was evaluated at a constant tube current of 7mA, with exposure times ranging from 25-100ms per source. The skin entrance dose was measured for each beam when pulsed at 50 and 100ms. A clinical 2D intraoral x-ray source was also evaluated in order to validate the s-IOT exposure levels.

3.3.3.4.1 Half-value layer

The HVL of the source array was measured using the dosimeter with kilo-voltage accessory with aluminum standards and found to be 2.9mm of aluminum.

3.3.3.4.2 Tube voltage verification

The dosimeter with kilo-voltage accessory was also used to verify that the tube voltage meets the setpoint of 70kVp.

3.3.3.4.3 Pulse width verification

The ion chamber was used to measure the actual pulse width of the x-ray beam at each output setting, confirming accurate beam on-time for each of the seven sources (Table 1).

Table 1: Pulse width

Pulse Width Setting (ms)	**Measured Pulse Width (ms)**
25	25.2
30	29.8
35	36.2
40	40.2
45	44.9
50	50.1
100	99.8

3.3.3.4.4 s-IOT dose

The entrance and exit dose was also measured for each of the seven x-ray beams when pulsed at 100ms. To ensure proper positioning, a custom detector holder was fabricated to ensure proper alignment of the ion chamber to the primary beam (Figure 3-13). Dose was measured with the ion chamber placed on the anterior surface of the detector to determine entrance dose and posterior surface for exit dose. For

the 100ms pulse width setting, the average entrance dose was 49.1mR per pulse with a cumulative dose of 344mR. The average exit dose was 1.1mR per pulse with a cumulative dose of 7.7mR.

a

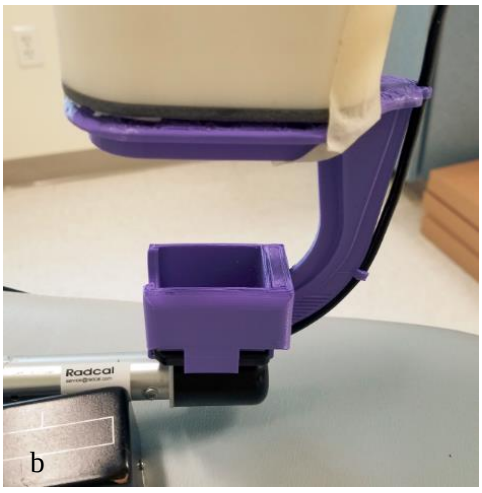

b

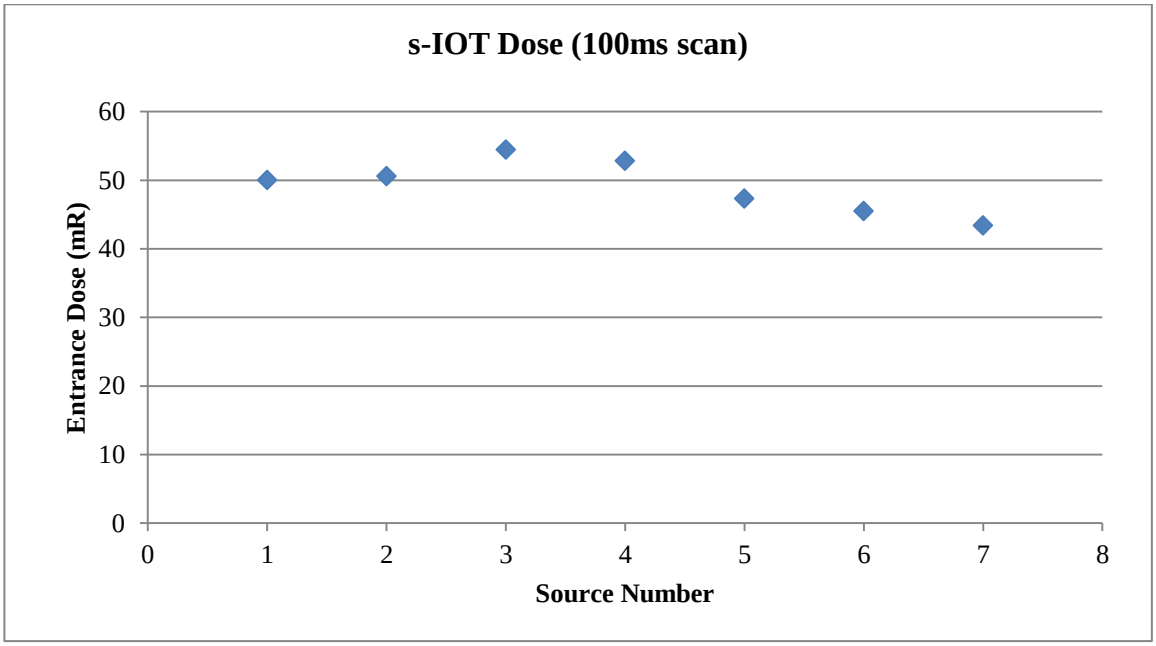

c

Figure 3-13: a) Radcal ion chamber placed in primary beam for entrance dose measurement and b) behind the detector for exit dose measurement. c) A plot of entrance dose values for each source at 100ms pulse width.

3.3.3.4.5 Dose validation

To ensure that the s-IOT system provided a clinically appropriate exposure range, dose validation was performed with a 2D clinical intraoral x-ray source. The 2D system (Instrumentarium Focus, Intrumentarium Dental, Charlotte, NC) includes both a short circular and long rectangular collimator cone and can be used at a wide range of source-to-object distances (SOD) and exposure levels. To establish a dose range, the system was operated in multiple configurations and distances. A PSP with an extension cone paralleling (XCP) positioning device was used to define the clinical SOD and for exit dose measurement. Figure 3-14a is a photo of the 2D system. Figure 3-14b shows the ion chamber placed beneath the rectangular collimator with the XCP device used to define the location for measuring entrance dose. Figure 3-14c shows the configuration for exit dose measurement, with the PSP plate positioned in a bitewing holder. Figure 3-15 is a plot of the measured entrance dose values for the s-IOT and 2D system. The broad dose range of the 2D intraoral system is mimicked by the s-IOT device when operated at pulse widths from 40ms to 100ms per projection. The s-IOT acquisition software has been updated to provide clinical exposures exclusively in this range.

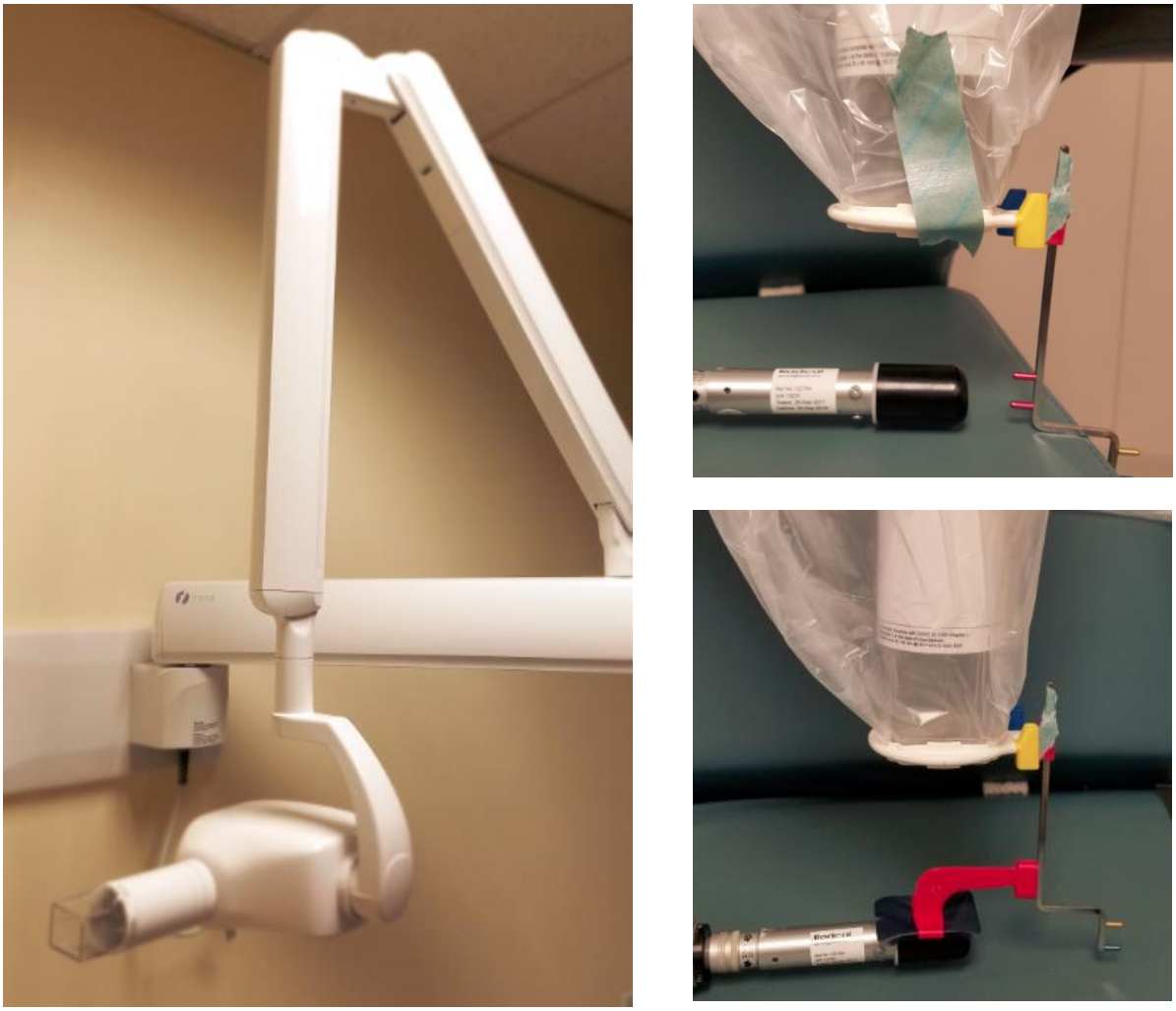

Figure 3-14: 2D intraoral system (a) used for dose validation with ion chamber positioning for entrance (b) and exit (c) dose measurement.

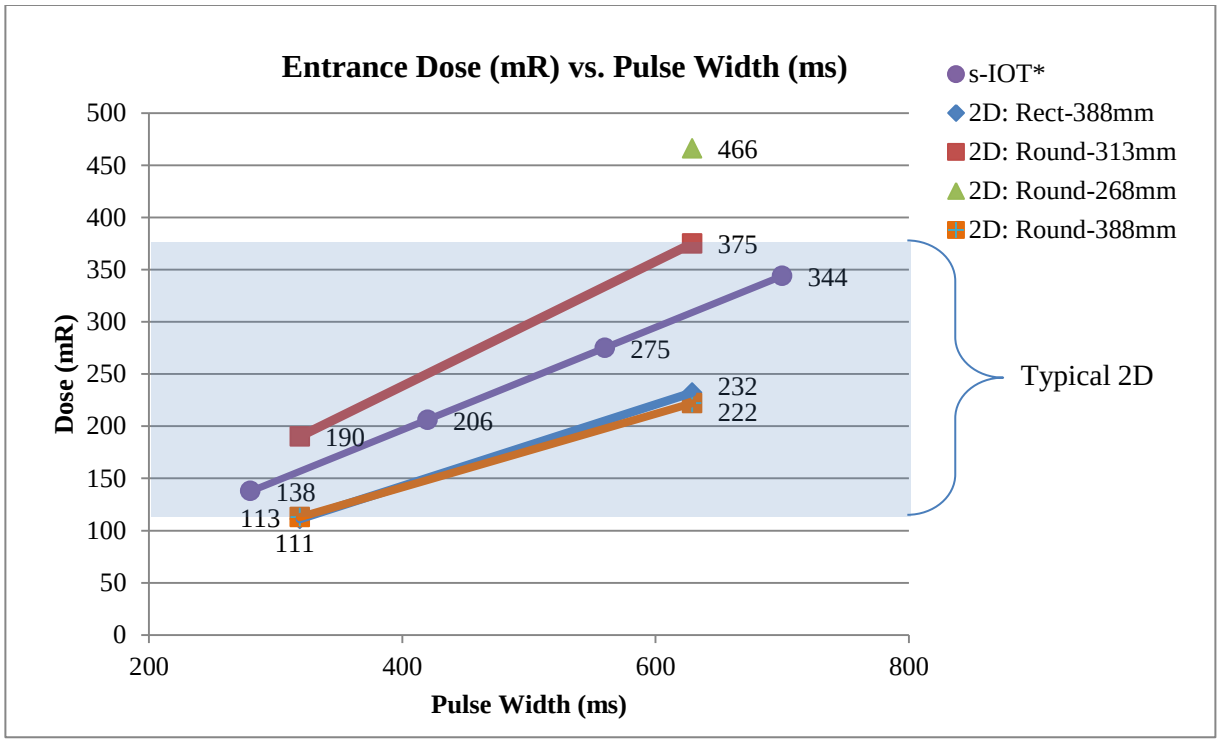

Figure 3-15: Plot of entrance dose vs. total pulse width for 2D and tomosynthesis scans

3.3.4 Implementation

System fabrication and characterization were followed by evaluation of components and software to ensure reasonable clinical workflow. Our team served as an interface between the dental radiologists and engineers to cycle feedback and recommend software and hardware modifications.

3.3.4.1 User interface

The GUI system acquisition software was designed by XinVivo incorporating input from our research team and dental radiologists regarding current 2D clinical workflow techniques for bitewing imaging. Through repetitive usage of the software for specimen and phantom imaging, our team served as the debugger to find and isolate possible problems and recommend modifications. This software was revised in several iterations to reduce potential user errors, data loss, system damage, and patient

overdose. The final product is now a robust application that is easy-to-use and provides safeguards against the most common user issues.

3.3.4.2 Reconstruction optimization

The ultimate success of the system as a clinical device relies on the generation of high quality end product, the reconstruction slice images. Correct implementation of the reconstruction algorithm requires input of carefully formatted projection images and precise geometric relationships between source and detector. The integration of the reconstruction algorithm into the image acquisition software initially introduced some quality issues due to image handling and geometric calibration. Our team worked to find the source of those issues and assist with software updates to substantially improve upon the quality of reconstruction images.

3.3.4.3 Regulatory compliance

Prior to patient studies, it was imperative to assure the system was in compliance with all state and federal regulations for radiation safety. At UNC, the reigning authority is the Radiation Safety Division in the Department of Environment, Health, and Safety (EHS). Consultations were made with Mark Brueckner of EHS to evaluate the system and ensure adequate implementation of safety measures.

EHS regulations dictate that the x-ray system required an audible tone to sound during beam on-time. Because this function was not provided with the system, our team worked to develop an electronic circuit to produce a tone during each x-ray pulse.

An area survey was performed to map the scattered radiation within the imaging room and in the hallway. The system was found to be properly shielded and did not put the technician or general public at risk of increased exposure in comparison to a standard 2D intraoral clinical system.

3.3.4.4 Training

In preparation for patient trials, our team has developed a standard operating procedure (SOP) and trained four dental radiologists to operate the s-IOT system.

3.3.5 Imaging

The potential clinical utility of the s-IOT system was explored over a range of dental pathologies (Figure 3-16) by imaging the RMI dental quality assurance phantom (a) , extracted human teeth (b and c), and a Dental X-ray Teaching and Training Replica (DXTTR, Dentsply Rinn Corporation) (d). The tomosynthesis projection images were acquired at 70kV with each source driven at 7mA for 50ms per projection resulting in an x-ray on-time of 350ms for one complete tomosynthesis study. This exposure is within the range of exposure used for a single bitewing image acquisition at the UNC School of Dentistry Oral and Maxillofacial Radiology Clinic. For imaging phantoms and loose specimens, the x-ray assembly was oriented vertically and the phantom or specimen was placed on the upper surface of a detector holder designed specifically for this purpose (Figure 3-18a).

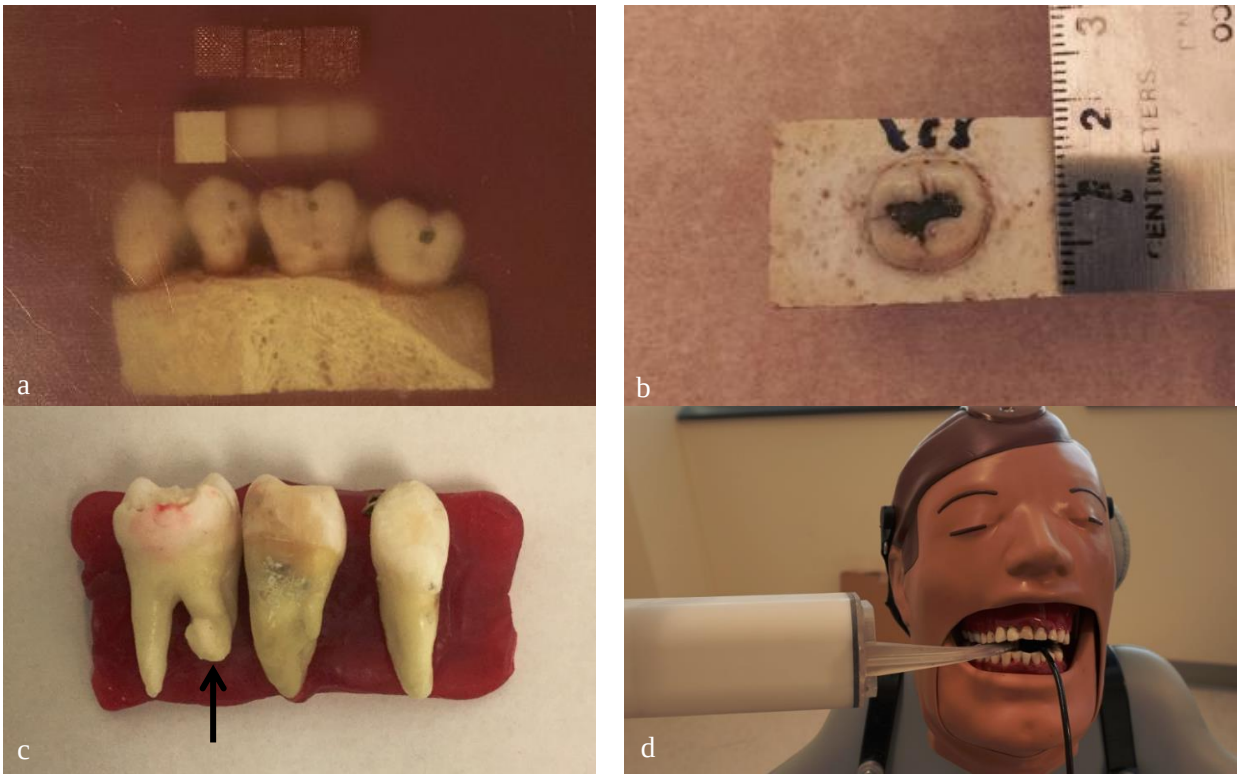

Figure 3-16: Photos of the RMI phantom (a), a specimen containing fractures (b), and dilacerated roots (c). DXTTR, containing caries and other dental lesions, shown with the s-IOT source positioned for right molar bitewing imaging (d).

3.3.5.1 RMI Phantom

The RMI phantom (figure 3-16a) contains three segments of metal mesh, four thicknesses of bone mimic, and a human maxillary specimen with teeth containing metallic fillings and simulated caries lesions.

Images of the RMI phantom are shown in figure 3-17. A 2D radiograph is shown in figure 3-17a. Though not apparent in the 2D image, the central and right teeth in the RMI phantom each contain three roots, two buccal roots and one palatal root. Figure 3-17b is a drawing of such a molar to clarify this geometry. When viewed distally, the dashed lines represent the tomosynthesis reconstruction slice locations in figures 3-17c and 13-17d. Figure 3-17c is the slice in the plane of the caries lesions and allows visualization of the buccal roots of the first molar. Figure 3-17d is 15 slices (7.5mm) posterior and

is in the plane of focus of the palatal root of the first molar tooth. A Y-shaped crown fracture (white arrow) is revealed in the central tooth that is not visible in the 2D image or upper reconstruction slice.

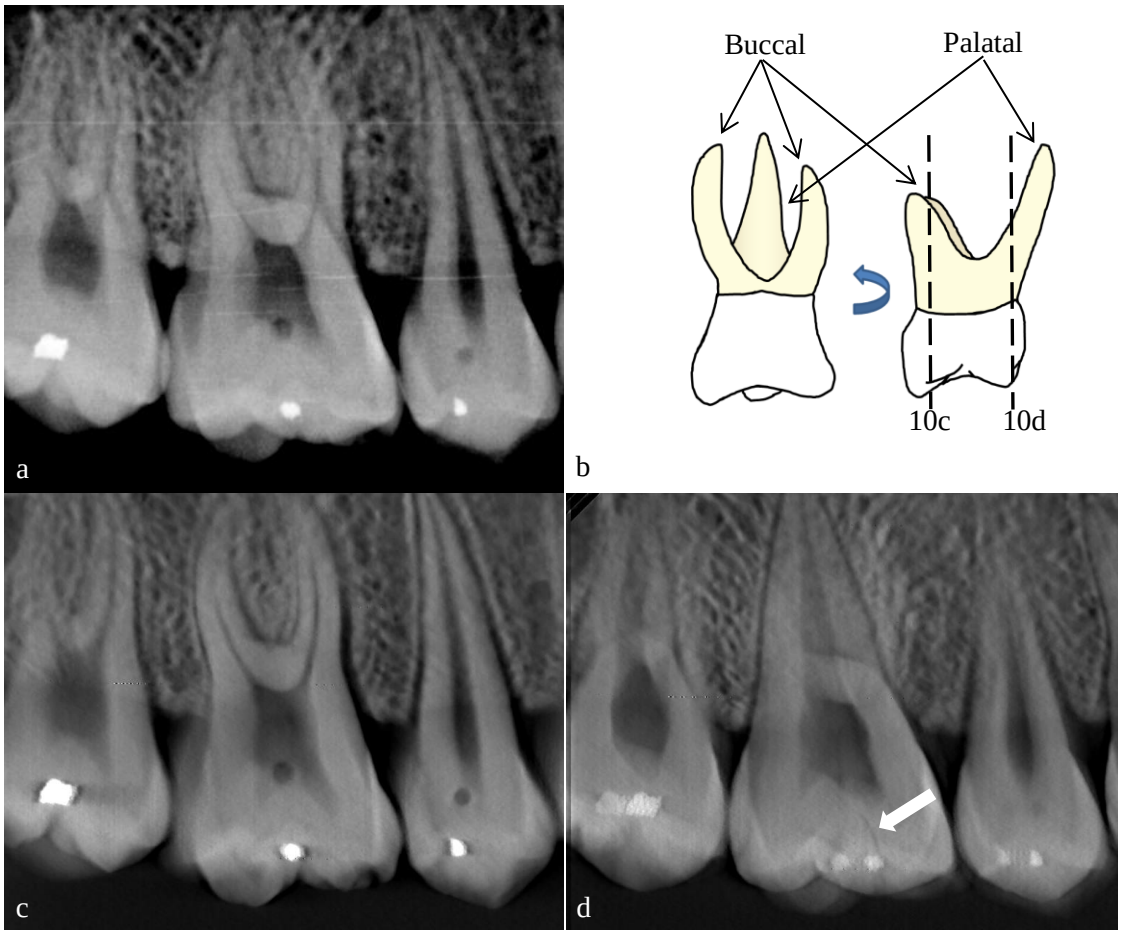

Figure 3-17: a) 2D image of the RMI phantom; b) Drawing of a molar containing three roots; dashed lines indicate planes of focus for reconstruction slices in c) and d); c) Reconstruction slice in the plane of the buccal roots, simulated caries lesions, and metallic restorations; d) Reconstruction slice in the plane of the palatal root and a crown fracture (arrow).

3.3.5.2 Root fracture specimens

Figure 3-18b is a photo showing the occlusal surface of a fracture-containing tooth specimen embedded in alveolar bone analogue prepared by our collaborators at the University of Minnesota (UMN) School of Dentistry. The analogue consisted of a plaster/walnut mix to account for attenuation due to bone and simulate marrow spaces. A 1cm slab of dental wax represented soft tissue attenuation.

Similarly prepared root fracture specimens (figure 3-18c) were also imaged in multiple orientations to assess fracture conspicuity at various viewing angles. Two different sample orientations are displayed in figure 3-18. For comparison, standard 2D images were acquired using a clinical 2D intraoral system (Instrumentarium Focus, Intrumentarium Dental, Charlotte, NC) and a PSP plate receptor, with exposures optimized by an expert dental radiologist over a range from 320 to 500ms at the same kV and mA.

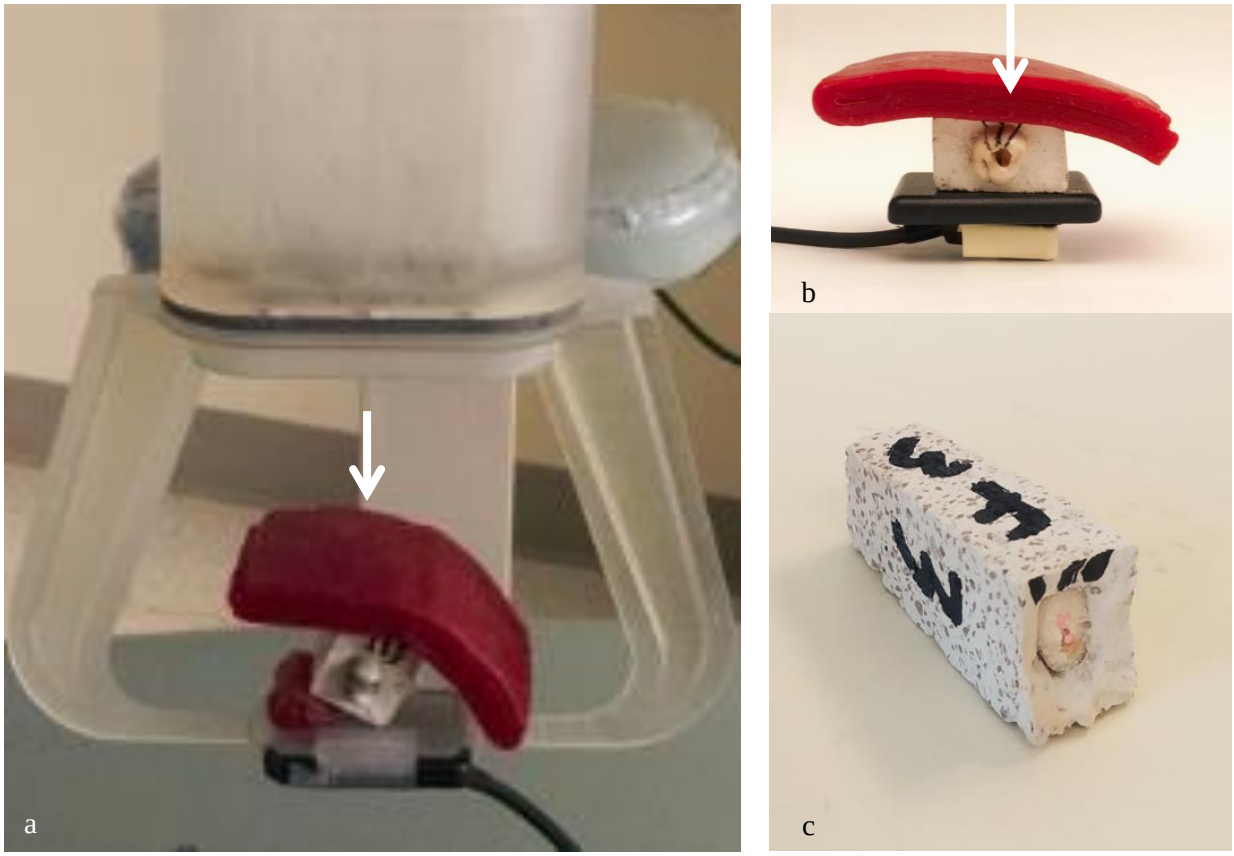

Figure 3-18: a) System configuration for phantom and specimen imaging;
b) specimen covered with a soft tissue mimic and placed on detector. The direction of incident radiation is indicated by the white arrows; c) obturated premolar root mounted in alveolar bone mimic

Specimens with root fractures prepared at the UMN School of Dentistry were imaged at the UNC School of Dentistry with both 2D intraoral radiography and s-IOT. Though tomosynthesis scans were performed with several sample orientations, the following images are from the standard scanning configuration, with the sample placed flush on the detector and the scanning direction orthogonal to its long axis (figure 3-18b). Two example specimen images are shown in figure 3-19. Figures 3-19a and 3-

19b are 2D images of the two root specimens, with the corresponding reconstruction slices shown in figures 3-19c and 3-19d. Though the 2D images were taken with a much longer exposure, 500ms, the root fractures are subtle and could be mistaken for adjacent root canals. The reconstruction slices exhibit higher contrast and excellent delineation of the fractures. Scrolling through the reconstruction stack allows the viewer to visualize the propagation of the fracture through the root.

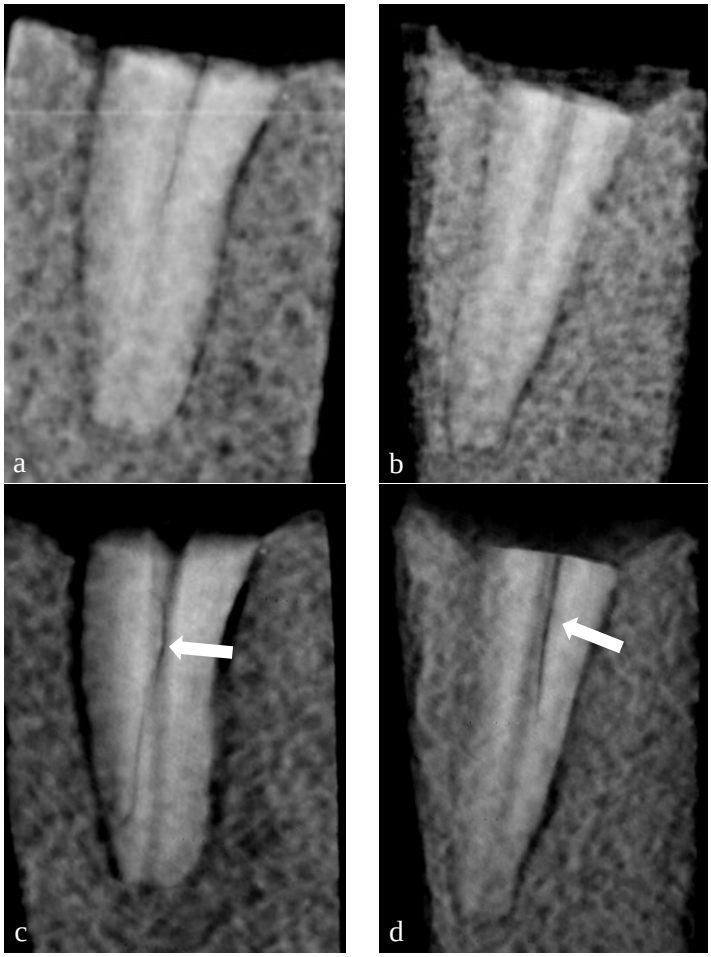

Figure 3-19: a, b) 2D images of root fracture specimens; c, d) Corresponding reconstruction slice images reveal well defined fractures indicated by arrows.

3.3.5.3 Dilacerated root specimens

Nearly all teeth have some amount of curvature, and such dilacerations can range from slight to severe. Dilacerated roots are not an unusual finding in patient images. Assessing the direction and

degree of dilacerations is critical in the delivery of endodontic treatment, orthodontic movement, or surgical intervention. Tomosynthesis is promising in these regards. Figure 3-16c shows the dilacerated root specimens, one with an extremely curved root (arrow). Figure 3-20 contains sample images of that specimen. The 2D radiograph is shown in figure 3-20a. The tooth contains obvious root dilacerations, but the direction and degree of curvature are unknown due to the lack of depth information. Figures 3-20b and c are the corresponding reconstruction slices. Figure 3-20b is a slice in the plane-of-focus of the root canals and pulp and figure 3-20c is six slices (3mm) anterior in the plane-of-focus of a well-defined root tip protruding toward to the x-ray source array, referred to as the buccal direction.

Figure 3-20: a) 2D image of a dilacerated root specimen; b, c) Reconstruction slice images of the same specimen in different planes of focus, indicating orientation in a buccal direction

3.3.5.4 Interproximal contacts

Dental clinicians rely heavily on radiography to inspect areas which are inaccessible to visual examination, which are also prone to decay. The interproximal contacts, or spaces between adjacent teeth, are of particular interest in routine screening. Dental radiographs should contain a clear view of each tooth surface with no overlapping, referred to as an open contact, which requires careful source-receptor positioning. [3] Poor positioning can necessitate retakes and imparts additional dose to the

patient. The ability to reduce or remove superposition is a key benefit to tomosynthesis, and may effectively eliminate closed contacts and retakes.

A reader study for contact visualization was initiated in which 11 DXTTR manikins were imaged with 2D intraoral and s-IOT. The DXTTR phantoms contain cadaveric dentition with various lesions and are equipped with a mechanical bite apparatus. Figure 3-16d is a DXTTR training phantom positioned for bitewing image acquisition utilizing a bitewing detector holder.

A comparison between sample 2D bitewing images and corresponding reconstruction slice images is shown in figure 3-21. The 2D bitewing images were acquired with a clinical adult size digital sensor (Schick Maximus, Sirona Dental, Long Island City, NY) and display a larger FOV. Figures 3-21 and 3-21b are the 2D images of the molar and premolar regions, respectively. The corresponding reconstruction slices are shown in figures 3-21c and 3-21d. The 2D image of the molar region (a) reveals a vertical crown fracture in a maxillary molar, indicated with an arrow. The corresponding reconstruction slice (c) displays the same fracture, but with higher contrast, and displays an additional fracture in the second right mandibular molar. The 2D image of the premolar region (b) reveals two fractures in one mandibular molar and one premolar. This image also displays five closed contacts (circled), in which the interproximal surfaces are superimposed and cannot be viewed individually. The corresponding reconstruction slice image (d) reveals an additional fracture in the first molar. The elimination of superposition in the slice image also opens the contacts for independent visualization of each interproximal surface.

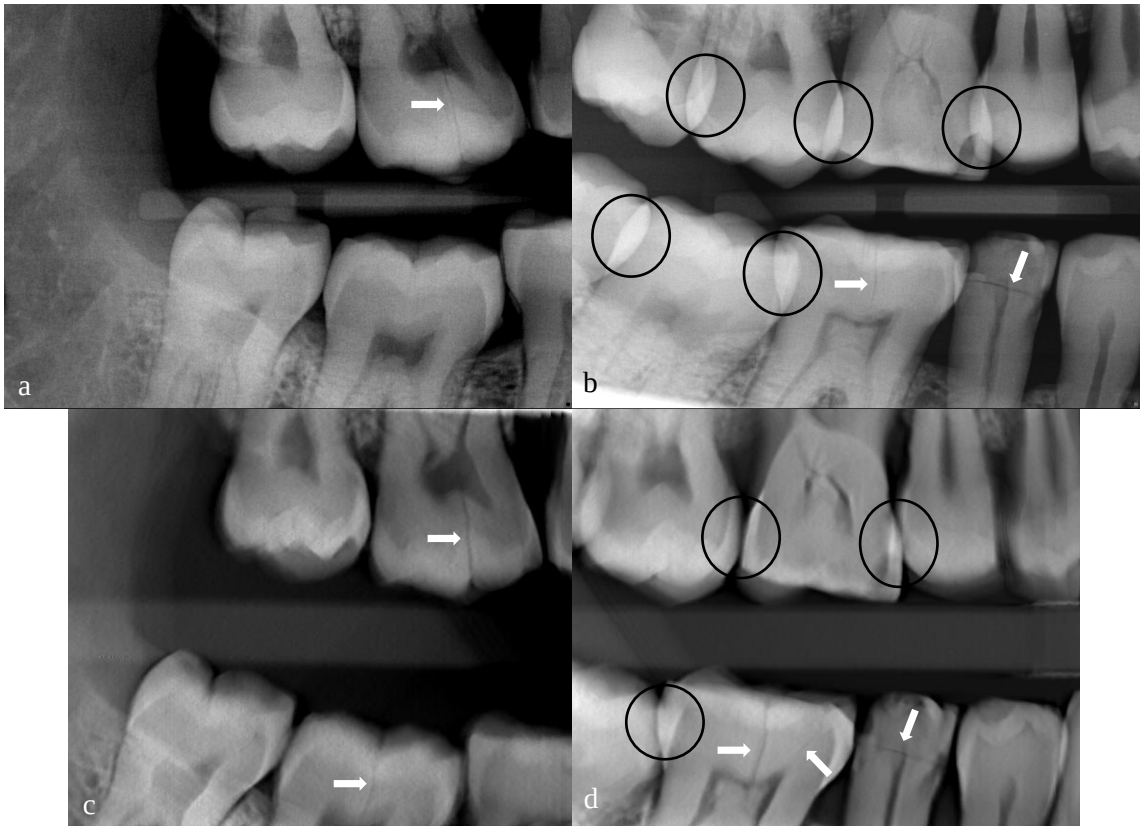

Figure 3-21: 2D images (top) and reconstruction slice images (bottom) from DXTTR bitewing acquisition. Reconstruction slices reveal more fractures (arrows), with higher contrast. Interproximal superposition (circled) in the 2D premolar image (b) is eliminated in the corresponding reconstruction slice (d).

3.3.5.5 Occlusal caries

Though visible in an oral examination, the occlusal surface of teeth can be challenging in diagnosis of caries. The occlusal terrain consists of cusps, often with pits, fissures, and stains. In a 2D radiograph, the cusps are superimposed and the relatively high radiopacity of the enamel can obscure early stage, or incipient caries. [3] If undetected, the decay will progress through the enamel into the softer dentin, and can rapidly reach the pulp cavity, requiring endodontic treatment.

s-IOT has the potential to eliminate superposition of cusps and enamel in the occlusal plane and may increase sensitivity to carious lesions. In order to assess the sensitivity of s-IOT, bitewing imaging was performed on sixty extracted human specimens mounted into dental typodonts. The specimens are part of a multi-modality study for occlusal caries detection currently in progress in the UNC SOD and

have also been imaged with a 2D intraoral source, CBCT, and micro-CT. Ground truth for the study will be provided by histological analysis. s-IOT images provide good visualization and depth resolution in which subtle radiolucencies in near the occlusal surface are observed. Figure 3-22 shows sample s-IOT reconstruction slices through different regions of the same speciment. Arrows indicate subtle radiolucencies at the dentino-enamel junction that may be carious lesions. Though imaging results for the other modalities investigated in this study are not yet available for comparison, this example demonstrates the ability to isolate tooth cusps within a sample for individual inspection.

Figure 3-22: Occlusal caries reconstruction slices suggesting presence of carious lesions (arrows) in two different reconstruction slices of the same specimen.

3.3.6 Discussion

3.3.6.1 Tube Current

The tube current was measured with high temporal accuracy on an oscilloscope and found to have a very uniform pulse width. The amplitude displayed some source-to-source variation and the average was slightly higher than the target of 7mA, at 7.2mA (<3%). This result is repeatable and therefore does not imply any instability in the tube, but rather is a result of the precision of the current version of the prototype electronics.

3.3.6.2 Dosimetry

The anode voltage was verified to be within 1% of the specified value of 70kVp. The HVL of the beam was measured to be 2.94 mm Al, satisfying the regulatory requirement of HVL >1.5mm Al for 2D intraoral sources. [67] The pulse width (exposure time) was accurate for all seven exposure settings. The largest deviation noted was 3%, with all other measurements falling within 1% of the desired width.

The skin entrance dose was measured at the highest pulse width setting allowed by the acquisition software, 100ms per source. Some source-to-source dose variation was observed that mimics the variation displayed in the tube current. At the highest exposure setting, the skin entrance dose produced by the system is 344mR, and is similar in dose to a single clinical 2D PSP exposure in the UNC School of Dentistry. The maximum exposure setting of 100ms per pulse is designed to examine the utility of s-IOT at doses clinically acceptable for 2D screening. The present dental CNT x-ray source array has the capability of achieving pulse widths greater than 200ms per pulse.

3.3.6.3 Resolution

The s-IOT system resolution was characterized by calculation of the MTF as well as imaging of a line pair phantom. The MTF values for projection images displayed a slight variation with respect to scan direction. The images of the line pair phantom also reflected this variation, indicating higher resolution in the direction orthogonal to the linear source array. The MTF values for reconstruction slices displayed a larger direction-dependent variation. This variation is due to edge enhancement resulting from metal artifacts in the scan direction. The artifact is easily visualized as bright streaking in reconstruction images and is more pronounced compared to the anatomical images due to the high attenuation of the phantoms. A more accurate measurement of resolution in the scan direction could be made with implementation of an artifact reduction technique, or use of an alternative reconstruction method, but would not reflect the actual algorithms of this clinical prototype system. Work is underway to mitigate the effects of metal artifacts from dental amalgams in patient images.

The system resolution in the reconstruction slices is affected not only by the inherent properties of the detector and X-ray source, but also the geometric calibration of the system. Precise location of the seven focal spots with respect to the detector center is required by the reconstruction algorithm. This geometry is currently defined by the manufacturer based on design values and is not measured for each scan. It was noted during DXTTR imaging that the large amount of biting force placed on the bitewing holder, coupled with the rigidity of the DXTTR mounting structure, caused some torsion in the holder. This was also noted by presence of the collimator edge in the projection images and inevitably caused some small deviation in the actual source/detector geometry compared to the design values. A more rigid bitewing holder could be implemented for patient use, although the patients will have more degrees of freedom than the fixed mounting bracket of the DXTTR. The actual impact of mechanical deformation on image quality will be assessed during patient trials.

3.3.6.4 Image quality

Various dental models were imaged to demonstrate the conspicuity of dental anatomic features and pathoses. The results shown in this study are examples of potential clinical applications. Reader studies are in progress for several of these lesion types and will better clarify the diagnostic efficacy of s-IOT.

3.3.6.4.1 RMI Phantom

Images of the RMI phantom displayed good visualization of the simulated caries lesions, fractures, buccal and palatal roots. In 2D periapical imaging, buccal and palatal roots overlap which can complicate their independent visualization. The mandibular bone displays good contrast of alveolar

porosity and implies possible application in evaluation of periodontal bone loss and other disorders presenting as subtle radiolucencies. [3]

3.3.6.4.2 Fractured Root Specimens

Root fracture detection in 2D intraoral radiography is difficult due to the superposition of bone, presence of endodontic obturation materials, and other tooth roots. Root fractures themselves can only be visualized when the fracture plane happens to be parallel to the direction of x-ray propagation [3]. If a fracture is left untreated, the condition will worsen and can lead to severe periodontal problems and tooth loss.

The fractured root specimens were imaged with the x-ray scanning direction at different orientations with respect to the longitudinal axis of the root. Sixty specimens have been imaged on this system for a reader study, currently underway at the UMN School of Dentistry, to assess the sensitivity of the s-IOT for root fracture identification compared to 2D and CBCT imaging modalities. For these two particular specimens shown, the fractures were easily visualized in the reconstruction slice images compared to the corresponding 2D radiographs. The reconstructed images presented in this work were obtained from tomosynthesis scans performed in the standard orientation, with the sample flat on the detector and scanning direction orthogonal to the root axis. Inspection of reconstruction images revealed that varying the sample orientation with respect to the source array provides additional information about the specimen, and multiple-view tomosynthesis may prove to be a valuable resource for diagnostic imaging. Geometrical relationships, including relative depth and direction of propagation of the fractures, are also easily accessible when viewing the entire reconstruction stack. The fractures are also typically visible in at one or more of the basis projection images due to the range of angulation. s-IOT may increase the likelihood of fracture detection by acquiring images from many angles compared to a single 2D intraoral radiograph.

3.3.6.4.3 Dilacerated Root Specimen

Dilacerated roots are a concern in endodontic treatment, orthodontic movement, or surgical extraction. Lack of awareness of the severity and direction of curvature can lead to complications during such procedures. The sample images of the dilacerated root specimen clearly show that the root is curved and extends six slices (>3mm) from the expected location. The contrast in the reconstruction image is excellent, although the specimen was not mounted in bone-simulant and contained only a few millimeters of simulated soft tissue. Not only does s-IOT depict the severity of curvature, but it also provides information about direction of curvature in three-dimensional space that 2D imaging may omit.

3.3.6.4.4 Interproximal contacts and caries detection

The DXTTR bitewing reconstruction slice images demonstrate good visualization of anatomical detail, including some crown fractures. Scrolling through the reconstruction stack allows the reader to open the contact points between the teeth, effectively removing the acquisition error. Conventional interproximal caries detection relies on proper positioning to ensure open contacts and improper positioning can result in retakes of 2D radiographs. The use of s-IOT for interproximal caries detection may eliminate the need for retakes by producing pseudo-open contacts. An observer study in the UNC SOD has been conducted on this data set and revealed a substantial decrease in contact overlap for s-IOT compared to 2D intraoral radiography. [68]

In viewing the reconstruction stack, the tooth cusps are also easily isolated among different reconstruction slices. Early stage, or incipient occlusal caries are difficult to detect with 2D intraoral imaging due to the superposition of tooth cusps. Ex-vivo reader studies for interproximal and occlusal caries detection are currently under way at the UNC School of Dentistry.

3.3.6.4.5 Image contrast and dose

In all image sets, the tomosynthesis reconstruction slices provided more anatomical detail with higher depth resolution and feature conspicuity than the 2D counterparts. Information can be gleaned from the reconstruction data that is not available in the 2D images, such as depth or direction of propagation of a fracture.

Bitewing s-IOT imaging of the DXTTR provides the closest approximation to in-vivo patient imaging and incorporates additional challenges over loose specimen imaging. The anthropomorphic design allows use of the bitewing detector holder for true clinical positioning and the tissue-mimicking vinyl "skin" provides additional attenuation. Structure of the oral cavity, particularly curvature of the jaws, restricts the positioning of the detector holder, often forcing a larger object-to-detector distance (ODD). The ODD can be up to 3cm in the pre-molar region, therefore increasing apparent focal spot size and magnification. The volume of irradiated material is also greater for the DXTTR, including the bitewing feature of the detector holder, generating scattered radiation, which can impact the contrast and resolution. The strong biting force of the DXTTR phantom also produced some deformation of the bitewing detector holder, possibly altering the actual source-detector relationship. Despite these additional factors that could negatively impact the image quality, the DXTTR reconstruction images were very good with crisp visualization of fractures and interproximal surfaces.

The s-IOT clinical prototype system displays good resolution and image quality when operated at 50ms pulse width per projection. The contrast and SNR in the dilacerated root specimen images are slightly better than the other images, as expected due to the lack of bone and tissue attenuation. The maximum exposure setting has been recently increased to 100ms per projection to allow further investigation into image quality and dose optimization for anthropomorphic specimens and patients. This limitation is not a constraint of the system hardware, but as an initial configuration for low dose s-IOT imaging.

The total x-ray exposure time for the tomosynthesis scan now varies from 280ms to 700ms, with a total scan time of approximately five seconds. The limiting factor in scan speed is the detector frame rate. Incorporation of a faster detector is underway and should decrease the imaging time to less than three seconds. The image processing and reconstruction step currently requires approximately 20 seconds. Ongoing enhancement of the reconstruction algorithm will also result in a reduction of computation time.

3.4 Conclusions and future work

The stationary intraoral tomosynthesis clinical prototype has been characterized for dose and resolution. The system is compact and easy to use with a fast scan time and real-time image reconstruction and dose comparable to that of a single 2D intraoral radiograph. Preliminary dental phantom images have been presented and the level of detail visualized in the s-IOT reconstruction slice images suggests that the s-IOT system will increase the diagnostic yield and will be more successful for clinical applications than standard 2D intraoral imaging without an increase in patient dose.

Future work on s-IOT will include dose optimization studies using anthropomorphic phantoms and human specimens. Root fracture specimens will be imaged at increased pulse width for analysis of feature conspicuity and artifact reduction. Our team will provide technical support to the dental radiologists during the patient trial and continue to explore possible applications of s-IOT.

CHAPTER 4: SCATTER IN X-RAY IMAGING

4.1 Scatter in radiography

Chapter one defined the interaction of photons with matter, namely the photoelectric effect and Compton scatter, as the mechanism responsible for x-ray absorption and the ability to create images. Unfortunately, the same interactions that cause absorption can generate unwanted side effects that degrade the image quality and increase patient dose. Recall that Compton photons change trajectory after interaction with an electron. If the trajectory happens to be in the direction of the detector, the photon is counted in an unintended location. The macroscopic effect of photon scatter is a hazy fog in the image.

The number of photoelectric events versus Compton events in a given material changes dramatically over the diagnostic imaging range. Figure 4-1 is a graph of the relative percentages each mechanism contributes, as well as the overall energy percentage. [1] Note the relative percentage of energy imparted by the photoelectric effect does not drop off as quickly as the percentage of interactions. This is because the photoelectric interactions impart all of their energy to the material, whereas Compton interactions do not.

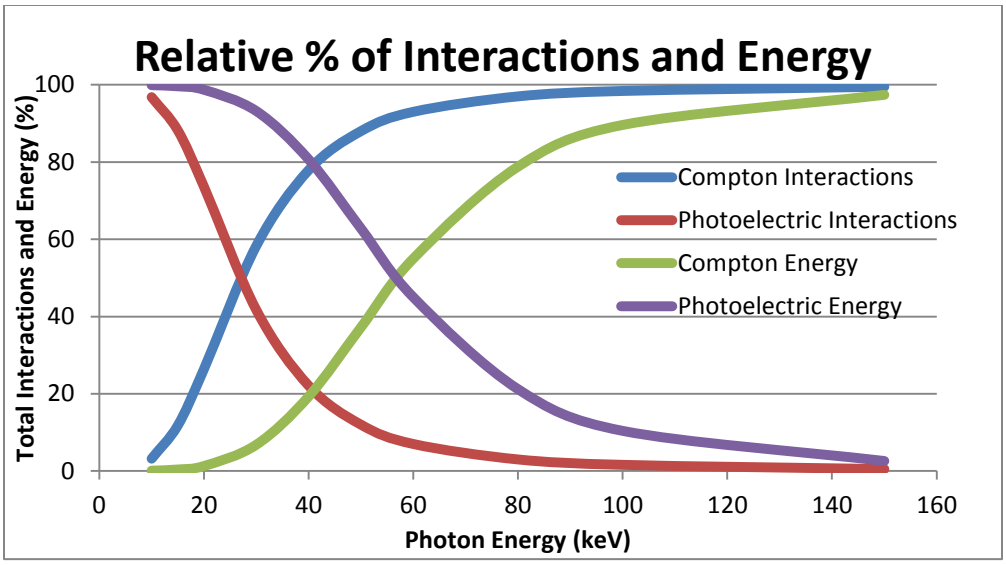

Figure 4-1: Relative percentage of interactions and energy contributed via Compton scatter and the photoelectric effect as a function of incident photon energy. Figure adapted from Prince and Links [1]

4.1.1 Effects of scattered radiation on image quality

Scatter in imaging reduces the image contrast by adding a low frequency signal into the image. In reality, the signal varies according to the object imaged and spectrum of the x-ray beam. To simplify the mathematics, we will assume the signal to be a constant intensity across the image. Local image contrast (C, equation 4-1) can be defined using the intensity of the target and background, I_t and I_b, respectively.

Equation 4-1: $C = \frac{I_t - I_b}{I_b}$

When a constant intensity scatter signal, I_s, is added to the target and background, the new contrast (C', equation 4-2) is reduced.

Equation 4-2: $C = \frac{(I_t + I_s) - (I_b + I_s)}{(I_b + I_s)} = C\,\frac{I_b}{I_b + I_s} = \frac{C}{1 + I_s/I_b}$

The contrast is reduced by a factor of $1/(1+I_s/I_b)$, with I_s/I_b known as the scatter-to-primary ratio. [1] Simply subtracting a constant value from the image intensities would increase the local contrast, but would be inaccurate and would also increase the relative amount of image noise.

4.1.2 Scatter in breast imaging

The presence of scatter is well known and plagues all X-ray imaging systems. In mammography, the scatter-to-primary ratio (SPR) can exceed one in dense breasts. [69] [70] The result of scattered photons is a decrease in the image contrast and signal to noise ratio [71], resulting in reduced image quality and lesion detection. Tomographic modalities, such as CT and tomosynthesis [72] [28] [73] [27] [26], also suffer from scatter.

Physical mechanisms have been devised to reject scatter, such as scanning slot systems and anti-scatter grids. [69] [70] [66] [71] Scanning slot systems utilize a fan beam and linear detector to scan the breast. This method is very effective at rejecting scatter, however it can require much longer scan times, ranging from 3-15 seconds per projection. [74] The current standard technique for mitigating the scatter is to use an anti-scatter grid. The grid reduces scatter, but also impedes primary photon transmission, requiring a larger patient dose to maintain SNR. Despite the dose penalty, linear and cellular grids are commonly used in commercial planar imaging systems. In chest imaging, a grid can reduce the scatter fraction from 70% to 20% in the lung and from 95% to 65% in the mediastinum. [66] Grid use is optional for mammography, employed as needed for dense or large breasts, and can reduce the scatter fraction to approximately 20%. [75] Three-dimensional modalities, such as CT and tomosynthesis, suffer worse effects from scatter than planar images. Scatter can create substantial artifacts in the reconstruction slices. As the tomosynthesis dose is already elevated slightly over planar radiography, an additional dose penalty for grid use is undesirable.

4.1.3 Scatter in thoracic imaging

Scatter is a well-known problem in thoracic imaging, where scatter-to-primary ratios can exceed 20. [76] [77] Scatter from dense tissue and bone obscures the details in soft tissue that are often of interest within the heart or lungs. Typical planar imaging systems and current commercial DCT scanners utilize an anti-scatter grid placed on the detector to reject the scattered photons after transmission through the object. Though effective, anti-scatter grids block primary photons and require increased entrance dose, on the order of 50% or more, to achieve adequate SNR. Due to the dose penalty, it is desirable to remove the scatter in tomosynthesis in some other manner.

4.2 Scatter mitigation techniques

4.2.1 Scatter estimation

4.2.1.1 Monte Carlo simulation

An alternative to scatter rejection is to computationally approximate the scatter and subtract it from the projection images. Monte Carlo (MC) simulations have been used to approximate scatter in breast tomosynthesis based on the patient image [78], but this method requires substantial computing time and is impractical for a clinical environment.

4.2.1.2 Scatter libraries

A more likely implementation of this method involves using pre-computed models, or scatter map library, chosen based on the similarity to the patient image. [79] This approach is initially computation intensive and is not patient-specific.

4.2.2 Scatter rejection and reduction

Physical mechanisms have been devised to reject scatter, such as scanning slot systems [69] [70] [77] [71] and anti-scatter grids [71].

4.2.2.1 Slot-scan imaging

Scanning slot systems utilize a fan beam and linear detector to scan the breast. This method is very effective at rejecting scatter, however it can require much longer scan times, ranging from 3-15 seconds per projection [74].

4.2.2.2 Anti-scatter grids

The current standard technique for mitigating the scatter is to use an anti-scatter grid. The grid reduces scatter, but also impedes primary photon transmission, requiring a larger patient dose to maintain SNR. Despite the dose penalty, linear and cellular grids are commonly used in commercial planar imaging systems. In chest imaging, a grid can reduce the scatter fraction from 70% to 20% in the lung and from 95% to 65% in the mediastinum [77]. Grid use is optional for mammography, employed as needed for dense or large breasts, and can reduce the scatter fraction to approximately 20% [75]. Three-dimensional modalities, such as CT and tomosynthesis, suffer worse effects from scatter than planar images. Scatter can create substantial artifacts in the reconstruction slices. As the tomosynthesis dose is already elevated slightly over planar radiography, an additional dose penalty for grid use is undesirable. Despite this dose penalty, linear grids have been adopted in chest tomosynthesis systems wherein the source is translated parallel to the detector, as in the VolumeRAD system (General Electric, Fairfield, CT). In standard breast tomosynthesis, the source rotates relative to the planar detector, thus the source rotation path and the linear grid lines are not coplanar. This makes the stationary linear grid with fixed focal length unusable on rotating gantry DBT.

4.2.3 Scatter subtraction

4.2.3.1 Beam stop scatter measurement

Scatter is generally of low spatial variance in comparison with anatomical structures [80] and a scatter map can be obtained by measuring the scatter signal from a small set of points in image space.

Direct scatter measurement requires use of a beam stop technique, wherein an object containing highly attenuating samples is placed between the source and patient. Scatter is sampled behind the objects [81] [82] and interpolated to a complete scatter map. The beam stop method is accurate for measuring scatter, but has drawbacks. If performed simultaneously with the patient scan, missing data must be interpolated. If performed as a second scan, it would incorporate nearly twice the dose, which is undesirable for clinical implementation.

4.2.3.2 Beam pass primary measurement

The inverse of a beam stop method, referred to as a beam pass method, exposes only small regions of tissue to sample the primary signal with little to no scatter. The primary signal samples are subtracted from the full-field image to generate sparse scatter samples, which are then interpolated to a complete scatter map. This method has no missing image information, but one drawback is that it requires an additional image. With a modern fast frame rate detector, this is less of an issue. The beam pass method has been utilized in breast CT [83] [84] [85]. In these studies, the placement of the beam pass array is close to the source, as is required by CT geometry. This results in relatively low sampling density and greater penumbral effects due to the large magnification factor. Both make the estimated scatter map less accurate.

CHAPTER 5: PRIMARY SAMPLING SCATTER CORRECTION

Our team has developed a beam pass technique called primary sampling scatter correction (PSSC) for projection radiography and tomosynthesis, using the same principle of primary beam sampling and scatter interpolation demonstrated in breast CT. [83] [84] [85] In comparison to CT, radiography and tomosynthesis provide a more favorable geometry with relatively large source-to-object distances, and typically fixed object-detector positioning, allowing placement of the aperture array, or primary sampling device (PSD), close to the object (Figure 5-1a). This reduces penumbral effects due to the side wall of holes, allowing smaller holes and denser sampling points, thus more accurate estimation of the scatter map and reduction of the dose used in the primary sampling step. The PSSC technique can accurately estimate the patient-specific scatter map, with minimal additional dose. [86]

The PSSC technique has been demonstrated for mammography, digital breast tomosynthesis [86], chest radiography, digital chest tomosynthesis [87], and is being investigated for potential use in cranial CT imaging. The primary sampling scatter correction (PSSC) technique has been demonstrated which can accurately estimate the patient-specific scatter map, with minimal additional dose. [86] [87] [88] [89] This chapter contains the first comprehensive review of the PSSC technique and its efficacy in multiple modalities of medical imaging.

5.1 Primary sampling theory

As briefly outlined in chapter one, scatter can be measured and subtracted via utilization of beam pass techniques. [85] Two images are acquired, one full-field object image, and a second image exposed through an array of small apertures, or primary sampling device (PSD). By exposing only small regions of material, little scatter is generated, and samples of the primary transmission signal are attained. These

primary samples (p) are sparsely situated so that scatter from adjacent holes is not measured. Though the sparse primary sampling would be completely inadequate for interpolation to an object image, these values can be used to calculate the scatter samples (s) when combined with corresponding samples of the full-field object image (t) via s=t-p. As scatter presents as a low-frequency signal, sparse samples (s) can be used to interpolate an accurate scatter map, S. This scatter map is subtracted from the original full-field image (T), to generate a scatter-free projection, T-S=P. Although somewhat over-simplified, figure 5-1 is a graphical representation of the PSSC scatter correction process in which the full-field total image (T) can be recomputed to a scatter-free projection image (P).

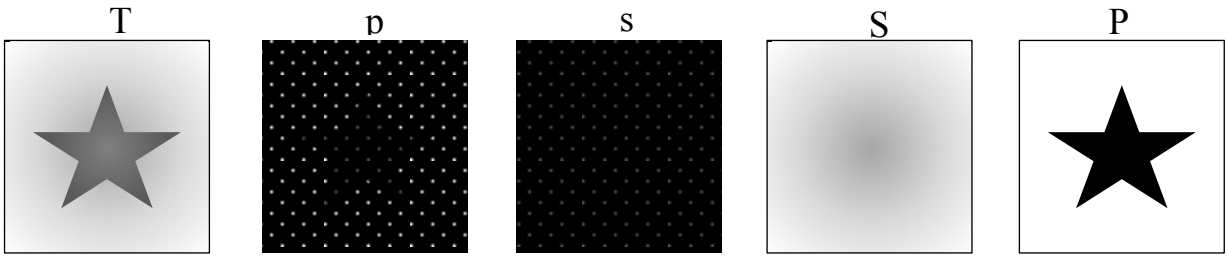

Figure 5-1: Graphical representation of total image (T), primary samples (p), scatter samples (s), interpolated scatter map (S), and scatter-free projection (P).

5.2 Patient-specific scatter correction for breast imaging

In the case of breast imaging, the compression paddle serves as an ideal host for the beam pass array. Figure 5-2a is a diagram showing system configuration for PSSC imaging on a mammography or breast tomosynthesis system. This section details the experiments performed to design a system-appropriate PSD and implementation in both mammography and digital breast tomosynthesis. Figure 5-2b is a photo of the PSD on our s-DBT compression paddle.

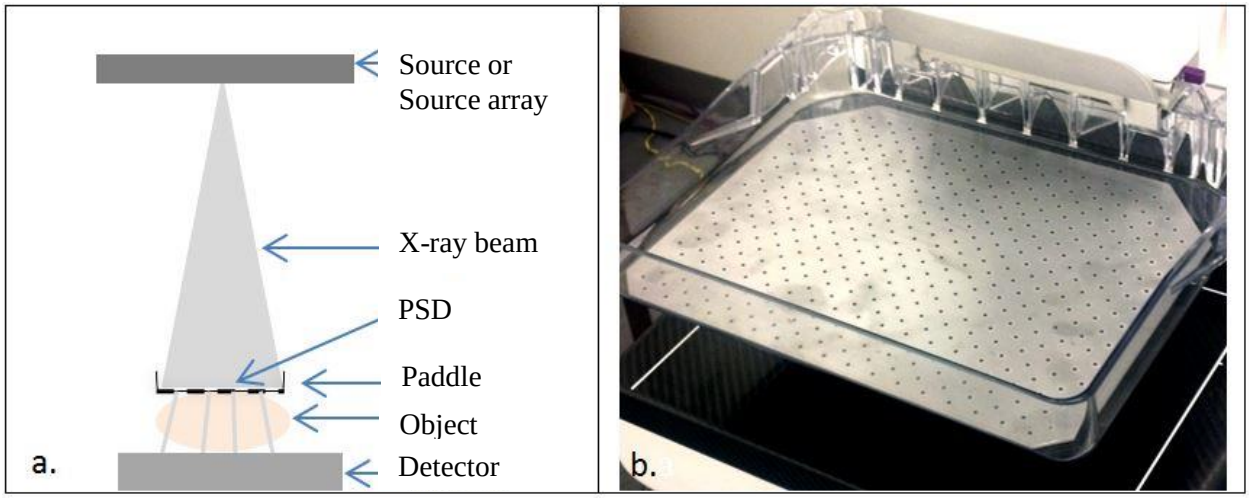

Figure 5-2: a) Diagram of system configuration for PSSC breast imaging; b) Photo of the PSD on the compression paddle of the s-DBT system.

5.2.1 Full-field digital mammography (FFDM)

Mammographic images were acquired with a conventional anti-scatter grid for quantitative evaluation of the PSD scatter correction technique. This comparison was performed on a full field digital mammography (FFDM) system (Senographe Essential, GE, figure 5-3). The FFDM has a removable, reciprocating focused grid assembly.

Figure 5-3: Photo of the GE Senographe full-field digital mammography system

5.2.2 Stationary digital breast tomosynthesis system

The PSSC technique was implemented on our s-DBT unit (figure 2-4). The source array is a single line of 31 focal spots (0.6 um x 0.6 um), created using carbon nanotube field emitters, with a W/Al anode/filter combination. A subset of 15 focal spots was used for the imaging in this project. The cathodes are individually switchable and focused on the detector, allowing up to 30 degrees of angular coverage. The detector on the Hologic system has a pixel size of 70um x 70um, with an effective size of 140um x 140um in 2x2 binning mode.

5.2.3 Primary sampling device (PSD)

The PSD is a detector-sized collimator designed to lie flat on the compression paddle. For accurate primary sampling, the plate must be thick enough to attenuate the primary beam, yet as thin as possible to minimize edge effects when imaging at an oblique angle. This section details the measurements made to determine physical parameters for PSD construction and validation of the completed device.

5.2.3.1 Attenuation measurement

Three partially overlapping plates of 1mm stainless steel (SS) were imaged at 35kV to determine the thickness at which the attenuation reached >99%. Figure 5-4a is a false-color projection image of the overlapping plates indicating the region of interest (ROI) plotted in figure 5-4b. The transition from 1mm to 2mm of thickness yields a gray level in the range of the typical dark field image, approximately 50-60 counts, therefore 2mm was deemed adequate for this study.

5.2.3.2 Aperture size and pitch

Aperture geometry was determined via empirical measurements in order to balance between the competing factors of sampling frequency and patient dose. Apertures of 2, 3, and 4mm diameter were drilled into a 1mm plate of stainless steel and imaged in conjunction with attenuation measurements (figure 5-4a). An additional plate incorporating a proposed design was also imaged to validate aperture size and spacing. Figure 5-4c is an ROI from 5-4a, rotated and zoomed to highlight the proposed geometry. The plot profile of this ROI is shown in figure 5-4d, indicating that the samples are uniform. The diameter of the apertures must be large enough to ensure adequate sampling of the primary information, yet kept as small and sparse as possible to maintain a low dose to the patient and minimal scatter signal generated for primary sampling. A pattern of 2mm holes with a 10.6mm pitch was fabricated in 2mm stainless steel.

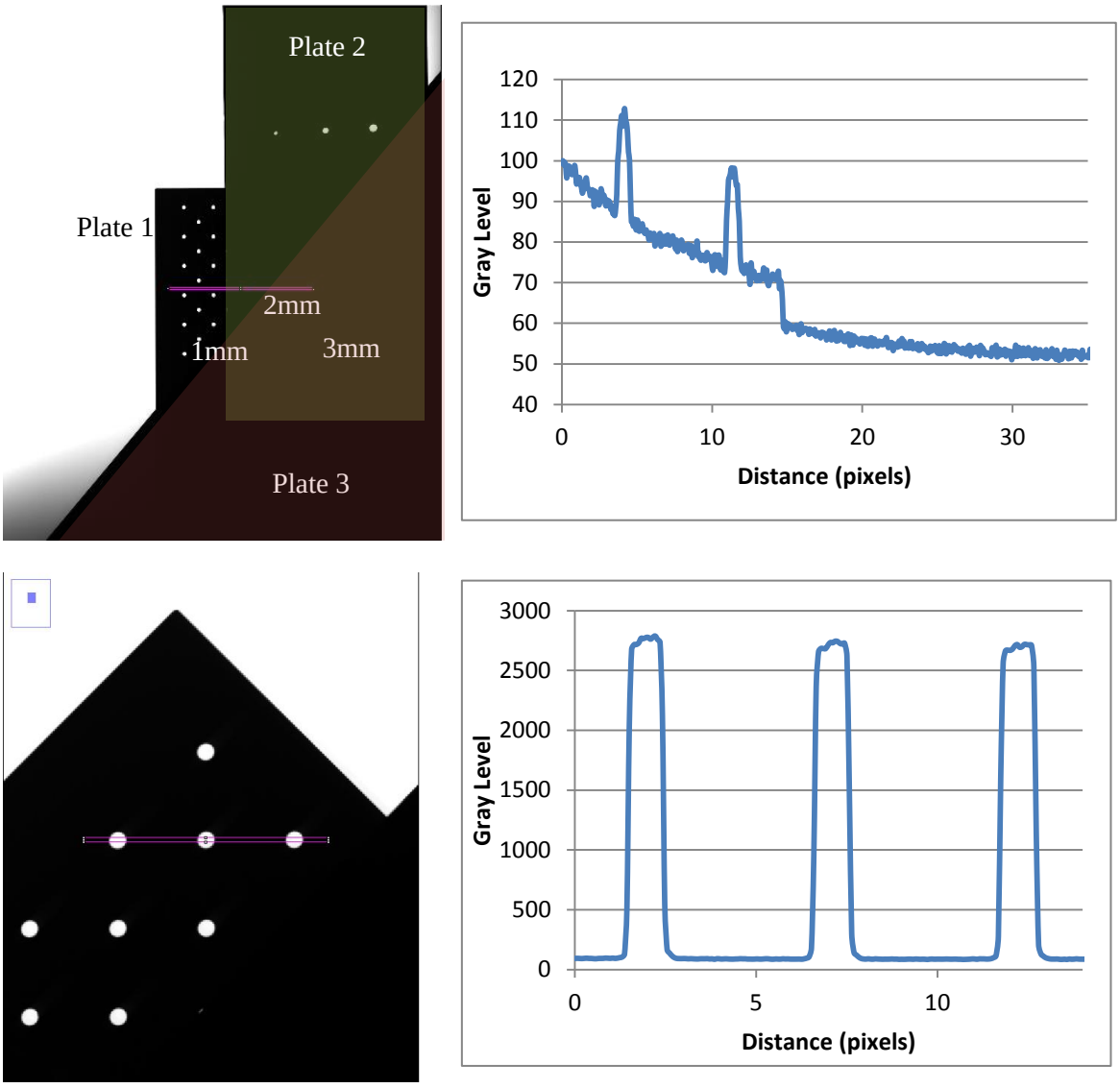

Figure 5-4: a) Projection image of three overlapping plates for transmission measurement; b) Plot profile of ROI in (a) showing adequate attenuation at 2mm thickness; c) Zoomed ROI of (a) containing the proposed design; d) Plot profile of (c) showing adequate sampling geometry.

5.2.3.3 Penumbral effects

The size of the apertures used for primary sampling must allow full transmission of the primary signal over an area for averaging. Undersized apertures would result in rounded profiles due to the cone geometry of the source and the parallel side-walls of the apertures. Yet smaller apertures would be affected by the finite size of the focal spot, but the scale used here is a magnitude higher and does not warrant concern. An adequate sample diameter should produce a nearly square profile in a homogenous

field. The PSD was imaged using an anthropomorphic breast biopsy phantom (CIRS Model 013) to evaluate the profile. Figure 5-5a is a projection image in which three ROI are indicated. Figure 5-5b is the plot profile of ROI #1, through the bright field portion of the image, demonstrating plateaus at the apex of each sample. Figure 5-5c is a surface plot of one aperture, ROI #2, also displaying a flat sampling region. Figure 5-5d is the plot profile of ROI #3, with samples of much lower intensity still displaying a relatively square profile with no visible scatter tails. This verified that the sampling pitch was large enough to avoid crosstalk of scatter tails produced in regions of thick scattering material.

5.2.3.4 Oblique transmission

The s-DBT allows 28^{o} of angular coverage, with 14^{o} incident angle from each end of the source array. This angle must be considered in the use of parallel-walled apertures. The PSD thickness of 2mm was expected to have some impact on sample shape, and perhaps quality, so was evaluated at various incident angles. Figure 5-5e shows a zoomed view of an aperture in the central source projection, near the periphery of the plate, with the circular primary sample indicated. Some distortion is observed, but an ROI of nine-pixel sampling diameter is shown to fall well within the boundary. Figure 5-5f shows a similar image using a 14^{o} projection image. This aperture is also located on the periphery of the image, to provide a worst-case scenario for sample distortion. The apparent compression of the sample in one direction results in a width of similar size to our sampling region. As shown, this could result in the sampling of a few penumbral pixels, but still maintains a large area of uniform illumination. Sampling penumbral pixels is an undersampling of primary signal and would generate a slight overestimate of scatter.

Previous beam pass work for breast CT [83] [84] [85] required application of a correction factor to the measured primary values due to attenuation of signal through the holes. To ensure accurate measurement of the primary signal in this study, the PSD projection was evaluated in comparison to the corresponding blank projection at the same acquisition angle. The PSD was imaged without the paddle to

check transmission rate through the sampling apertures. Figure 5-5g is a plot profile through four apertures in the periphery of the 14^{o} image, as well as a full-field image. It can be seen that the primary samples do not measure the entire primary signal, with a difference on the order of 5%. This problem can be mitigated by adjustment of the sample diameter in the PSSC algorithm, or correction via a scaling factor map, though it is not critical for breast applications. This occurs only in the distal corners of the most oblique images, where breast tissue is rarely present. A PSD design for larger paddle and detector geometries would require reconsideration of this factor.

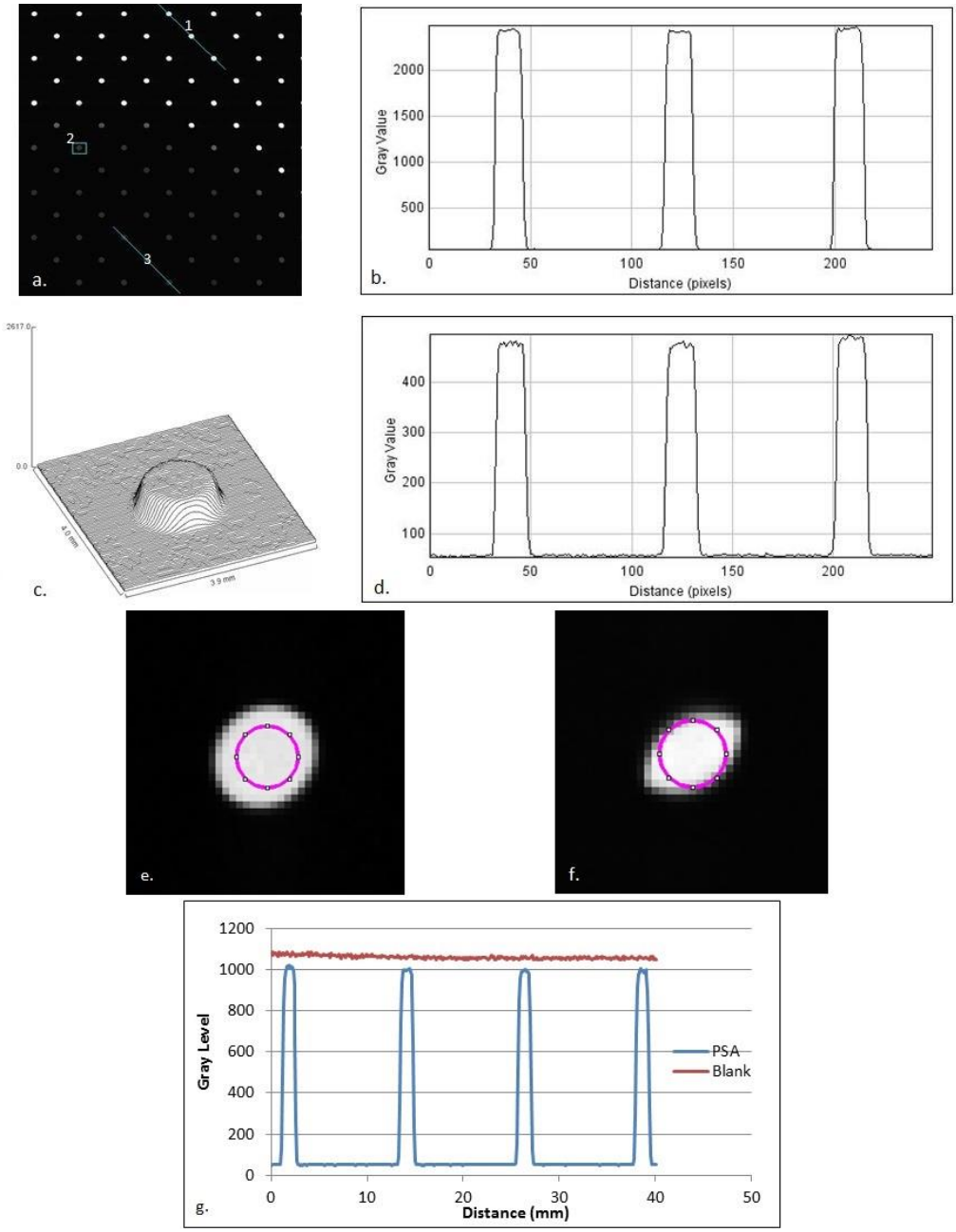

Figure 5-5: a) PSA image indicating regions of interest in b)-d); b) line plot through bright field area indicated in ROI 1; c) surface plot of ROI 2; d) line plot through phantom area indicated in ROI 3. Results indicate that the 2mm thick plate is sufficient to attenuate the x-ray beam, the 2mm hole size is sufficent to to provid accurate primary sample, and the hole distance is sufficent to avoid crosstalk of scatter signals. Figures 8e) and f) show typical primary sampling (e), and hole distortion (f) at the maximum incident angle. Figure 8g shows the transmission of the primary signal through the PSD in comparison to the blank image.…

5.2.4 Image processing chain

For the purpose of standard image processing, multiple blank and dark images were acquired. Raw images were corrected according to Corrected *image= (Raw image – Dark image) / (Blank image – Dark image)*, prior to scatter correction.

5.2.4.1 Scatter interpolation

A scatter correction algorithm was applied to estimate the scatter maps. Though fundamentally similar to previous beam pass corrections [83] [84] [85], this algorithm performs three separate scatter interpolations. Preliminary studies of the method used a single interpolation over the entire image which demonstrated visible artifacts in transitional regions. [86] Refinement of the algorithm included segmentation of the full field image to create three ROI, the object, background, and skin line. Scatter maps for each region are calculated independently and merged. Figures 5-6 to 5-9 illustrate the process for each step.

As shown in Figure 5-6, the full field image was first segmented to find the skin line and establish the boundaries for skin line interpolation, or skin line mask. The segmentation was performed within the algorithm, binarizing the image based on a threshold computed via the MATLAB function *graythresh*. The PSD image was then segmented to define the primary sample locations. This image was also binarized in the algorithm using a manually-adjustable threshold. The binary image was automatically checked for over- or under-sized sample regions and the user prompted to adjust the threshold, if necessary. Object and background masks were generated using fixed samples of nine pixel diameter to eliminate sampling in penumbral regions.

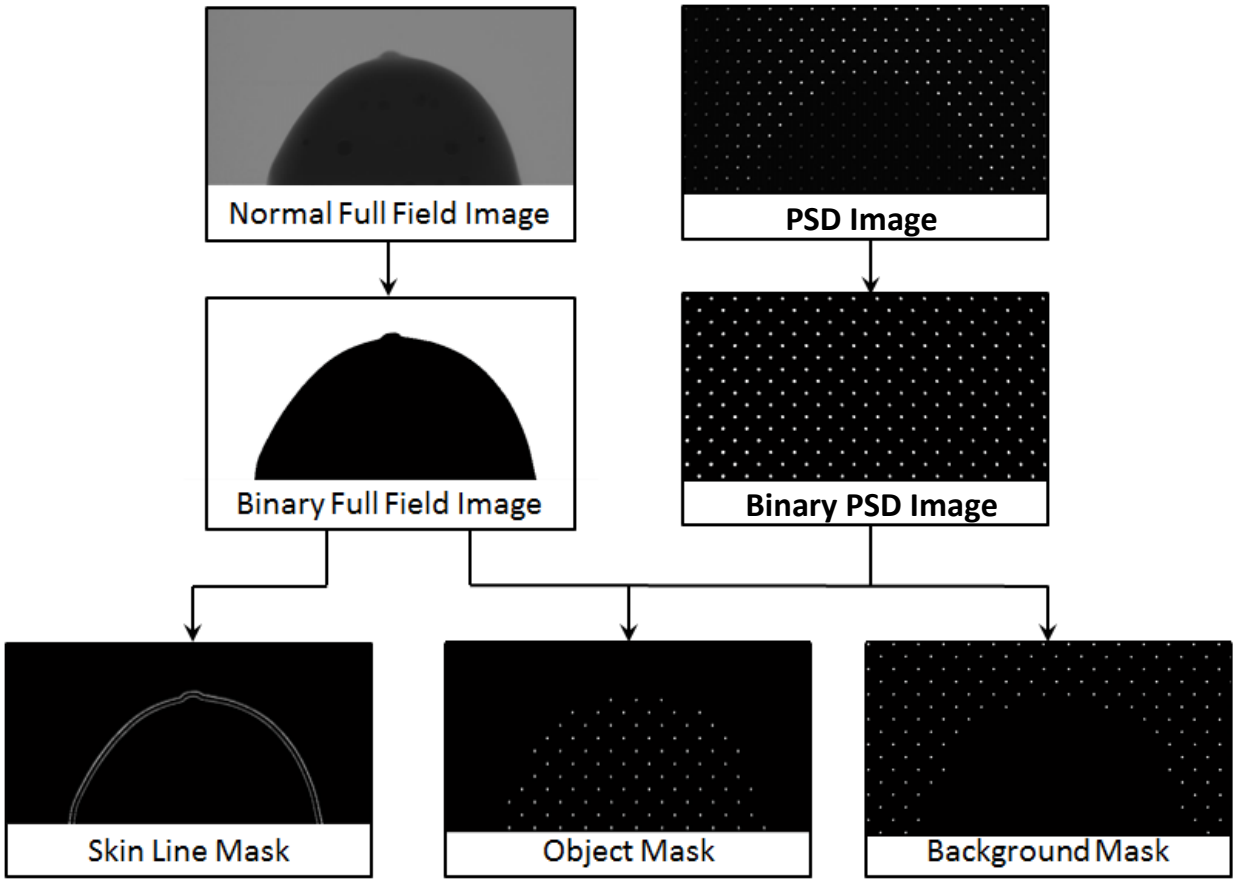

Figure 5-6: Flow chart showing steps for segmenting the images into the three ROI: skin, object, and background.

Figure 5-7 depicts the use of these masks to sample the PSD image and normal projection image to generate a map of the scatter samples. Discrete values of the primary signal, *P*, were computed by averaging the signal intensity over circular regions (d = 9 pixels) at the center of each PSD hole. The corresponding pixels were averaged within the full field projection (without PSD) to compute the total signal (scatter + primary), *T*. Values for the scatter signal in these hole locations were computed using $S = T - P$, producing scatter sampling maps for the object and background regions.

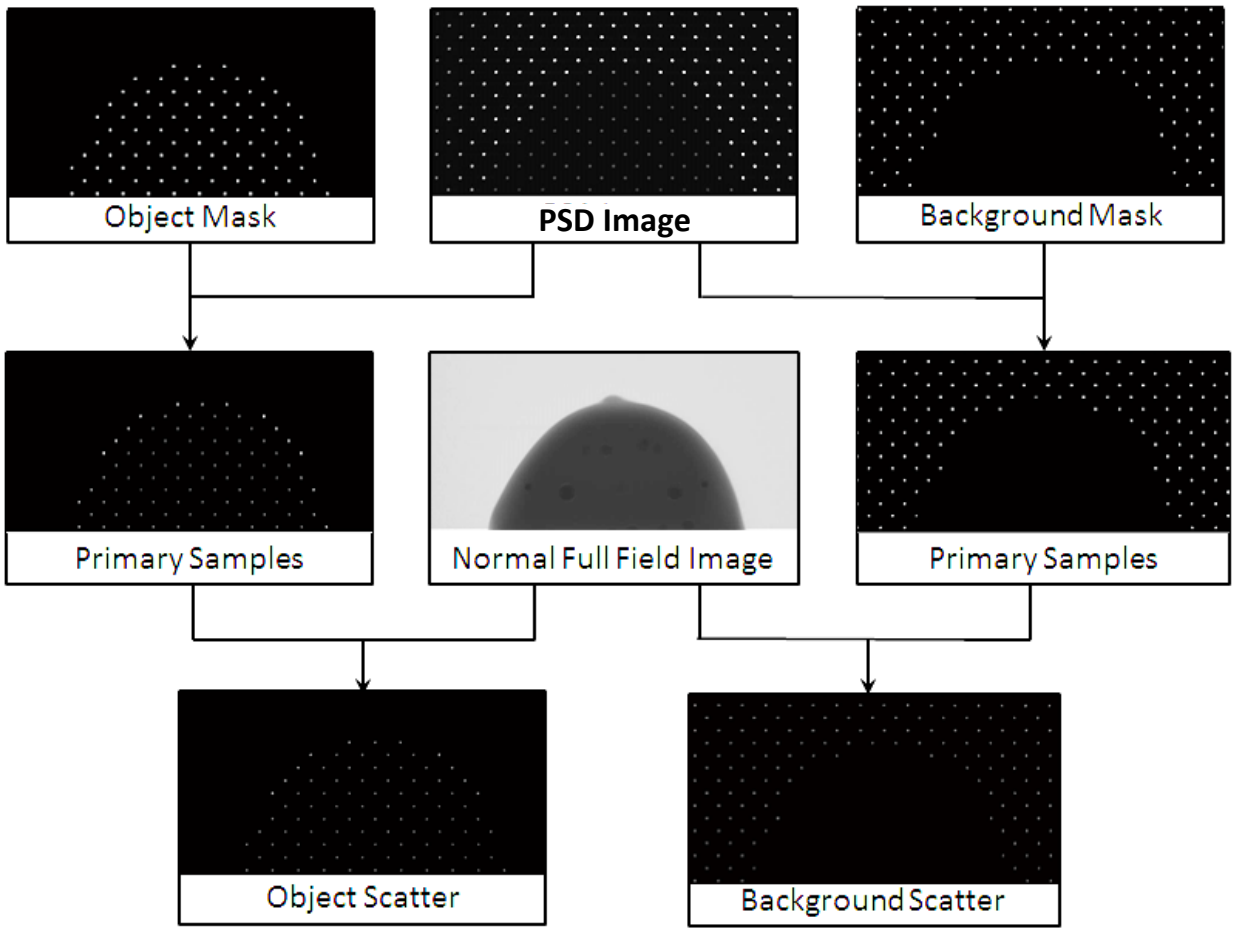

Figure 5-7: Flow chart showing steps for obtaining scatter samples from PSD and full field image using masks generated via the process in figure 4.

These scatter sampling maps were then used for two separate biharmonic spline interpolations, in the object and background regions, as shown in Figure 5-8. These interpolations were sampled using the skin line mask to generate a data set of two concentric silhouettes, the inner sampled from the object interpolation and the outer sampled from the background interpolation. These two lines were then interpolated to generate a smooth transition from the object to background regions. All three interpolated images were cropped to their region of interest and combined to generate the first estimate of scatter in all pixels, S_{int}. The interpolated scatter map could have been used at this point to increase the contrast by

subtracting the low-frequency scatter profile from the full field image. This method is referred to as the scatter interpolation (SI) scatter correction.

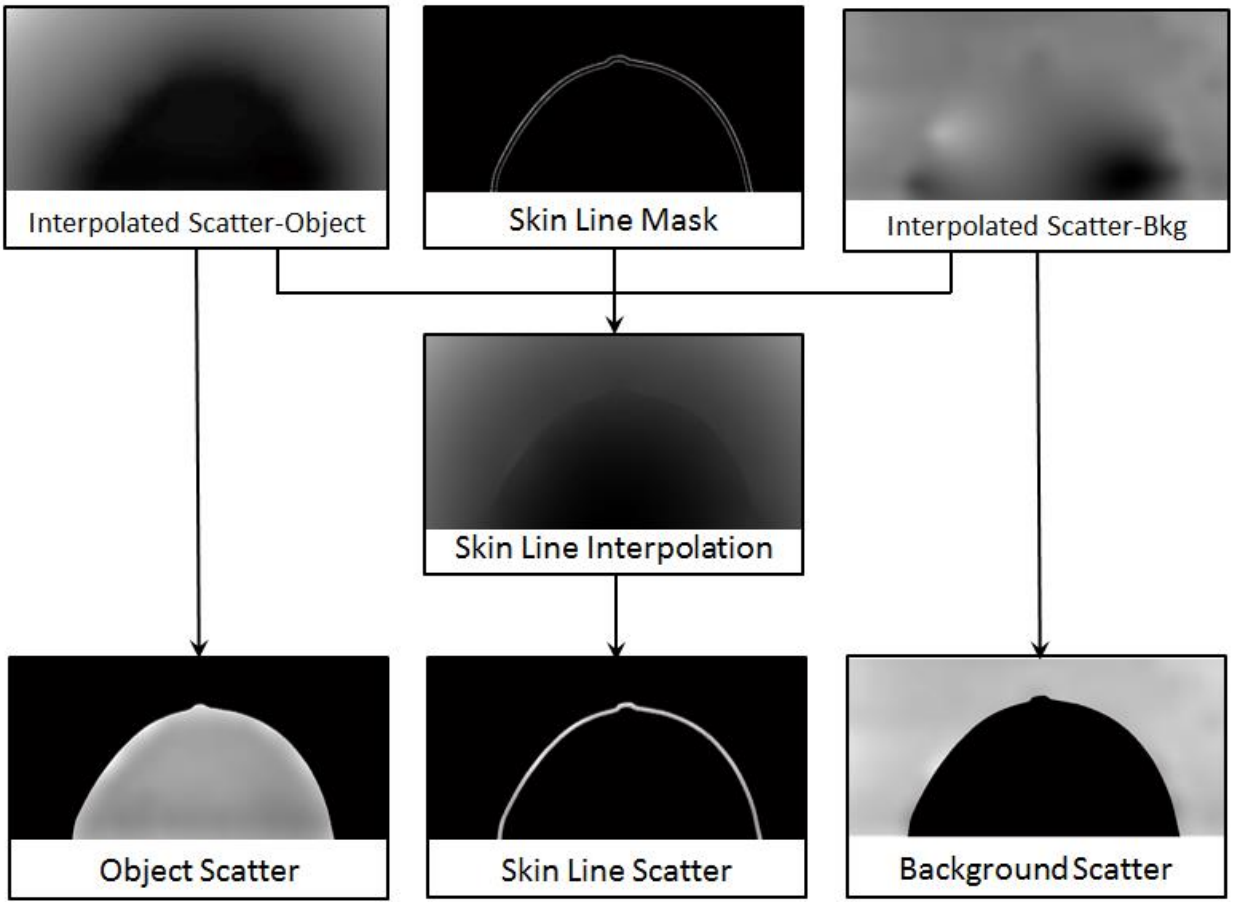

Figure 5-8: Skin line interpolation is a result of sampling from the object and background interpolations. Object, skin line, and background scatter are cropped into their respective ROI and combined into one scatter map. The scatter map is combined with the full field image to generate the SPR, which is then filtered. Note that the window/level values of these images are non-uniform. They have been adjusted for feature visibility.

5.2.4.2 Filtered scatter-to-primary ratio (f-SPR)

Since S_{int} is a smooth varying function, subtraction results in a loss of signal, adversely affecting the signal-difference-to-noise ratio (SdNR) as the noise in the images is not reduced. It is desirable to increase both the contrast and SdNR, so the scatter correction must include a high-frequency scatter component. The full field image contains noise, including noise from scatter, to which the amount of

local fluctuation may correlate. To capture this we apply additional processing, also shown in Figure 5-9. The scatter-to-primary ratio (SPR) is calculated at each pixel location using $SPR = S_{int}/(T - S_{int})$. The SPR map was then filtered via convolution with a low-pass Gaussian to generate the filtered SPR, SPR_f. The Gaussian convolution kernel was a rotationally symmetric matrix of 9x9 pixel size with a standard deviation of σ=2 pixels. The filtration produces a smoother SPR_f image, which when mathematically recombined with *T*, produces a fluctuating scatter map. The final processing steps are shown in Figure 7, wherein the final estimate of the scatter, S_{fspr}, is re-computed from the SPR_f using $S_{fspr} = T \cdot SPR_f/(1 + SPR_f)$. The final scatter map, S_{fspr}, includes a smooth varying scatter component and part of local fluctuations associated with the full field image, *T*. When S_{fspr} is subtracted from the full image, T, there is a corresponding reduction of high frequency local fluctuation, in addition to the elimination of the low frequency object-specific scatter map. Compared with using the interpolated scatter, S_{int}, this method improves both the contrast and SdNR significantly. This technique is referred to as the filtered scatter-to-primary ratio (f-SPR) scatter correction.

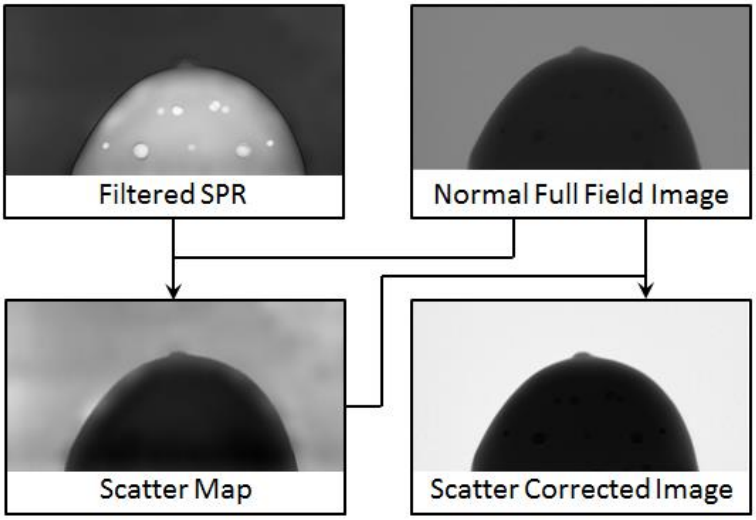

Figure 5-9: The filtered SPR is recombined with the full field image to generate the final scatter map, used to generate the scatter corrected final image.

5.2.5 Phantom imaging

5.2.5.1 FFDM imaging

Mammographic images were acquired with a conventional anti-scatter grid for quantitative evaluation of the PSD scatter correction technique. This comparison was performed on the FFDM system. The Senographe has a removable, reciprocating focused grid assembly. Phantoms were imaged with one edge placed at the chest wall location on the detector to simulate patient positioning.

Images of an American College of Radiology (ACR) accreditation phantom, CIRS 015 (Figure 5-10a), were acquired with the grid installed using automatic exposure control (AEC) calculated technique of 29kV and 46mAs with Rh/Rh anode/filter combination. The grid assembly was removed and phantom imaged with a similar manual technique of 29kV, 45mAs, Rh/Rh, as the manual settings do not allow for ±1mAs adjustment. The same phantom was then imaged with the PSD plate using the same exposure level.

A second breast imaging phantom, BR3D, CIRS 020 (Figure 5-10b), was also imaged to evaluate the technique on a thicker object This phantom is comprised of six slabs, each 1cm thick, with one slab containing objects of interest. The remaining slabs are a swirled mixture of 50%/50% adipose/glandular tissue mimic. The object slab was placed beneath one slab of tissue mimic, and on top of the other four, for a total of 6cm thickness, to generate a relatively large amount of scattering volume. The phantom was imaged in the same manner as the ACR, but with AEC technique of 30kV and 76mAs determined using the grid.

5.2.5.2 s-DBT imaging

The stationary digital breast tomosynthesis system (s-DBT) system developed at UNC was used for this study with scans performed in binning mode, utilizing fifteen beams, covering 28 degrees.

A CIRS 013 stereotactic needle biopsy phantom (Figure 5-10c) was imaged for initial evaluation of the PSD method, utilizing the same PSD used in the FFDM grid study. The phantom is comprised of a gel material with embedded masses and microcalcification clusters at varying depths. Dark and blank images were acquired prior to phantom imaging. The phantom was placed on the midline of the detector, with the flat side situated at the patient edge of the detector to mimic clinical patient positioning. The phantom was compressed to 4.1cm. Tomosynthesis scans were performed at 100mAs [29] [25], with and without the PSD. Each configuration was acquired three times for statistical analysis, with a protocol of 15 views over 28 degrees.

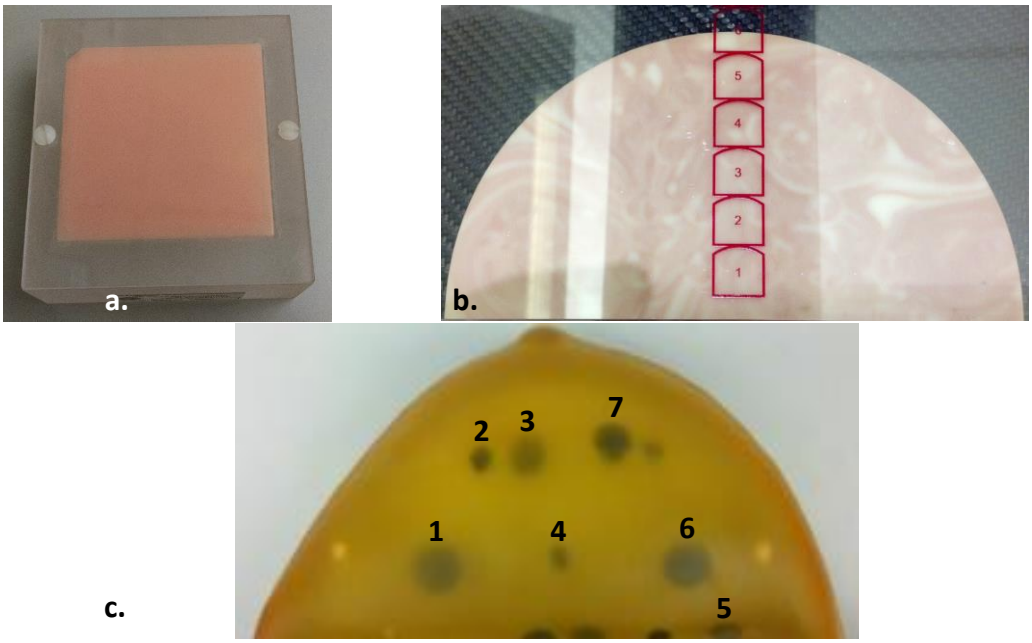

Figure 5-10: Photos of mammography study phantoms a) CIRS 015 (ACR) and b) CIRS 020 (BR3D) shown under the compression paddle. Photo of CIRS 013 stereotactic needle biopsy phantom (c), quantitative analysis was performed on the numbered masses.

5.2.6 Contrast and SdNR analysis

Object contrast is imperative for lesion detectability. Quantitative evaluation of this method was performed in ImageJ by calculating the contrast (C) of seven masses in the CIRS 013 phantom using the object intensity measured with respect to the background material, μ_{obj}, and μ_{bkg}, respectively (Equation 5-

2). Not all masses in the phantom were suitable for evaluation. The ROIs were selected within the object by sampling a circular region at the center, utilizing the central 25% of the object area. The background value was measured in an annular region situated at approximately 1.5x the object radius to avoid any edge effects from the mass. The masses chosen for analysis are shown in Figure 5-10c. Masses containing simulated microcalcifications and/or central fissures were excluded from analysis.

$$\text{Equation 5-1: } C = \frac{|\bar{\mu}_{obj} - \bar{\mu}_{bkg}|}{\bar{\mu}_{bkg}}$$

Contrast alone does not define good image quality, as it can be manipulated in digital imaging[4]. It is also a relative metric in which noise is overlooked. In addition to evaluating the contrast, the signal difference to noise ratio, SdNR, was calculated as a firm descriptor of the image quality, utilizing Equation 3. The SdNR was calculated using the same ROI with the additional measurement of the standard deviation of each sample area, μ_{obj}, and μ_{bkg}.

$$\text{Equation 5-2: } SdNR = \frac{|\bar{\mu}_{obj} - \bar{\mu}_{bkg}|}{(\sigma_{obj} + \sigma_{bkg})/2}$$

Quantitative comparison of the FFDM images of the ACR phantom was made using the uncorrected full field image, an anti-scatter grid image, and a PSSC-corrected full field image. The SdNR values of the three largest masses of the phantom were measured.

5.2.7 Imaging results

5.2.7.1 Comparison of PSSC technique with anti-scatter grid in FFDM

5.2.7.1.1 ACR phantom

Results of the comparison of the PSSC technique with anti-scatter grid using the ACR phantom are shown in figures 5-11 and 5-12. Figure 5-11 is the full field uncorrected image and b) is the calculated scatter map, windowed to exaggerate non-uniformities. Under- and overestimates of scatter

occur in regions of abrupt attenuation transition, as demonstrated near the rectangular ID tag (arrow, Fig. 5-11a). Figures 5-11c-e are the uncorrected image, anti-scatter grid image, and the PSSC corrected image. Display window level and width are set to the background mean, and 5% of mean, respectively. The uncorrected image demonstrates cupping due to scatter, which presents as a background gradient. The cupping is gone in the grid image and contrast is enhanced; however, the loss of primary photons to the grid reduces the SNR and adds grainy texture to the features and background. The cupping artifact was also removed in the PSSC corrected image, but without introduction of additional noise. Some minor artifacts remain, particularly at the perimeter, from the scatter map inconsistencies. The PSSC-corrected image preserves the high photon count of the uncorrected image while flattening the background. Enlarged views of the largest mass and fiber are shown in figures 5-11f-k, wherein the background gradient of the uncorrected images can be easily visualized as well as the grainy texture of the grid images.

Quantitative analysis was performed on the three largest masses, as labeled in Figure 5-11c. The overall result of the PSD scatter correction is an improvement in SdNR for the masses, as shown in Figure 5-12. The improvement in SdNR varied from 60-79% over the uncorrected image, with an average of 68%, and 32-42% over the grid image, with an average of 37%.

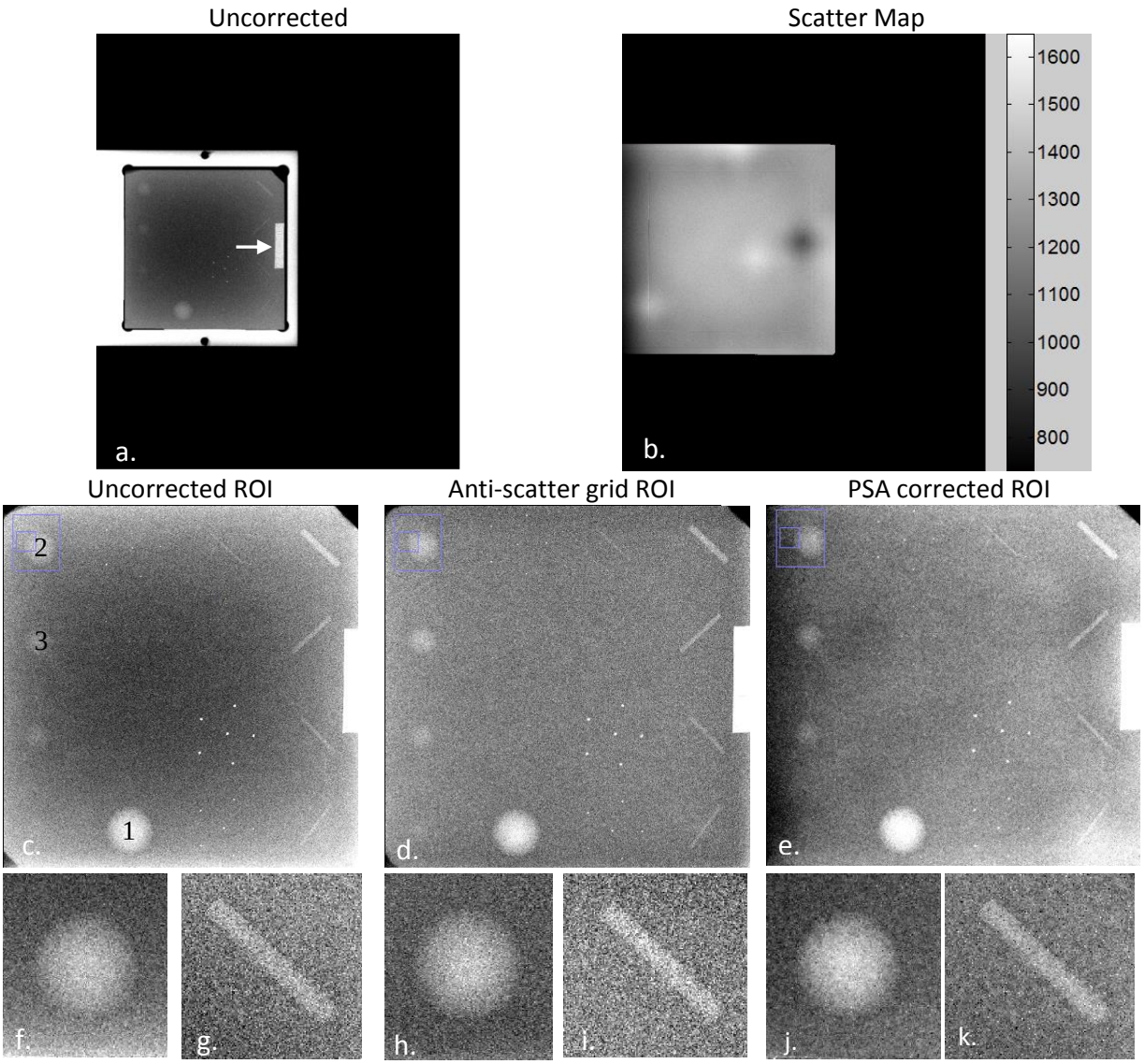

Figure 5-11: ACR images; (Top) a) Full field image without scatter correction, and b) calculated scatter map. (Center) Enlarged ROI c) without scatter correction, d) with anti-scatter grid, and e) with PSD scatter correction. (Bottom) Magnified views of the largest mass and fiber, f) and g) without scatter correction h) and i) with the anti-scatter grid; and j) and k) with PSSC correction. All images were taken at the same exposure. The scatter map (b) displays some non-uniformities due to under sampling at the perimeter and areas of abrupt transition, resulting in non-uniformity of the PSD image (e).

Figure 5-12: SdNR for three masses in ACR phantom. The PSA-corrected image had higher SdNR than both the uncorrected and grid images acquired at the same exposure.

5.2.7.1.2 BR3D phantom

BR3D phantom mammographic images are shown in figure 5-13 for qualitative comparison. This dataset includes the filtered-SPR PSSC scatter correction images as well as a set of images corrected with only the interpolated PSSC scatter correction. Figure 5-13a is the full field image without scatter correction. The fibers and masses of the BR3D object slab are not visible in any of the images, so three clusters of microcalcifications, at 400, 290, and 230um diameter, have been chosen for comparison, labeled 1, 2, and 3. Figure 5-13b is the PSD corrected image. Figures 5-13c-f, from left to right, are the uncorrected, anti-scatter grid, interpolated-scatter corrected, and PSSC (f-SPR scatter corrected) images of cluster one. Figures 5-13g-j and k-n are corresponding images of clusters two and three, respectively. The anti-scatter grid image is shown with GE post-processing for presentation, automatically performed by the system to optimize viewing for the radiologist. Though some mammography systems have an

embedded grid assembly, the GE Senographe system does not. The grid is installed manually via an external housing that slips onto the detector. Note that use of the grid requires removal and repositioning of the object and alters the object-detector distance, therefore system magnification. Both of these factors attribute to apparent feature shifting in grid images compared to the other images. All images are leveled and windowed based on the mean gray level and standard deviation in the region of each cluster, respectively. The placement of the microcalcifications within the object, near the chest wall edge, is in an area with lower inherent scatter than the center. This may be the reason for the subtle difference between the uncorrected and anti-scatter images. The images corrected with interpolated scatter show an increased contrast with increased noise. Compared to all the other images, the PSSC scatter corrected images (right) have a smoother appearance without a loss of feature contrast.

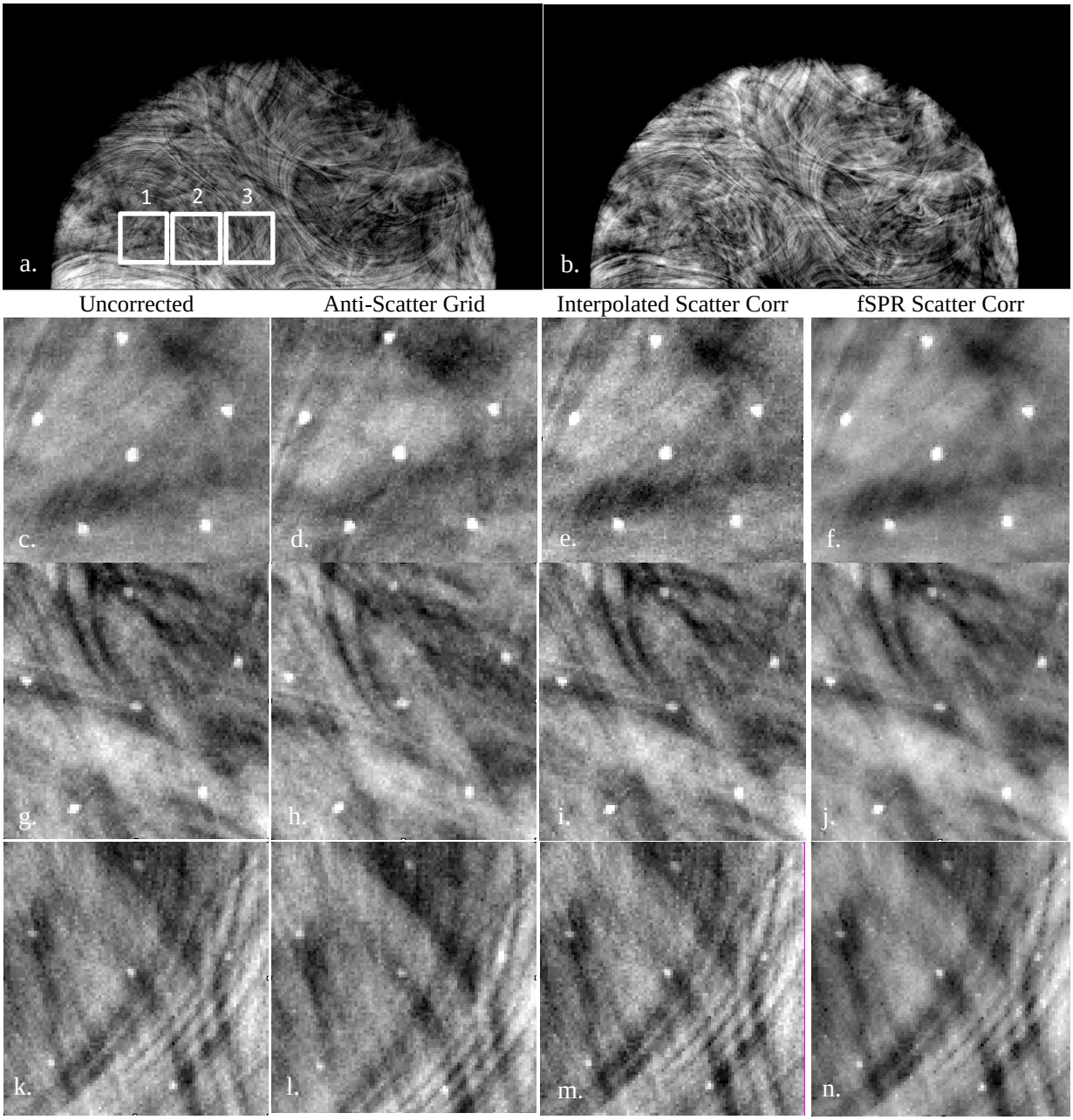

Figure 5-13: BR3D images acquired with the GE Senographe. Full field image with no correction (a) and PSD scatter correction (b). Microcalcification cluster ROIs are indicated. c-f) Images of cluster 1 (400um) from left to right, uncorrected, with anti-scatter grid, with interpolated scatter correction, and with fSPR scatter correction. g-j) Corresponding images of cluster 2 (290um). k-n) Images of cluster 3 (230um). Noticeable reduction of noise in PSD corrected images can be seen.

5.2.7.2 PSSC in s-DBT

5.2.7.2.1 Tomosynthesis projection images

The CIRS 013 phantom was imaged three times at 100mAs total exposure. The images were processed for beam and detector non-uniformities. The scatter correction procedure was performed and corrected projection images were obtained. Figure 5-14 depicts the images obtained in the correction process. The exposure for each projection was 6.7mAs. Figures 5-14a and b are the image without scatter correction, and with scatter correction for the central x-ray projection. The corrected image is displayed to match the window and level optimized for the uncorrected image. Figure 5-14c is the scatter map produced for this projection image. Figure 5-14d is a scatter map for the projection image taken from the 12 degree incident angle, for comparison. Figures 5-14e and f are enlarged images of mass 3 before and after scatter correction, also from the central x-ray projection image. The scatter corrected image contains less noise in the object and background regions and higher contrast. For fair qualitative comparison, images 5-14e and f have been adjusted to similar window width and level based on their respective mean background intensities. The level is equal to the mean background intensity of an annular sample and the window is set to 10% of that value.

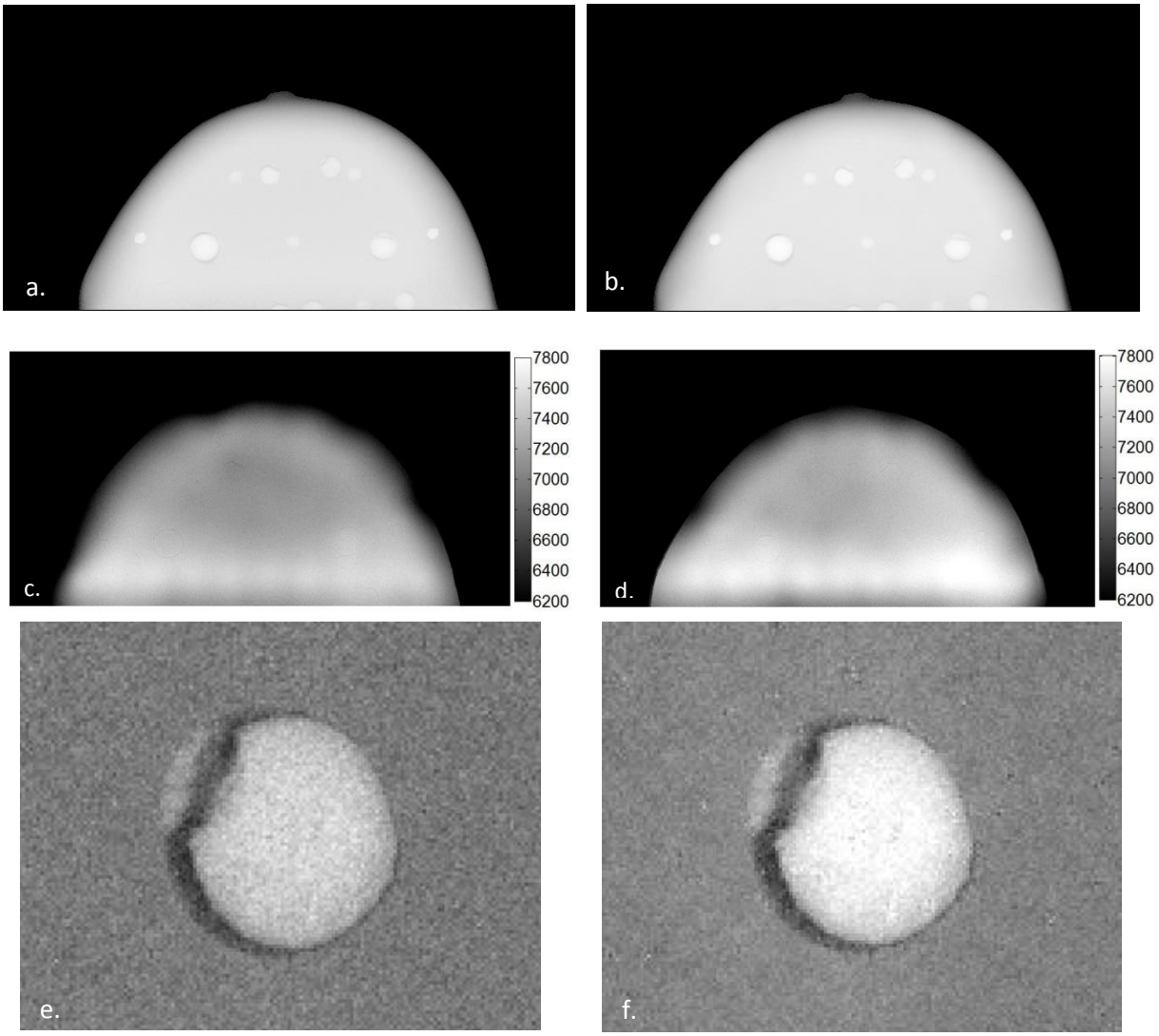

Figure 5-14: Inverted projection images, 100mAs scan; a) Uncorrected, b) Corrected, and c) Scatter map, from the central projection; d) Scatter map from 12 degree projection; e) Mass 3, uncorrected; f) Mass 3, corrected, from the central projection. Noise is visibly reduced in the corrected images.

Projection images of the CIRS 013 biopsy phantom were analyzed at multiple incident angles. Image quality improvement was similar for all angles. Contrast and SdNR in the corrected projections were increased by averages of 60 and 50%, respectively. Figures 5-15 and 5-16 depict the increase in contrast and SdNR observed for each mass. The error bars were calculated via standard deviation of measurements made on three separate datasets. Figure 5-17 details the level of enhancement observed via increase of the contrast and SdNR, calculated as Improvement Factor = Corrected Value/Uncorrected Value.

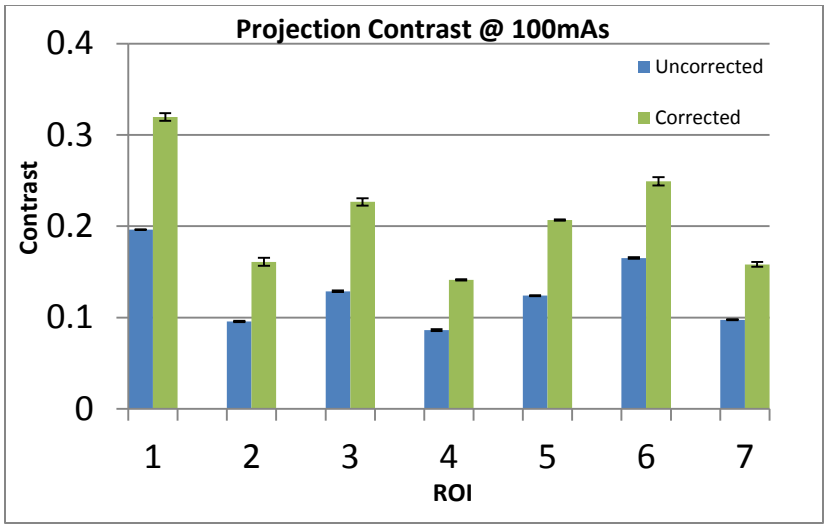

Figure 5-15: Contrast for different masses in the CIRS 013 phantom for the central projection at 6.7mAs exposure. Significant improvement in contrast is observed with PSD scatter correction, with average improvement in contrast of 60%.

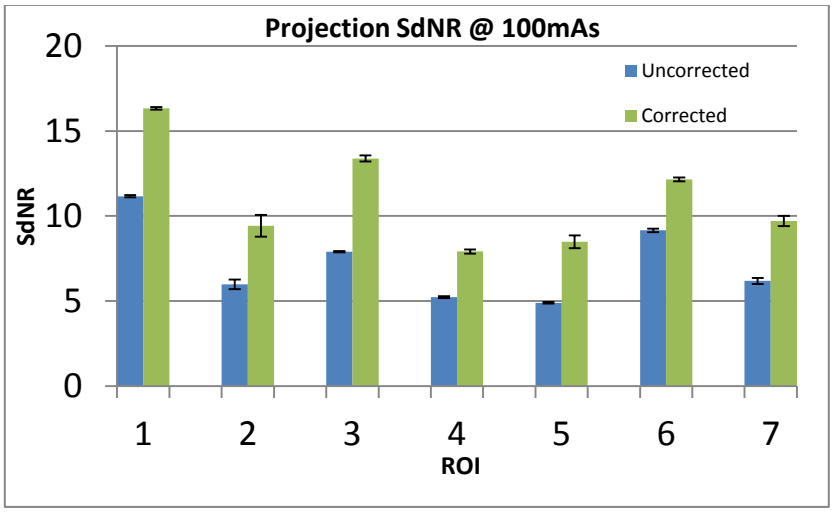

Figure 5-16: SdNR for different masses in the CIRS 013 phantom for the central projection at 6.7mAs exposure. Significant improvement in SdNR is observed with PSD scatter correction, with average improvement of 50%.

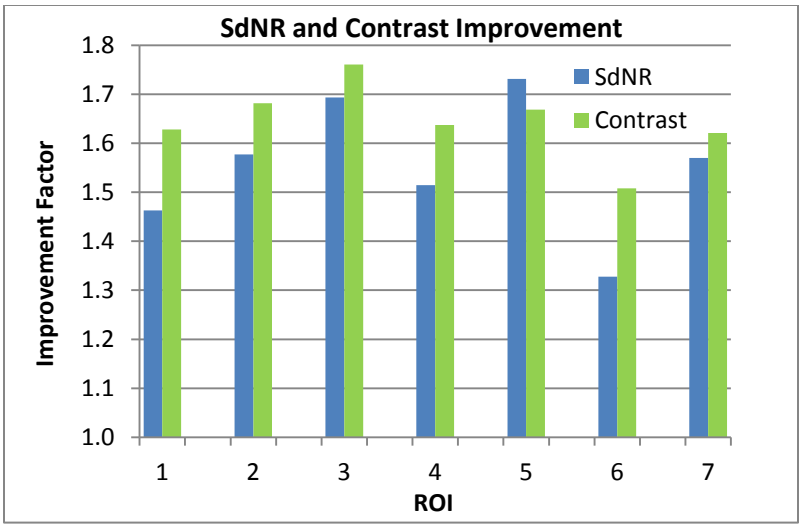

Figure 5-17: SdNR and contrast improvement factor for each ROI in projection images for the CIRS 013 phantom.

5.2.7.2.2 Tomosynthesis reconstruction slices

Reconstruction of the CIRS 013 phantom was performed with and without scatter correction. Slices were generated to represent 0.5mm thickness with 140um pixel size. Due to the inherent variation of gray level between corrected and uncorrected images, the window level and width are based on background values. The displayed images have a level equal to the mean of a background sample and the window is scaled with the standard deviation of the mean. Figure 5-18a shows a corrected reconstruction slice in the plane of focus of two masses, as indicated. Figures 5-18b-e are enlarged views of the masses taken from reconstruction slices generated from uncorrected and corrected projection data. Images 5-18b and c contain scatter. Images 5-14d and e are the corresponding scatter-corrected images. With the noise scaled similarly, the most visually apparent difference in the scatter-corrected slices is the increased feature contrast.

Figures 5-18f and g are line plots through the regions shown in 5-18a. Figure 5-18f shows the increased feature contrast for the indicated mass, measured through line 1. Note that the contrast is enhanced without loss of feature resolution, as demonstrated by the sharp edge transition. Figure 5-18g shows a reduction of cupping through an area with no masses, region 2, though the convex shape of the corrected profile could imply overestimation of scatter in some regions. Imaging of a non-compressible

homogenous material will be addressed in the next section of this chapter. The reconstruction slices display a substantial improvement in image quality as was found in the projection slices. The average increase in contrast and SdNR were 25% and 44%, respectively. Figure 5-19 shows the quantitative results for each mass evaluated in its plane of focus. Measurements were conducted on the same ROI used for projection analysis, as outlined in figure 5-10c. SdNR and contrast improvement are consistent for all ROI, independent of their location within the phantom. The masses span a range of depths within the phantom. The consistent improvement in SdNR and contrast, for both projection images and reconstruction slices, indicates that the technique is effective throughout the object, at the center and periphery.

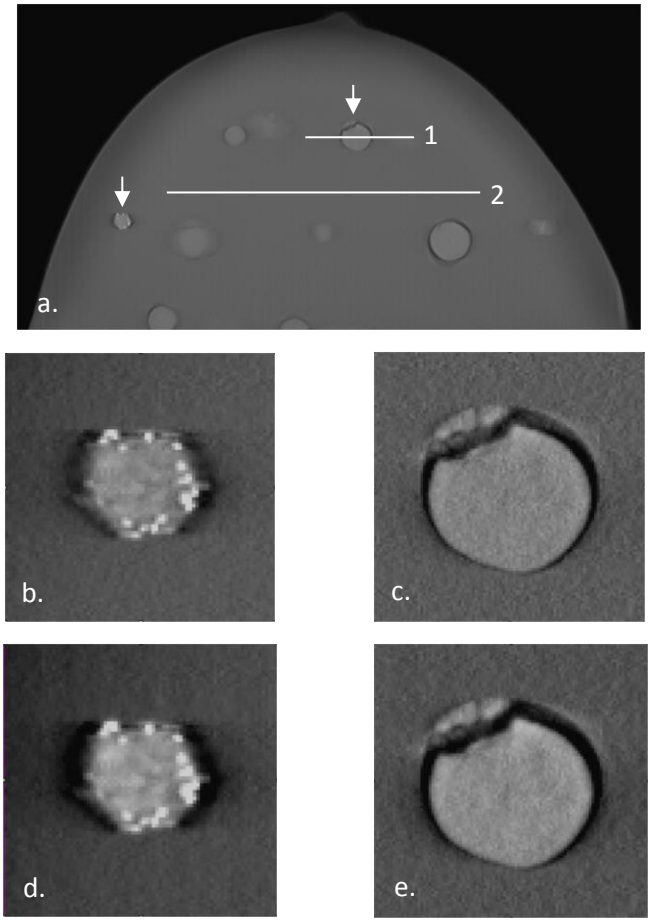

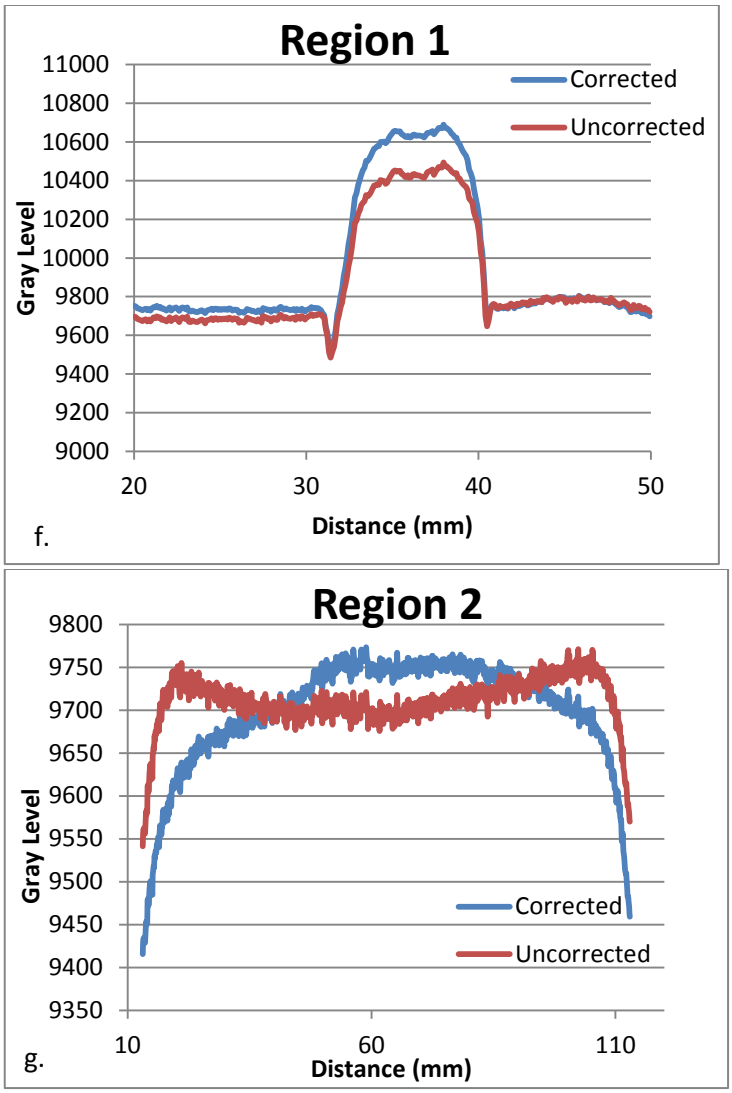

Figure 5-18: a) Reconstruction slice in a plane containing two focused masses; b-e) Images of a mass containing calcifications and mass #6 (top: uncorrected, bottom: corrected). A reduction of noise is seen in the scatter corrected images, yet the feature sharpness is not compromised. Figures f and g are line plots for the two regions shown in a. Object contrast is enhanced in f and cupping artifact is reduced in g.

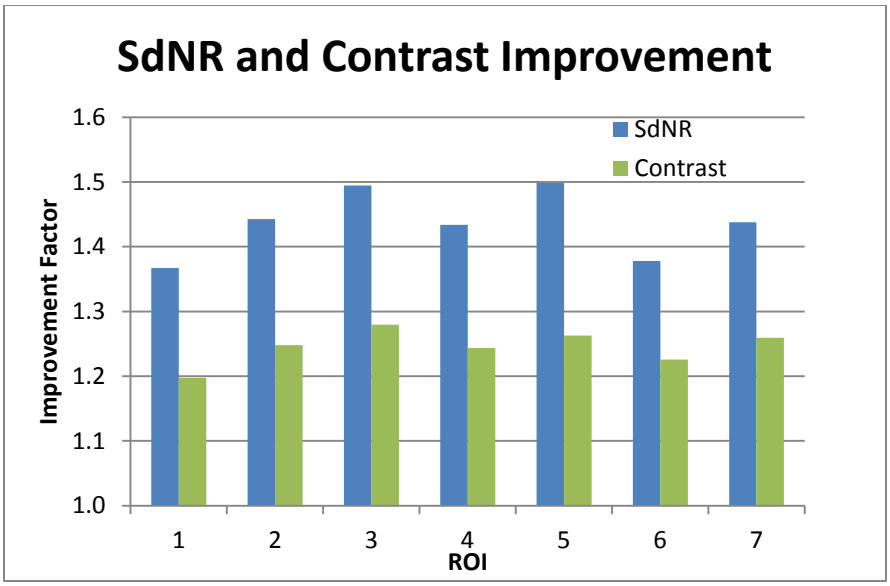

Figure 5-19: SdNR and contrast improvement for each mass within the reconstruction plane of focus. For the labeling of ROI see Figure 5-10c.

5.2.8 Discussion

The goal of this study was to develop a patient-specific scatter correction technique for tomosynthesis. Physical parameters of the PSD were investigated, optimized, and implemented for primary sampling scatter correction in the image acquisition. A CIRS biopsy phantom was imaged to study the performance of the PSSC method in breast tomosynthesis. Projection images were analyzed for contrast and SDNR and compared between uncorrected image and scatter corrected image. An average increase of 64% in contrast and 55% in SdNR in the projection images was measured after scatter correction with PSSC. Reconstruction images showed a smaller, yet substantial, increase in contrast, 25%, and SdNR, 44%. The PSSC outperformed the anti-scatter grid at equal exposure, therefore a dose savings may be possible with clinical implementation of the PSSC method.

The hole spacing and size used in this study were chosen based on empirical data incorporating only three percent of additional dose to the patient. These dimensions were chosen to minimize patient exposure and ensure accurate sampling of primary signal. Increase or decrease in the sampling frequency would impact the resolution of the scatter map, patient dose, and computational time. Using just 3% of

additional patient dose is a more efficient way to improve image quality compared to simply increasing the X-ray dosage. By implementing scatter correction with PSSC, we could achieve the same image quality in terms of contrast and SdNR with lower dosage or achieve better image quality at the current clinical setting. This will be especially beneficial for patients with large or dense breasts which have intrinsically higher scatter. The PSD parameters could be further optimized together with the image dose to offer a more effective scatter correction, namely optimization of PSD parameters for a slightly larger dose penalty to achieve better image quality. A recent study of the spatial variance of scatter [82] indicates rapid variation of the scatter profile at the chest wall and uniformity toward the center of the breast. The distribution of the PSD holes may be further optimized for more accurate sampling in transitional regions.

The scatter correction script was written in MATLAB and it required about 60 seconds for each projection on a quad-core desktop PC. The time could be reduced by utilizing a high performance computer, re-writing the scatter correction code in C with GPU acceleration, and integrating the scatter correction with the reconstruction software. The correction script currently uses a MATLAB function, *imdilate*, which dilates a region using a structured element disk to generate the sampling mask. In projection images from the most oblique angles, this results in occasional sampling of penumbral pixels, which results in overestimation of the scatter signal. Future versions of the code may utilize a slightly smaller element to ensure proper sampling at all angles and/or use the median value, as opposed to the mean, to exclude outliers.

One drawback to using the PSSC method clinically for breast imaging is the additional scan time. Integration of the PSD into the compression paddle would minimize the transition time from full field to PSD imaging, with a modest estimate of one to two seconds. Figure 5-20 demonstrates one possible configuration I have designed in which a folding PSD plate would be incorporated into the compression paddle. During imaging, the plate would be stowed out of the field of view (Figure 5-20a). After full-field scanning has been performed, the PSD would be rapidly deployed to sample the primary information

(Figure 5-20b, c). The design incorporates a flange to shield the hinged region and prevent unwanted primary beam transmission, figure 5-20d. The PSSC method in this study utilized a unique scatter profile for each projection image which doubles the scan time range from 2.5-4.8s currently, to 5-9.6s, increasing the patient discomfort and likelihood of patient motion. Though limited to some degree by breast compression, patient motion between the full field and PSD scans would impact the quality of the scatter correction. Since the scatter profile should vary little between adjacent sources, further analysis will be performed to determine the ideal number of PSD images. As demonstrated for breast CT [84], it may be possible to acquire fewer PSD images and approximate some of the scatter maps to save time and further decrease dose without compromising the improvement in image quality.

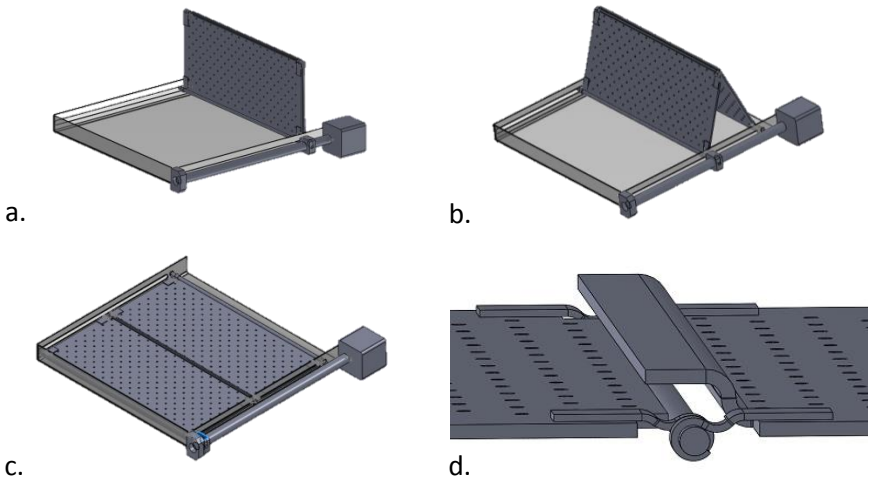

Figure 5-20: Hardware for potential clinical implementation into breast compression paddle; a) PSD folded; b) Deployment into FOV; c) PSD flat for primary sampling scan; d) detail view of shielded hinge assembly.

5.3 Patient-specific scatter correction for chest imaging

5.3.1 Digital radiography system

A commercial 2D chest radiography system (DRX Revolution, CareStream Health) was used to compare the PSSC technique with use of an anti-scatter grid. The DRX Revolution has a 1.2mm focal spot and variable source to image distance. The detector is a DRX-1C, with 139x139um pixel size and an active area of 2560x3072 pixels (35.6x42.7cm). An optional grid encasement can be installed over the detector for scatter rejection.

5.3.2 Stationary digital chest tomosynthesis system

An s-DCT system has been created in our lab, consisting of a carbon nanotube (CNT) X-ray source array (2008-08-L75-02, XinRay Systems LLC.) and a flat panel detector. The source contains a linear array of 75 X-ray emitting focal spots with 4mm pitch over 296mm. The average focal spot size per source is 2.5mm x 0.5mm. [33] The whole source array or subset of sources can be used for tomosynthesis imaging, with sources typically operated at 80kVp and 5mA of cathode current. Multiple detectors have been used with this system, with earlier studies performed on a 30x30cm panel (Varian 3030D, Varian, Inc.) and later studies performed on a larger, 40x30cm panel (Varian 4030X, Varian, Inc.). The source-detector distance (SDD) is variable from 100-130cm.

5.3.3 Primary sampling device (PSD)

5.3.3.1 First-generation device

Preliminary investigation into the use of PSSC for chest imaging used PSD geometry mimicking breast PSD, but scaled according to plate thickness. Due to the higher energy of the x-ray beam, lead was chosen as the plate material. To ensure complete attenuation of the beam in the background region, a 305x305x6mm plate was used. In order to maintain a similar acceptance angle, or aspect ratio, aperture diameters of 6mm were punched into the plate. A pitch of 31mm was used to maintain the 3% open area

used in the previous study, as this directly correlates to additional patient dose, for a total number of 85 apertures. Figure 5-21 is a photo of the first-generation device.

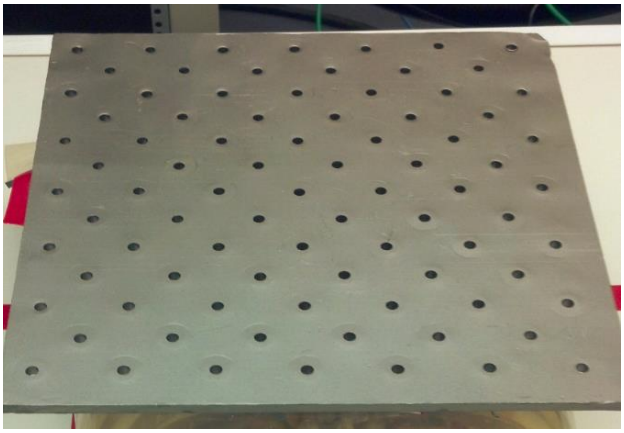

Figure 5-21: Initial PSD plate for chest imaging

5.3.3.2 Second-generation device

Based on results from preliminary studies, a larger PSD device was designed with smaller apertures and pitch for increased primary sampling and more accurate scatter interpolation. This PSD was made from a 3mm lead plate sandwiched between two 1.5mm aluminum sheets, incorporated for strength and to encapsulate the lead. The 2mm apertures were drilled at a pitch of 10mm covering 45x35cm, for a total of 1575 apertures. Aperture diameters were later increased to 3mm due to attenuation of the primary signal in the 2mm sampling regions. Figure 5-22 is a photo of the second-generation PSD for chest imaging.

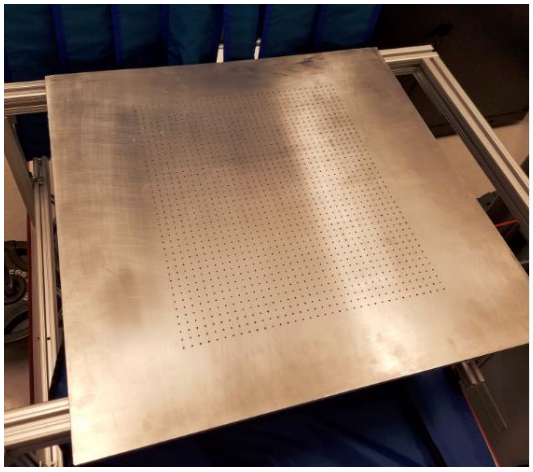

Figure 5-22: Second-generation PSD for chest imaging

5.3.3.2.1 Attenuation measurement

Similar to measurements outlined in section 5.2, the PSD was evaluated for attenuation in the background region. An image of the PSD with no object was evaluated in a background region and compared to a dark frame. The PSD values were approximately 100 counts higher than the dark image, so the attenuation of the plate is inadequate. This effect could be partially mitigated by subtraction of a scaled blank image, but full attenuation is more desirable.

5.3.3.2.2 Aperture size and pitch

Evaluation of PSD aperture size was performed using blank and PSD images to compare the relative values in the bright field for transmission. Three ROI were compared, shown in the PSD image, figure 5-23a. Due to source-detector geometry, region one is in the most intense and orthogonal part of the x-ray beam. Regions two and three are in areas of increasingly oblique trajectory. Plot profiles of each ROI, showing the PSD intensities (blue) and blank intensities (red) indicate that even at 3mm diameter, the PSD aperture size is not quite large enough. The transmission rate amongst the three sampling locations is very uniform, 83 $\pm$1%, lending itself to a constant value correction factor to scale primary samples to the proper amplitude and avoid scatter overestimation.

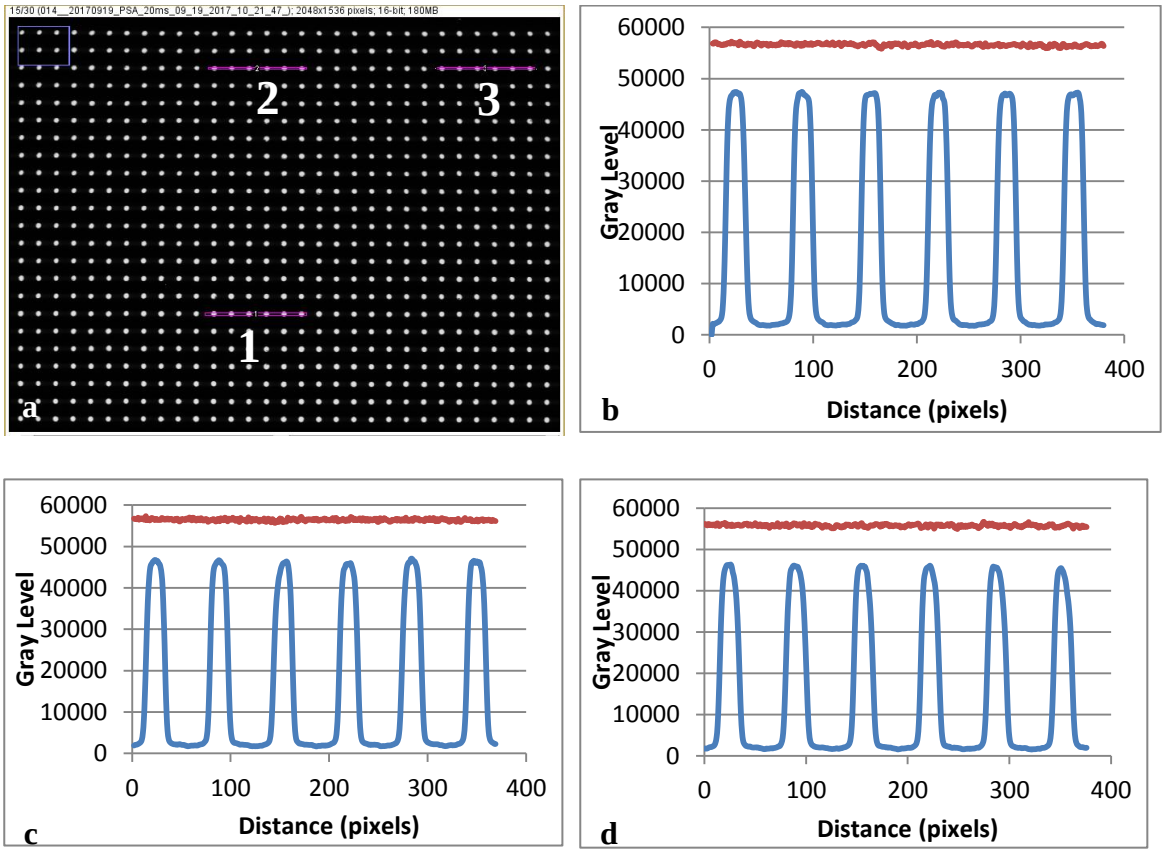

Figure 5-23: a) PSD image with no object for transmission indicating ROI for b-c; b-d) Plot profiles of ROI 1-3, respectively, comparing PSD with blank intensity.

Evaluation of the pitch of the PSD was performed using an image containing scatter to assess the crosstalk of scattering tails on the primary samples. A ROI was chosen in the center of an object known to have substantial scatter. The primary transmission is low in this region, but a plot profile reveals a fairly flat background signal. This implies that the aperture pitch is adequate to avoid scatter tail crosstalk. Though this is satisfactory, the PSD open area increased from 3% to 7% with the previous increase in hole diameter. An increase in pitch from 10mm to 15mm would reduce the open area, and therefore the additional patient dose, back to 3%.

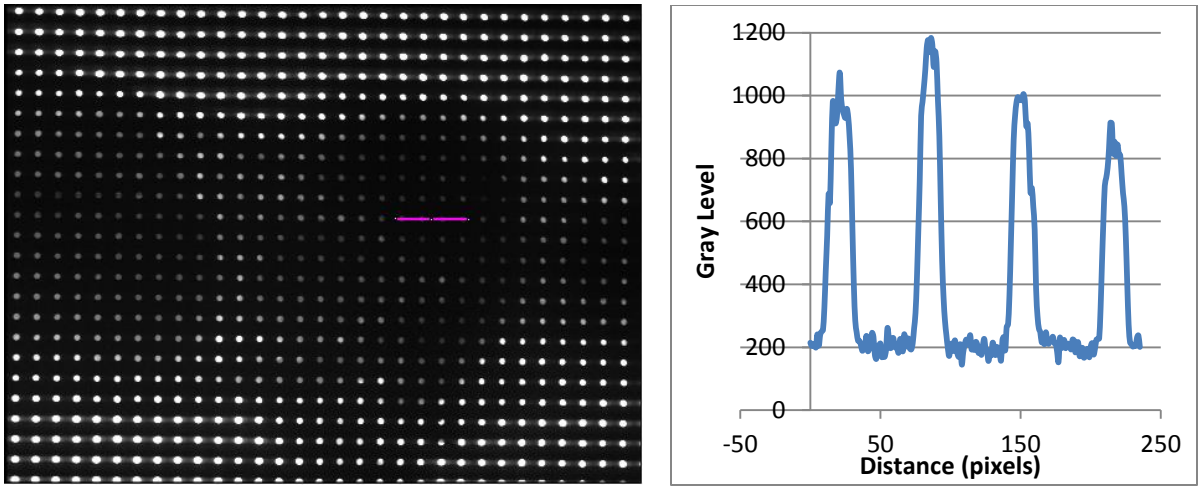

Figure 5-24: Evaluation of PSD scatter tails in an image with known scatter (a). The plot profile of the ROI shown in (a) indicates that the flat background scatter signal is not due to sample crosstalk.

5.3.3.2.3 Penumbral effects

The geometry of a thoracic imaging system is inherently larger than a breast system. The size of a typical human thorax can vary widely, so larger detectors are used. The thickness is also much greater, often 25cm or more. These factors place the PSD farther from the detector and covering a much larger area. Penumbral effects are therefore more difficult to avoid. Although subtle, it should be noted that the shape of the PSD sampling peaks in figure 5-23 is not as square as demonstrated in the breast imaging PSD. This is due to several factors, including larger PSD to detector distance, larger focal spot of the source, and smaller acceptance angle of the apertures. Future design of a PSD for imaging on this system would require weighing the cost of increasing the aperture size with regard to sampling frequency and impact on patient radiation dose.

5.3.3.2.4 Oblique transmission

Oblique transmission of x-rays at large incident angles was evaluated using the same PSD image from section 5.3.3.2.3. Figure 5-25 shows two zoomed ROI, one from figure 5-23 from a centrally

located sample (a), and one from a peripheral sample in an oblique image (b). Some distortion is visible in the oblique sample and use of a nine-pixel diameter sample region would include a substantial region of penumbral pixel values. As was the case with the breast PSD, this worst case scenario does not affect many primary samples, but could be mitigated by use of a smaller sampling region, filtered out via use of a standard deviation parameter, or use of a median signal, rather than mean. Future designs could incorporate a focused array of apertures, for use over a defined range of source-to-PSD distances, or use radially-increasing aperture diameter to compensate for cone beam photon trajectories.

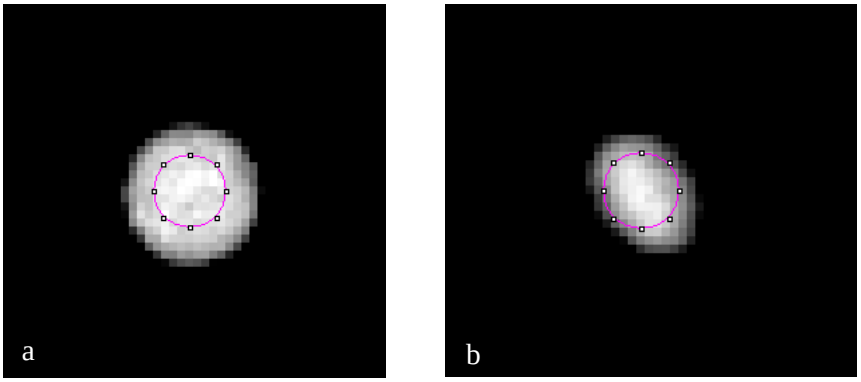

Figure 5-25: Zoomed ROI from the image displayed in figure 5-23a. Though the projected aperture shape changes from an orthogonal (a) to an oblique projection (b), a nine-pixel sampling region provides a reasonable margin. Window and level are adjusted to emphasize sample values.

5.3.4 Digital radiography imaging: PSSC vs. anti-scatter grid

Planar radiographs of an anthropomorphic thoracic phantom (Kodak Imaging) were acquired using a commercial 2D chest radiography system (DRX Revolution, CareStream Health). Full-field and PSD images were acquired using a standard anterior-posterior (AP) chest technique, 110kV and 3mAs, for processing via PSSC. Images were then acquired using the same technique, but incorporating an anti-scatter grid, or digital detector grid encasement, (DRW Grid Pro™, RC Imaging) with 103 lines and an aspect ratio of 6:1. Due to time constraints on system availability, the second-generation PSD was used for this study prior to validation experiments and subsequent enlargement from 2 to 3mm apertures. A

correction factor was used in an attempt to mitigate under sampling of the primary signal and overestimate of scatter.

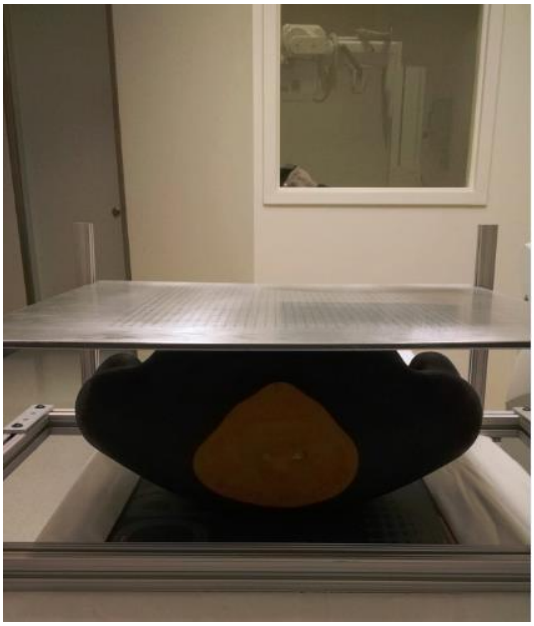

Figure 5-26: Anthropomorphic thoracic phantom and PSD situated for 2D imaging.

5.3.5 s-DCT imaging

5.3.5.1 First-generation PSD imaging

Preliminary studies were performed with the PSD outlined in section 5.3.3.1, with sparse sampling and large apertures (6mm). Tomosynthesis scans were performed utilizing phantom and cadaver subjects. Scans were performed with 31 projections at 80kVp with 5mA per projection and varied exposure time. Phantom images were acquired at 25 and 50ms beam-on-time per projection, resulting in radiation exposures of 3.86 and 7.75mAs per full scan, respectively. Scans were performed at an SDD of 112cm in standard full-field imaging mode, with the PSD, and subsequently, with an anti-scatter grid for quantitative comparison. Incident air kerma for the low- and high-exposures was

calculated to be 287 and 577uGy, respectively. This is in the range of current clinical chest tomosynthesis systems. [27] Cadaver images were acquired in the AP view at 100 and 130cm source-to-detector distance.

In each configuration, the PSD was placed on top of the object and a second scan was performed at equal tube exposure, with 3% transmitted to the object. Gain and offset scans were acquired for standard image processing prior to scatter correction.

5.3.5.1.1 Phantom imaging

Phantom images were acquired for evaluation of the method. The phantom consisted of a water-filled polyethylene vessel, 12 x 20 x 6cm, containing objects of varying attenuation, including closed cell polyethylene foam, polyethylene spheres, and stainless steel spheres. It was placed inside a hollow, anthropomorphic chest phantom. Figure 5-27a is a photo of the objects and their orientation within the water-filled vessel. Figure 5-27b is a photo of the phantom imaging scheme.

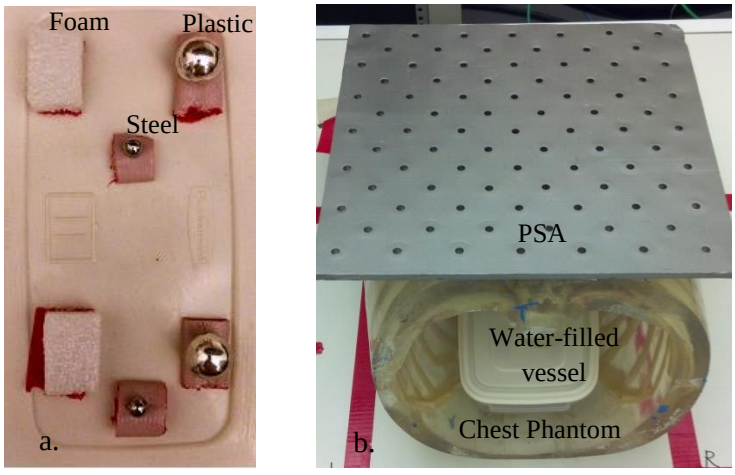

Figure 5-27: a) Photo of vessel inserts; b) Phantom imaging configuration

5.3.5.1.2 Cadaver imaging

An adult female thoracic cadaver was obtained through collaboration with colleagues in the UNC School of Medicine. The thickness of the thorax was 25cm.

5.3.5.1.3 Image analysis

Quantitative evaluation was performed for the phantom images using the signal-difference-to noise ratio (SdNR), previously shown in equation 5-2. SdNR was calculated utilizing the mean signal intensity within the object, μ_{obj}, mean signal in the nearby background region, μ_{bkg}, and their standard deviations, σ_{obj} and σ_{bkg}, respectively. Image measurements were performed in ImageJ. Quantitative analysis was done only for chest phantom projection images with embedded contrast objects. Cadaver images lack any well-defined, discrete features for quantitative analysis and were assessed qualitatively. Images were windowed individually to optimize feature conspicuity.

5.3.5.2 Second-generation PSD imaging

Subsequent imaging has been performed with the second-generation PSD device described in section 5.3.3.2, with 3mm apertures and 10mm pitch. The PSD placed 25cm above the detector using an aluminum support frame. For each phantom, a full-field image was acquired, and then the PSD was inserted without disturbing the phantom. The PSD image was acquired and images were processed with the PSSC method. Images were acquired using 29 sources over a range of pulse widths, 15-35ms, for total exposures of 2.28-5.08mAs. Reconstructions generated slice images representing 2mm of thickness, unless otherwise specified.

5.3.5.2.1 Homogenous slabs

One of the most commonly stated effects of scatter on 3D images is cupping, as demonstrated by the uncorrected image profile (red) in figure 5-18g. For a more accurate representation of this effect, and validation of the PSSC technique, homogenous slabs of water-equivalent plastic were imaged. The slabs covered an area of 14.6x14.6cm with a total thickness of 11.7cm. Figure 5-28 is a photo of the slabs placed on the detector under the PSD. The bright spots are generated by visible light from the alignment assembly on the s-DCT passing through the holes of the PSD, allowing visualization of the primary sampling locations.

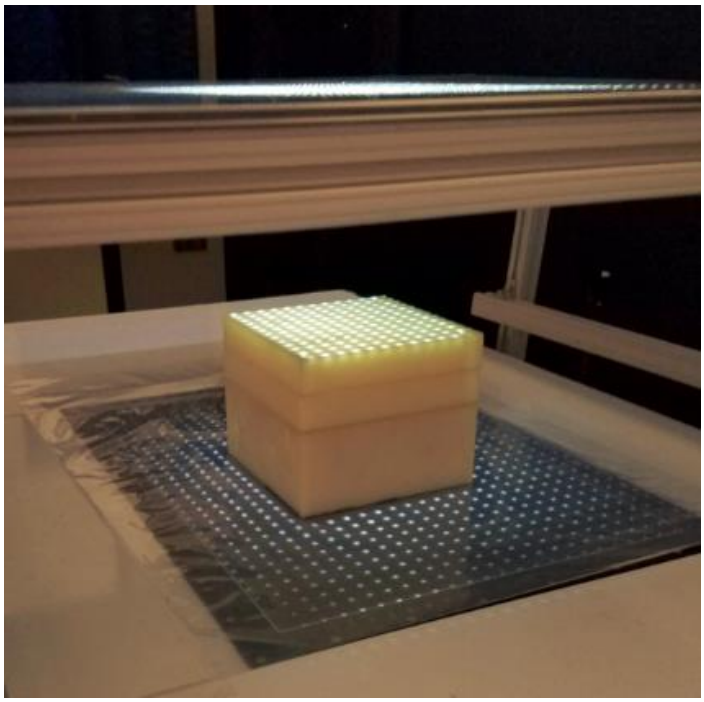

Figure 5-28: Homogenous slabs placed on the detector for PSD imaging. The illuminated regions are generated by visible light passing through the PSD apertures.

5.3.5.2.2 Anthropomorphic thoracic phantom

The thoracic phantom (Kodak) utilized in the 2D anti-scatter grid comparison was also imaged with s-DCT. Tomosynthesis scans were performed with and without the PSD using 18ms pulse widths for 2.6mAs total scan exposure.. Figure 5-29 is a photo of the phantom situated on the detector for PSD imaging.

Figure 5-29: Photo of the anthropomorphic thoracic phantom situated for PSD imaging.

5.3.5.2.3 QA phantom

For quantitative assessment of the PSSC method, a thoracic quality assurance (QA) phantom (Digital Phantom 07-646, Supertech X-ray) was utilized. This phantom is comprised of organ and bone-shaped metal sheets of varying attenuation to mimic anatomy. It also contains a wire mesh background material and test objects and line pair test patterns for evaluation of contrast and resolution. Because of the high attenuation of this phantom, a 35ms pulse width was used for a total scan exposure of 5.08mAs. Figure 5-30 is a photo of the phantom on the detector for PSD imaging.

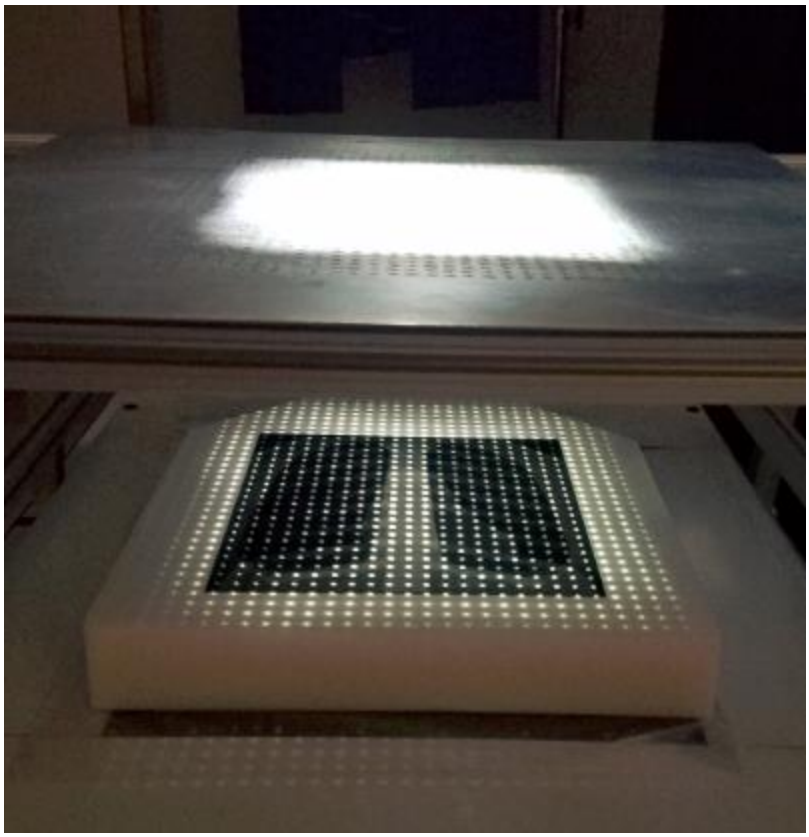

Figure 5-30: Photo of the QA phantom, situated for PSD imaging.

5.3.6 Porcine imaging

Phantom imaging is useful for quantitative assessment of image quality, but does not always represent outcomes for in-vivo studies. To validate the PSSC technique, a sedated free-breathing pig was imaged. Because image registration between full field and PSD images is critical to an accurate scatter approximation, images were acquired using physiological gating to the respiratory cycle. Each projection was acquired at peak inspiration, typically used in thoracic imaging when pulmonary features are of interest. Images were acquired at 20ms pulse width per projection for a total exposure of 2.9mAs. Figure 5-31 is a photo of the sedated animal on the imaging bed, situated under the PSD. Respiration was monitored with a veterinary physiological monitoring system, utilizing a pressure transducer secured under an elastic belt (arrow).

Figure 5-31: Photo of sedated pig, situated for PSD imaging. Respiration was monitored using a pressure transducer secured with an elastic belt (arrow).

5.3.7 Digital radiography imaging results

The PSSC method was evaluated in comparison to an anti-scatter grid using a commercial 2D system. Projection images were acquired of the thoracic phantom using the chest radiography system (DRX Revolution, CareStream Health) in full-field, PSD, and anti-scatter grid configurations. An AP chest technique was used, incorporating 100kVp and 3mAs exposure. Figure 5-32a is the PSSC scatter corrected image with a defined ROI in the lower thoracic spine. Figures 5-32b-d are zoomed to this ROI for comparison of uncorrected (b), anti-scatter grid (c), and PSSC (d) images. The PSSC image shows better definition of the vertebrae than either the uncorrected or anti-scatter grid images. The grid image (c) displays lower image quality than the uncorrected image (b) due to primary photon attenuation.

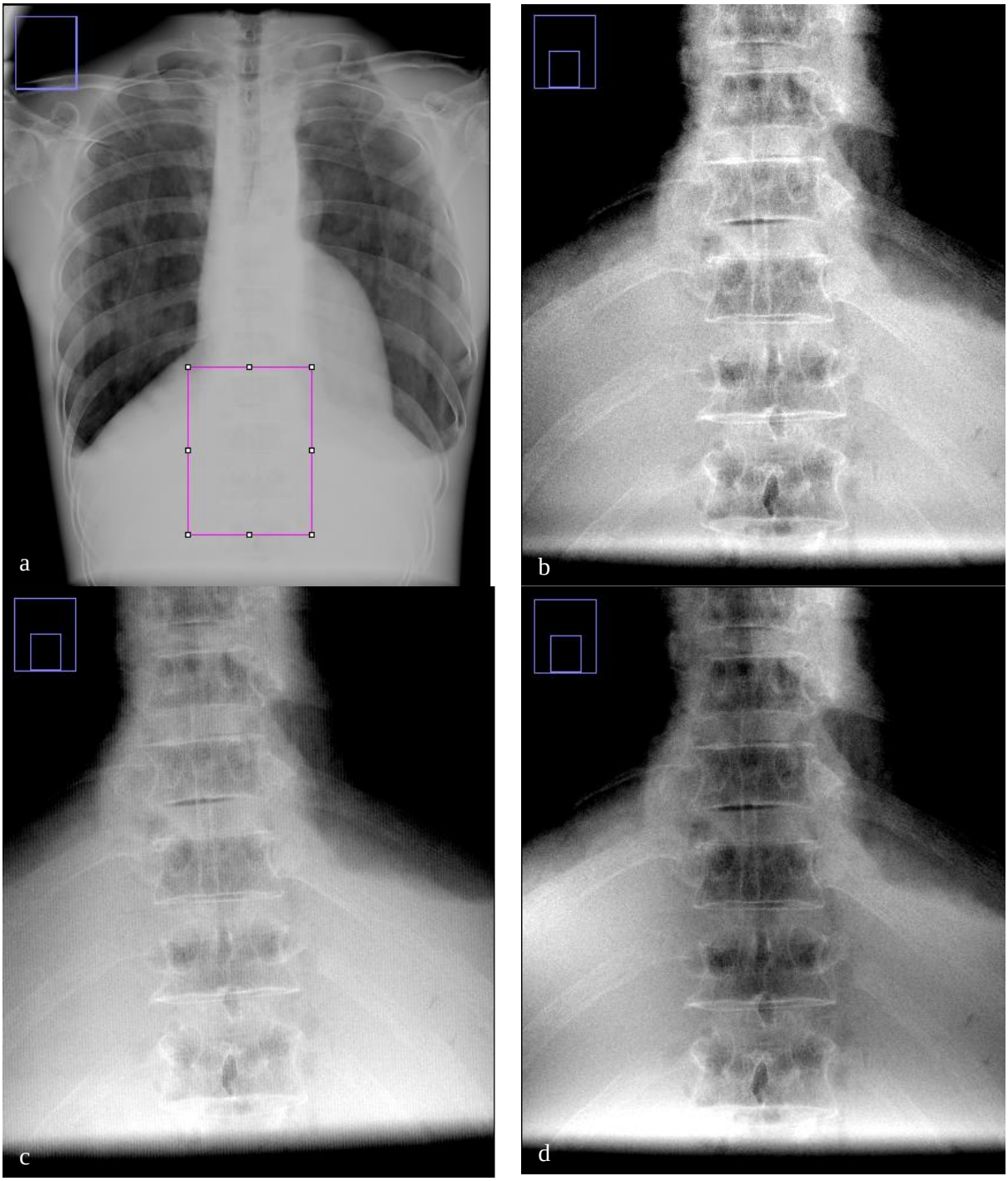

Figure 5-32: a) Scatter corrected image of the thoracic phantom defining an ROI; b-d) uncorrected, anti-scatter grid, and PSSC images, respectively.

5.3.8 s-DCT imaging results

5.3.8.1 First-generation PSD

5.3.8.1.1 Phantom images

Representative phantom projection images are shown in figure 5-33. Figure 5-33a is a scatter-corrected projection from the central source, and 5-33b is the associated scatter map used for correction. Figures 5-33c and d depict magnified regions of interest and object sampling for computation of SdNR outlined in 5-33a. The foam blocks and steel spheres were visible in all images, but the polyethylene spheres did not appear in any set of images, due to their similar attenuation to water at 80kV. (μ/ρ=0.184cm^2/g for water and 0.182 for polyethylene; National Institute of Standards and Technology (NIST) X-ray mass attenuation database) Four objects were assessed for quantitative comparison between the 7.75mAs exposure original uncorrected images, 3.86mAs and 7.75mAs exposure PSD corrected images, and 7.75mAs exposure images with the grid. Comparisons were made utilizing projections from varying angles. Similar results were observed at all angles with results from the central projection shown in figure 5-34. The original, uncorrected images displayed similar results to the images acquired with the grid. Both the low- and high-exposure PSD images demonstrated improved SdNR over the original and grid images.

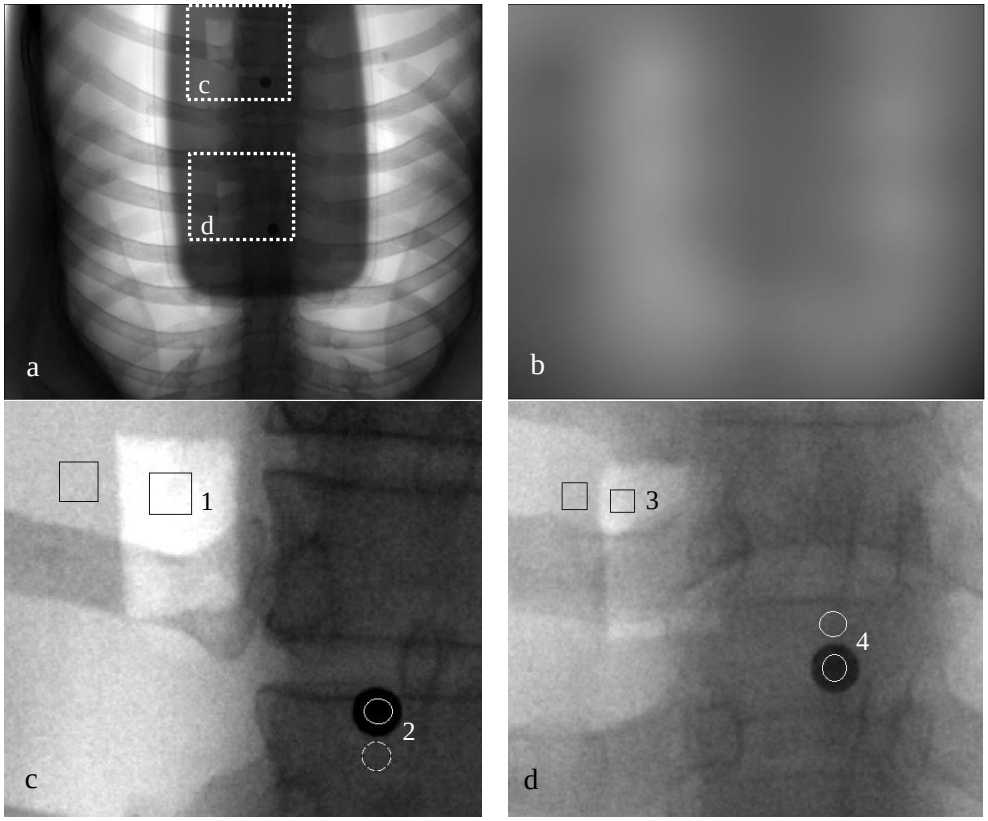

Figure 5-33: a) Scatter-corrected projection image depicting regions of interest; b) scatter map used for correction; c) upper ROI in a); d) lower ROI in a).

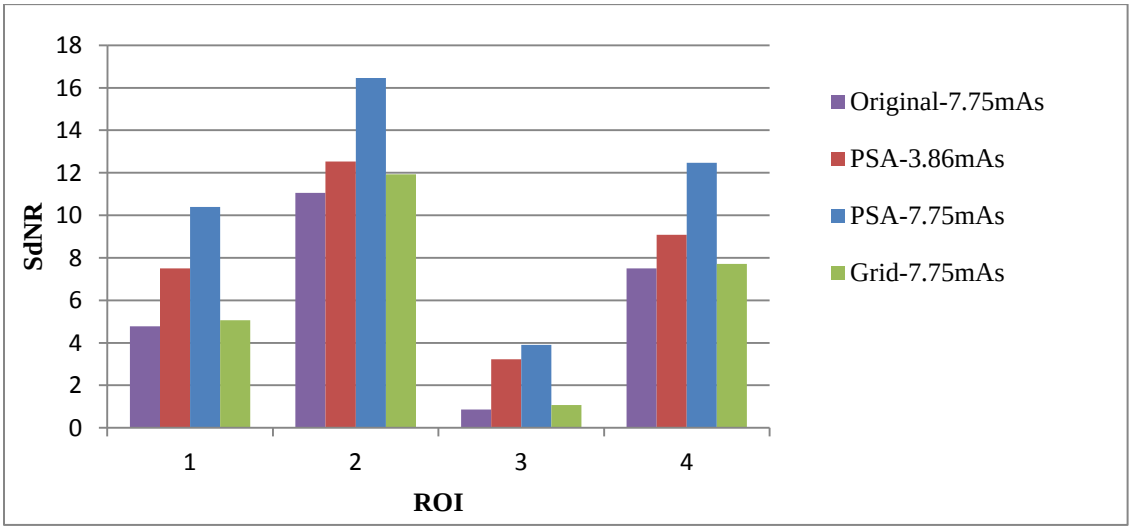

Figure 5-34: SdNR for each ROI in phantom projection images. As can be seen, the SdNR for PSA scatter corrected image increases significantly over that of the uncorrected images. The SdNR for the PSA scatter correction also significantly outperforms the anti-scatter grid for the same object exposure, which has very limited impact on SdNR under the constant exposure.

5.3.8.1.2 Cadaver images

Scatter corrected projection images demonstrated a marked increase in conspicuity of features in comparison to the non-corrected projections. Sample projection images are shown in Figure 5-35a) uncorrected and b) scatter-corrected. Sample reconstruction slices are shown in Figures 5-35c) uncorrected and d) scatter-corrected. Scatter-corrected images exhibit a broader distribution of gray levels, allowing visualization of more features at any window/level.

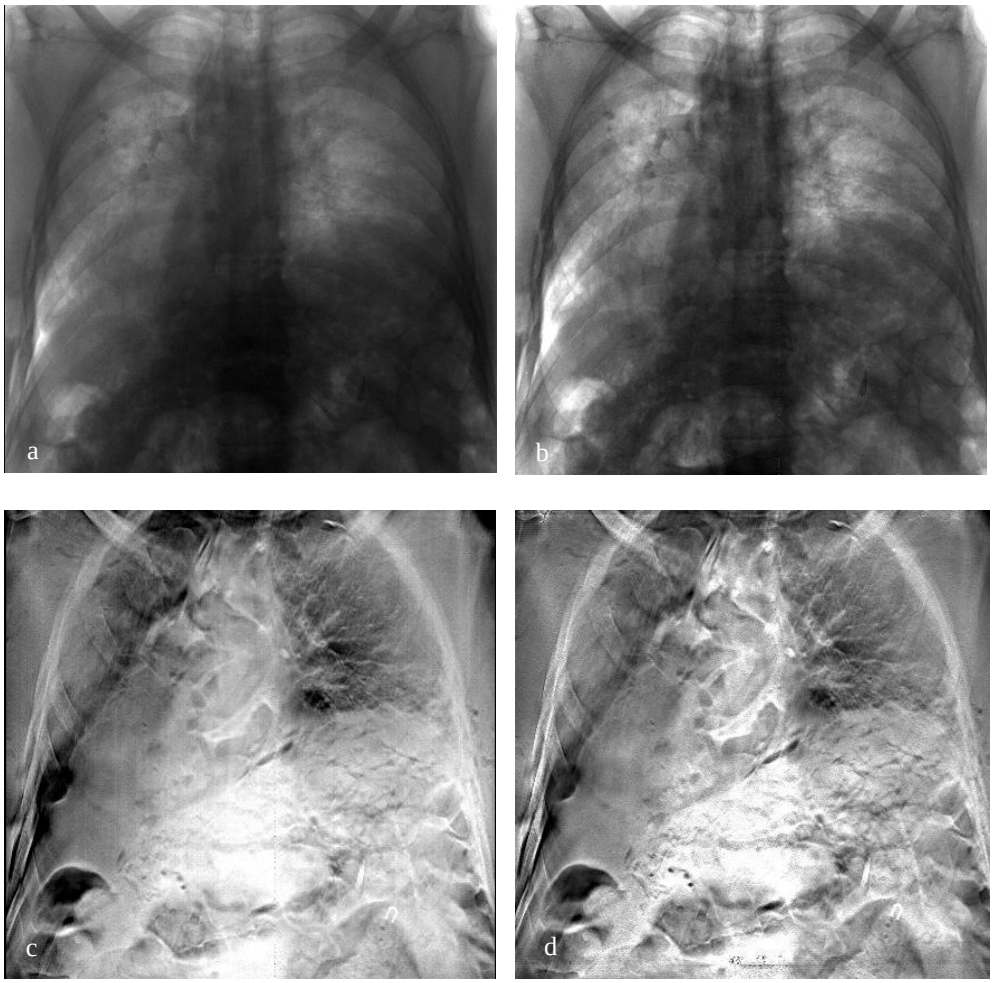

Figure 5-35: Cadaver projection image (a) without scatter correction and (b) with scatter correction; (c) reconstruction slice without scatter correction and (d) with scatter correction.

5.3.8.2 Second-generation PSD phantom imaging

5.3.8.2.1 Homogenous slab images

Slabs of homogenous tissue-equivalent plastic were imaged to evaluate the PSSC method in the reduction of the cupping artifact. Images were reconstructed with and without scatter correction. Figure 5-36 shows reconstruction slice images in the plane of focus of one of two cylindrical cavities. An ROI was chosen in a homogenous region for the uncorrected (a) and PSSC-corrected (b) reconstruction slices. Figures 5-36c and 5-36d are the corresponding plot profiles for 5-36a and 5-36b. The uncorrected slice displays a cupping artifact due to scatter, which is substantially reduced to a nearly flat profile in the PSSC-corrected image.

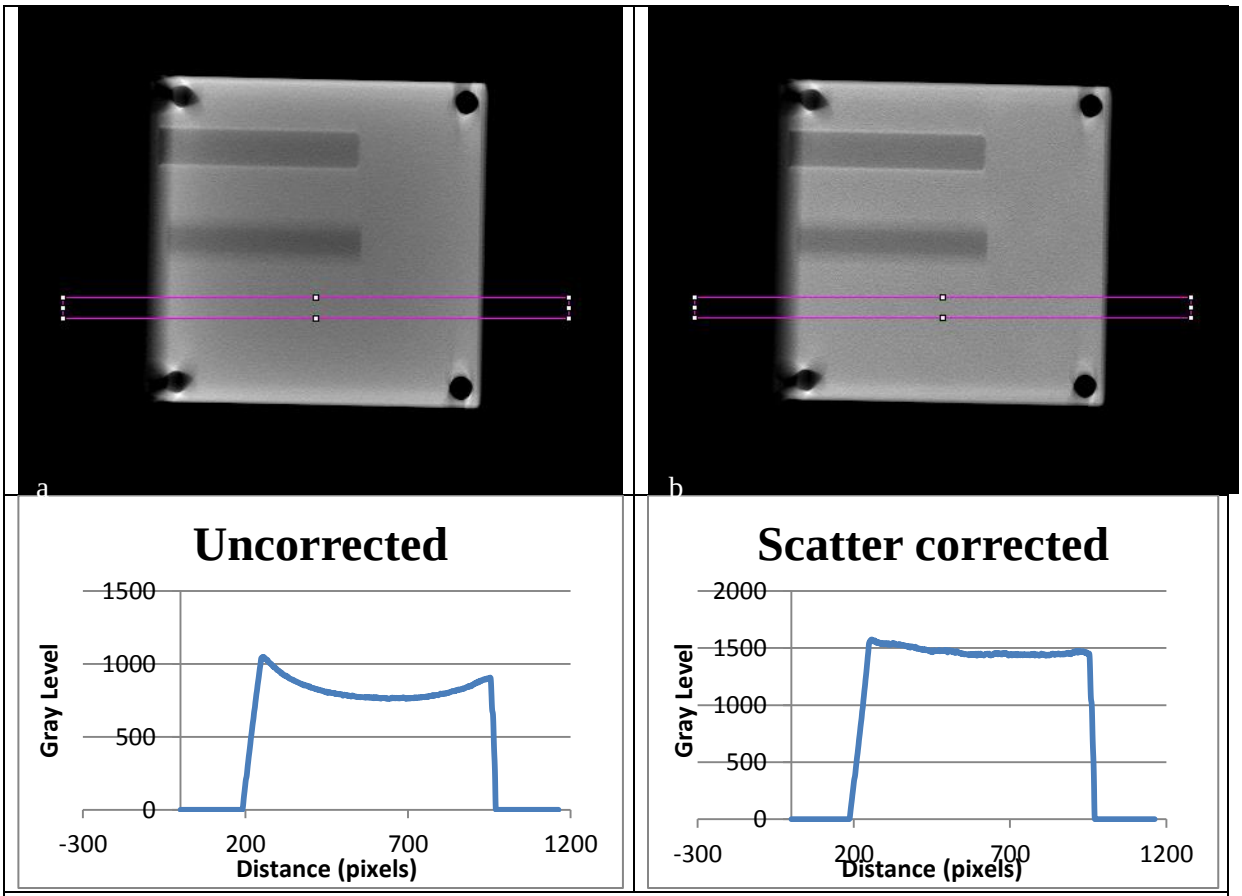

Figure 5-36: A ROI for a) uncorrected and b) corrected reconstruction slices of tissue-equivalent slabs; c) and d) are the corresponding plot profiles showing substantial reduction of the cupping artifact.

5.3.8.2.2 Thoracic phantom images

The anthropomorphic thoracic phantom was imaged at 18ms pulse width for a total exposure of 2.6mAs. Figure 5-37 shows the uncorrected central projection image (a), the interpolated scatter map (b), scatter-interpolated PSSC image (c), and f-SPR PSSC image (d). The images have been inverted, with window and level optimized to a region in the lung. The uncorrected image displays lower feature contrast in the lung than the scatter corrected images. The abdominal region does not offer any anatomical detail at this window and level. The SI (c) and fSPR (d) scatter corrected images do not display any macroscopic difference when compared to one another, but display higher feature visibility within the lung than the uncorrected image. The scatter corrected images also reveal details in the abdominal region, including lower thoracic vertebrae, at this window and level. The scatter map displays more texture than the scatter map produced with the first-generation PSD (figure 5-33b) due to the increased sampling density.

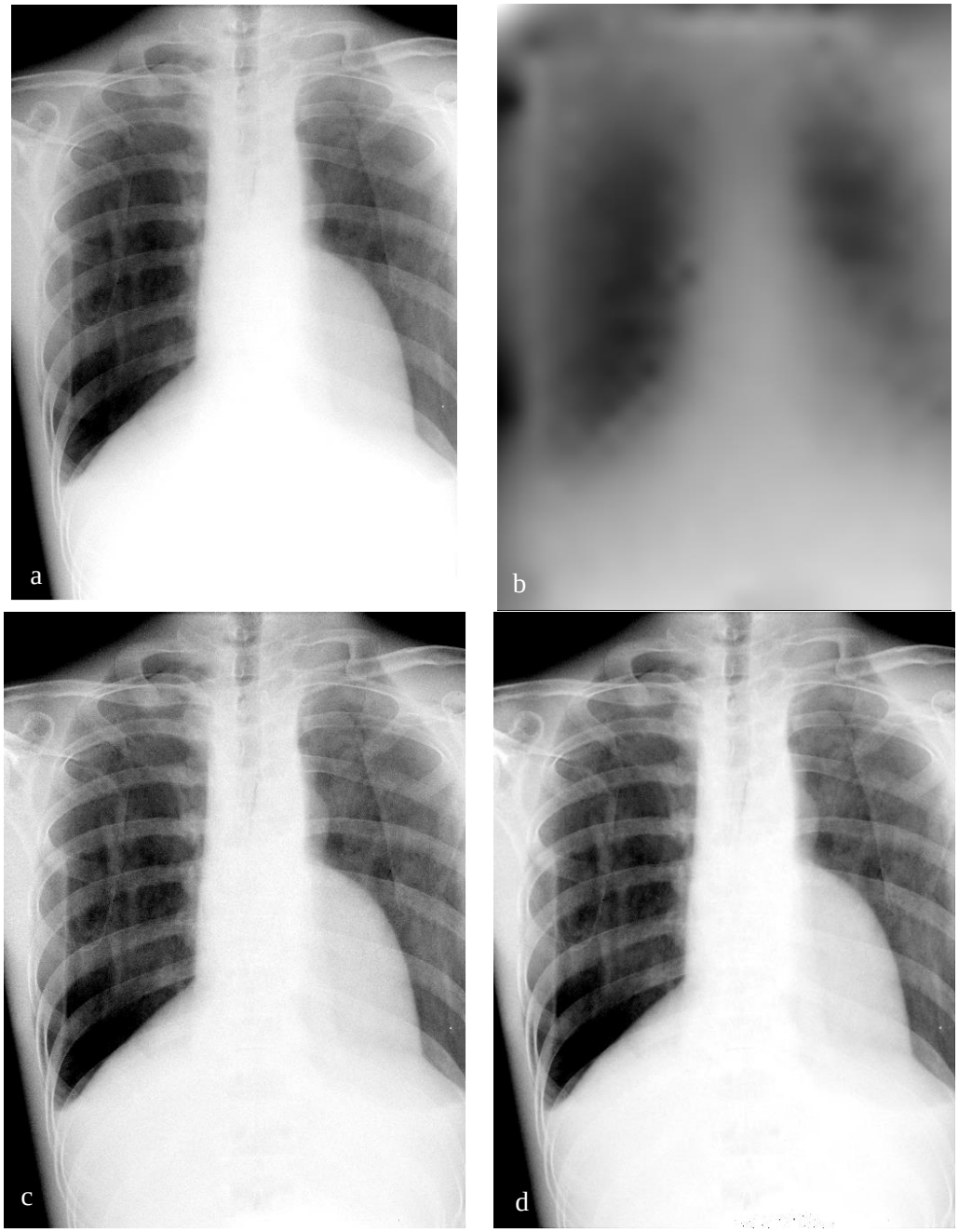

Figure 5-37: a) Central projection image without scatter correction; b) interpolated scatter map; c) SI corrected image; d) f-SPR corrected image

Reconstruction slice images of the thoracic phantom are shown in figure 5-38. Both are windowed to a region in the lower thoracic spine. The uncorrected slice (5-38a) exhibits a smoother texture with lower feature contrast than the SI scatter-corrected slice (5-38b). The uncorrected slice image was adjusted to enhance the contrast in the zoomed ROI (c) to match the scatter corrected ROI (d),

but non-uniformity of the background signal does not allow simultaneous optimization of the T9 and T12 vertebrae. Corresponding plot profiles of the ROI shown in figures 5-38c and d are shown in 5-38e and f, respectively.

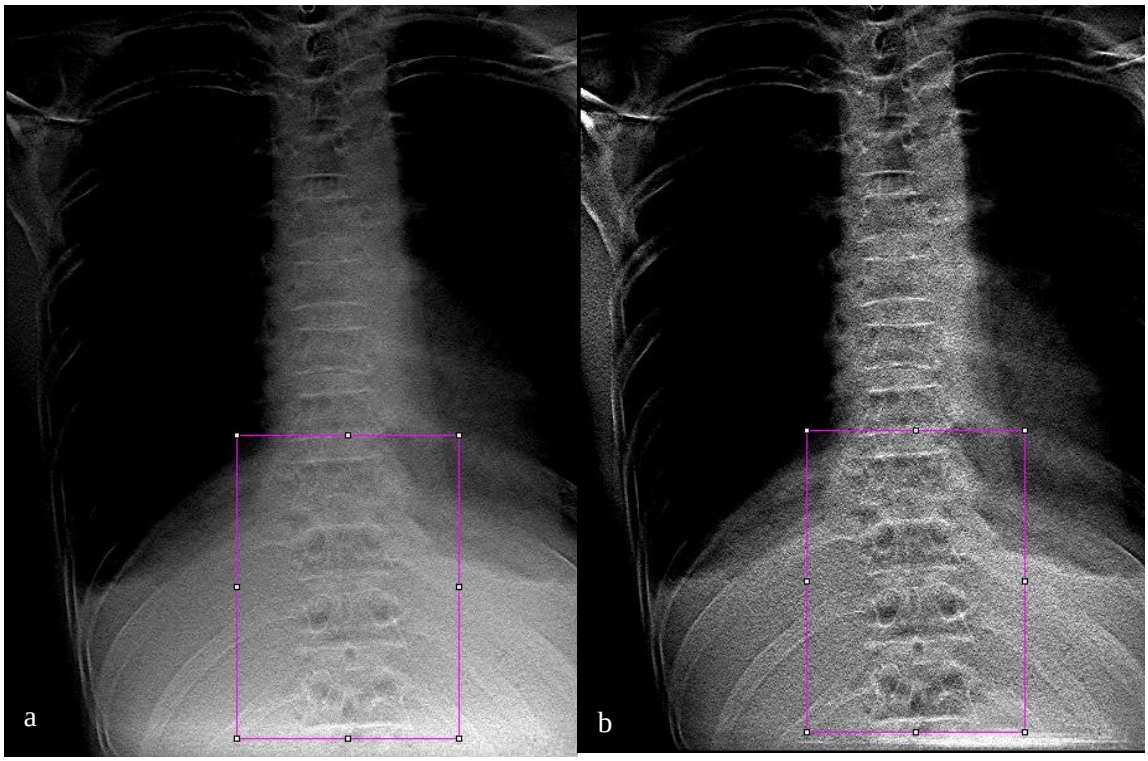

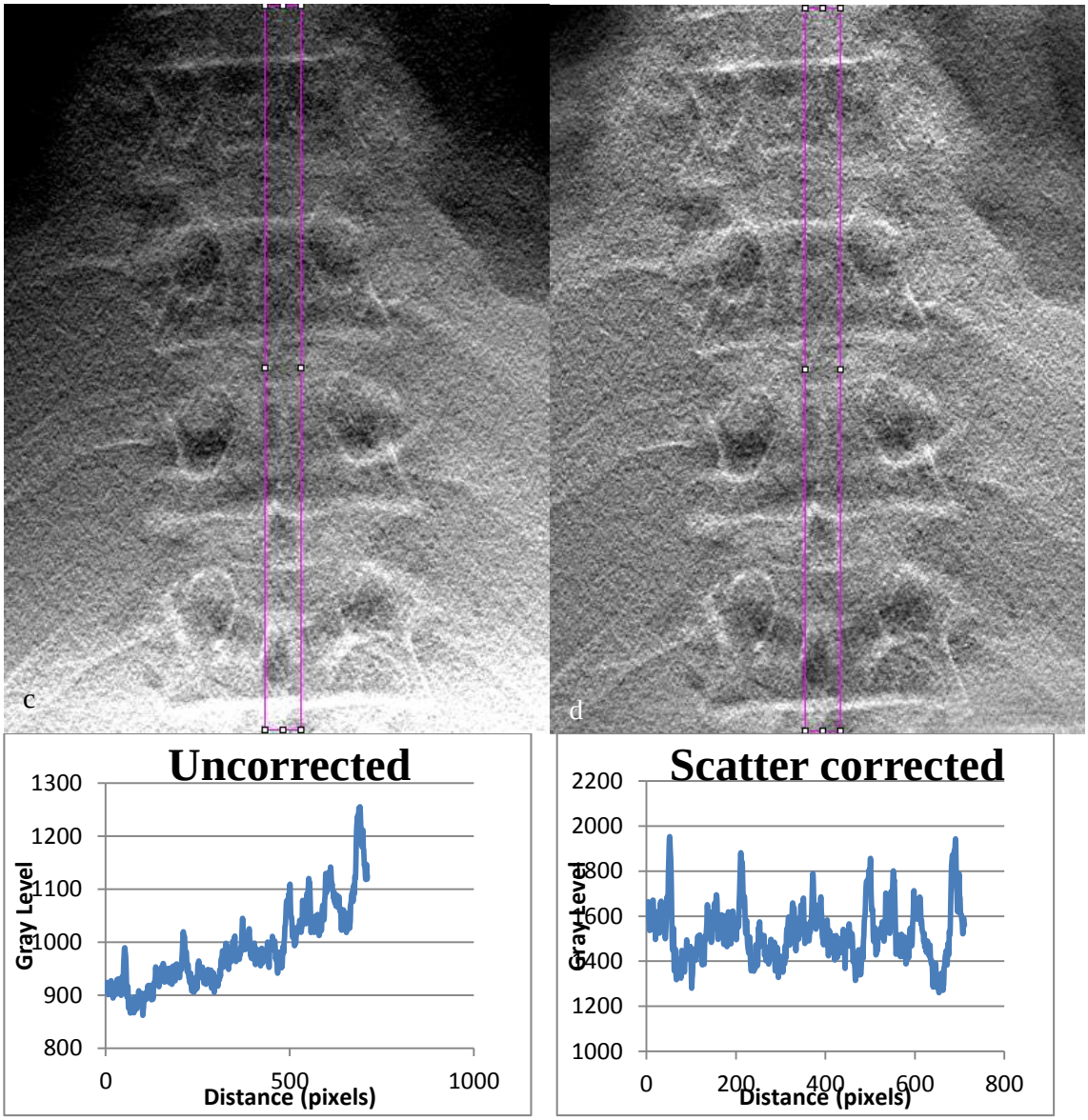

Figure 5-38: Reconstruction slice images of the thoracic phantom, (a) uncorrected, and (b) SI corrected. Window and level were optimized for the rectangular ROI in the lower thoracic spine. Manual adjustment of the zoomed ROI of the uncorrected image (c) and scatter corrected ROI (d). Plot profiles of the vertebral ROI in the uncorrected image (e) and scatter corrected image (f) show differences in the shape of the background signal.

5.3.8.2.3 QA phantom images

Images of the QA phantom are shown in figure 5-39. Reconstruction slices within the object layer are shown in 5-39a-c, with window and level optimized to both the lung and abdominal test pattern ROIs indicated. Figures 5-39d-f are the corresponding zoomed regions of the abdominal pattern, with window and level optimized for that region. The test pattern contains a 5x5 matrix of contrast objects, of

which 15 are visible in the uncorrected and scatter corrected images. The only notable differences in the images are the smoothing and edge blurring of objects as well as reduction of contrast within the wire mesh of the fSPR corrected image (figure 5-39f). Figures 5-39g-i are zoomed ROI within the lung test object region for each image type, with window and level readjusted for this region. No substantial difference is noted within this pattern, either. The line pair phantom is also visible in this ROI, with no difference noted for resolution. The 2.5 lp/mm feature, third from the left, is the highest resolution that can be achieved in this imaging configuration. It should be noted that the plane-of-focus for the object layer in this phantom is only 24mm from the detector surface, therefore the amount of scatter generated beneath it is considerably lower than in the other phantoms assessed in this study. Inversion of the phantom would likely produce images with a greater degree of scattering.

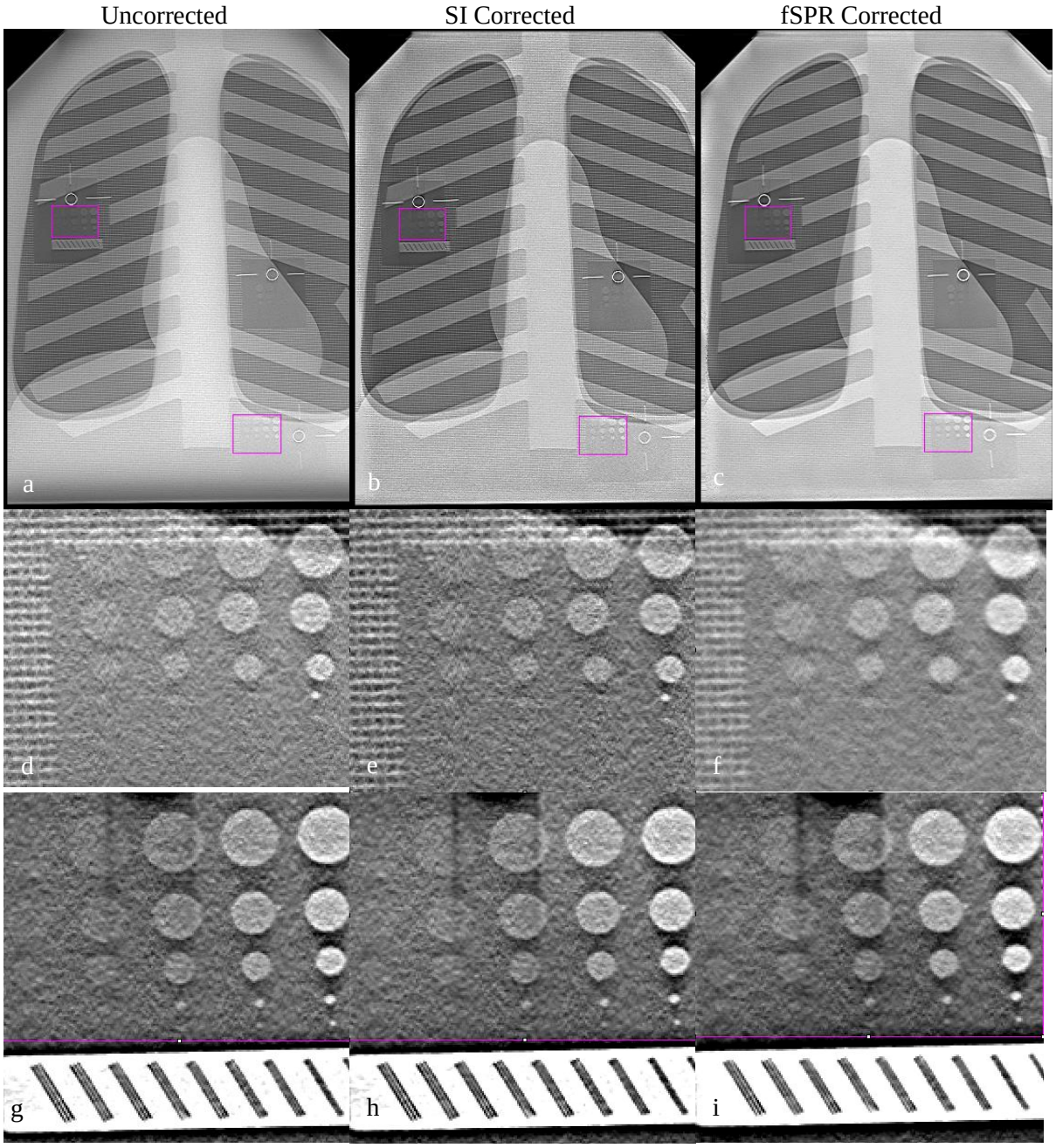

Figure 5-39: Reconstruction slice images in the plane-of-focus of the object layer. a-c) Uncorrected, SI corrected, and fSPR corrected slice images of the phantom indicating the lung and abdominal ROI; d-f) Zoomed ROI of the abdominal contrast objects; g-i) Zoomed ROI of the lung contrast objects and integrated line pair phantom.

5.3.8.3 Porcine images

In-vivo porcine imaging was performed to evaluate the PSSC technique. Full field projection images were acquired during peak inspiration of the respiratory cycle. The PSD was inserted and a second sequence acquired. Registration between these sets of images is critical for accurate scatter mapping, so global motion of the animal or variations in the inhalation amplitude could produce low-frequency artifacts. Because respiratory gating is generally used to increase the visibility of airways, they are used as the ROI for this data set. Figure 5-40 shows reconstruction slice images through the plane of focus of the airways. Figure 40a-c are the uncorrected, SI corrected, and fSPR corrected slice images with the ROI indicated. Image window and level was adjusted to optimize the ROI. As with phantom studies, corrected images display a more uniform appearance than the uncorrected image. No unusual artifacts are noted in the corrected images. Figures 5-40d-f are the zoomed ROI of the airways, which are most visible in the SI corrected image. Though it contains more noise than the others, it displays elevated contrast in comparison to the uncorrected image and more crisp delineation of the airway with respect to the surrounding tissue than the fSPR corrected image.

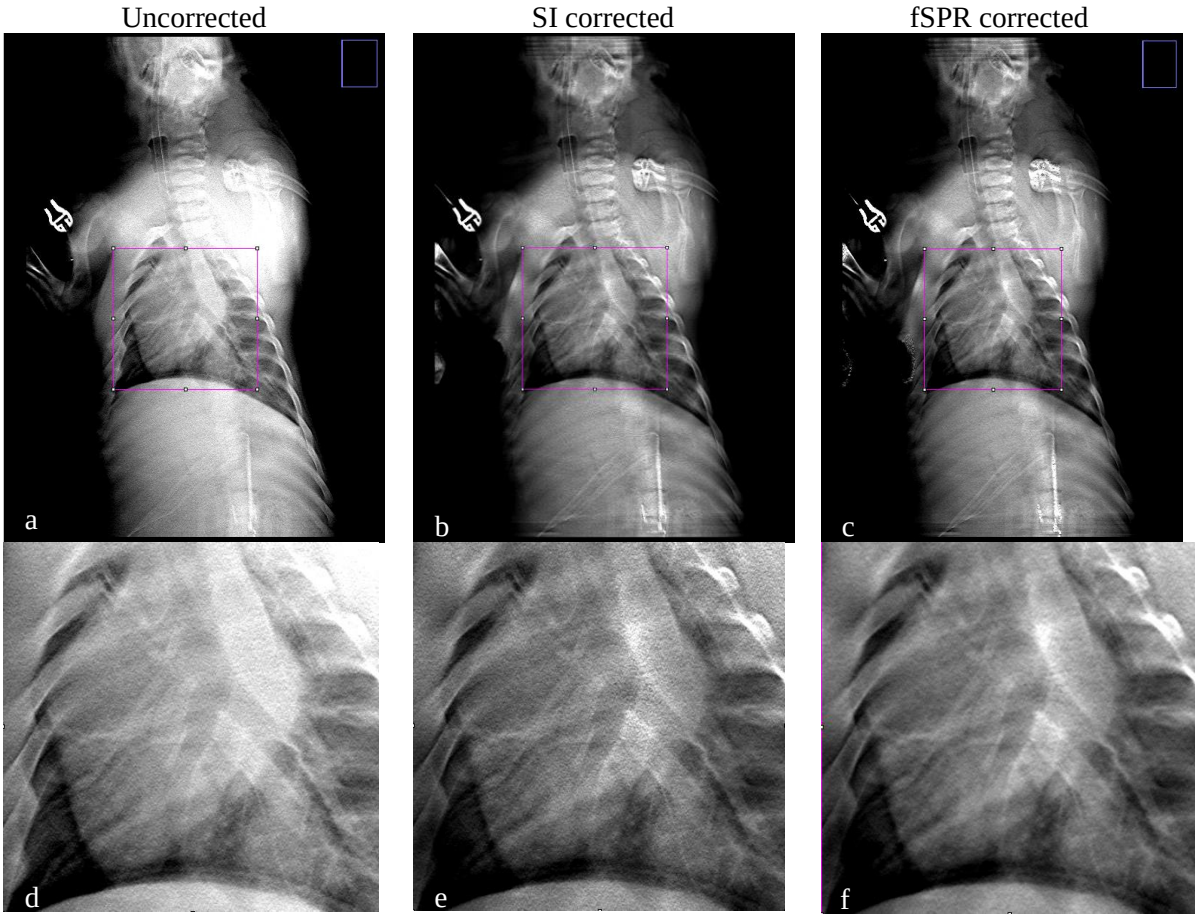

Figure 5-40: Reconstruction slice images without (a) and with SI (b) and fSPR scatter correction (c) display a change in feature contrast; d-f) corresponding zoomed ROI of airways.

5.3.9 Discussion

5.3.9.1 First-generation PSD imaging

We have investigated the PSSC scatter correction technique, which previously has been demonstrated to be effective for breast imaging, for chest projection and tomosynthesis imaging. Due to the substantially higher scatter rates in chest imaging, the potential gain is even greater. The PSD plate in this study had a sampling geometry with 3% open area, contributing only 3% of additional exposure to the object compared to full field imaging without an anti-scatter grid. Effectiveness of the method was measured with respect to images obtained with an anti-scatter grid. It is found that the PSSC technique

significantly increases image quality, as demonstrated by quantitative analysis of SdNR in phantom images and qualitative assessment of cadaver images.

Phantom projection images corrected with the PSSC method demonstrated a substantially higher SdNR compared to the uncorrected and grid images. The poor performance of the grid with respect to the uncorrected images is expected due to the substantial blockage of the primary beam by the grid, thus increasing quantum noise due to the lower photo count. The scatter correction offered by the grid is countered by the attenuation of primary information, resulting in similar SdNR. A surprising result is the superior performance of the low-exposure PSD with respect to the high-exposure grid images. This suggests dose sparing of greater than 50% may be possible in clinical use. For this preliminary study, the phantom objects provide assessment at opposite ends of the attenuation spectrum. As the foam blocks were chosen for their low attenuation as a lung mimic, the results are encouraging and imply the method may be useful in lung nodule detection. The steel spheres were chosen simply as a high attenuation material and do not mimic any typical anatomical features, but imply effectiveness in patients with metallic implants. Cadaver reconstruction images with scatter correction demonstrate visibility of more features at any single window/level than the uncorrected slices. Similar relative image quality was observed across all exposure levels for corrected vs. uncorrected images. Visibility of more anatomical landmarks at one level should improve speed and accuracy in reading diagnostic images.

The first-generation PSD contained 6mm apertures with 31mm spacing. The relatively large size of the apertures ensured full primary beam transmission, but forced the sparse sampling to maintain the low dose penalty exhibited in the breast studies. The positive findings of this prototype prompted design of a second device for larger detector coverage, smaller apertures, and denser sampling.

5.3.9.2 Second-generation PSD phantom imaging

5.3.9.2.1 Second-generation PSD

A second PSD was fabricated from 3mm lead and 3mm of aluminum with 2mm apertures and 10mm spacing, still maintaining the 3% open area of previous studies. This device was investigated and found to be too restrictive on the primary beam transmission. Apertures were enlarged to 3mm to increase transmission, increasing the open area to 7%. This would result in an additional dose penalty that could be compensated by decrease in full-field image exposure, fewer PSD projections, or creation of a new device with 15mm aperture pitch. The additional dose incorporated by use of the PSSC technique is still far below the dose penalty for use of an anti-scatter grid.

5.3.9.2.2 Comparison of PSSC method to anti-scatter grid

The second-generation PSD was used to image the anthropomorphic chest phantom on a digital radiography system for comparison to use of an anti-scatter grid. This study was performed prior to enlargement of the apertures, though still produced favorable results. The PSSC image displayed better feature contrast of the vertebrae by removing the overlying scatter signal. Though further investigations are warranted, use of the PSSC technique for planar radiography may result in an overall decrease in patient dose and/or increase in image quality compared to grid use.

5.3.9.2.3 Cupping

One of the primary effects of scatter in 3D radiography is cupping, wherein the attenuation of the material appears falsely low in the center. Reduction of this effect is valuable, particularly for imaging regions of high scatter, such as the brain. Imaging of the homogenous slabs demonstrated that the PSSC technique accurately removes cupping artifacts. Investigations into the benefit of PSSC for brain CT are underway.

5.3.9.2.4 Anthropomorphic thoracic phantom

The scatter corrected projection images of the thoracic phantom (figure 5-37) display a broader range of anatomy at a single window and level. The corrected reconstruction slice image (figure 5-38) also demonstrates better visualization of features due to removal of the non-constant background scattering signal. Though the slices appear somewhat noisier than uncorrected slices, the ability to visualize small variations in attenuation in lung and bone simultaneously has clinical value.

5.3.9.2.5 QA phantom

The QA phantom used in this study was not particularly well-suited for scatter reduction due to the close proximity of the object layer to the detector. The contrast test objects and line pair phantom produced similar results regardless of scatter correction. This result implies that implementation of the PSSC technique for thoracic imaging may be conditional based on diagnostic application. Features of interest lying near the detector are not subjected to scatter contamination as much as objects positioned 20 cm anterior. For example, spinal imaging may not benefit from PSSC as much as pulmonary or cardiac imaging in an AP view.

5.3.9.3 Porcine imaging

In-vivo porcine imaging is the closest approximation we have to use of PSSC in a human patient. The results were promising, with the airways displaying more contrast and conspicuity in the corrected slice images. The SI corrected image had better feature resolution than the fSPR image, due to the inherent blurring of airway walls due to SPR filtration.

Respiratory-gated images of the sedated subject are a nearly ideal case for both gating and the PSSC technique. The respiration of the animal was very uniform and there was no global motion. This ensures that each projection image is acquired at the same lung volume for effective “stop motion”. The full field and PSD images were acquired sequentially and showed good image registration. The respiratory consistency varies substantially with non-sedated, free-breathing human patients, particularly

pediatric patients. Application of the PSSC technique for tomosynthesis in respiratory-gated human patients would pose additional challenges. Current scan time for the s-DCT system is approximately 6 seconds in non-gated mode. Use of two sequential scans in one 15s breath hold is reasonable for full field and PSD acquisitions.

5.3.9.4 Conclusions

Only two PSD configurations were explored in this study and further investigations into dose penalty should be performed. A greater number of samples and/or non-uniform sample distribution may produce more accurate scatter mapping. Scatter maps from adjacent sources were also observed to be very similar and utilization of a reduced number of PSD images should be investigated. One drawback to the PSSC method is the doubling of scan time due to the PSD acquisition. Longer scan times would likely result in more image blurring due to patient motion. Utilization of a fast detector and/or reduced number of PSD images would reduce the scan time.

Overall, the PSSC method is effective at reducing scatter and enhancing conspicuity of delicate low-attenuation features within a large body. The potential dose savings offered by this method warrants further exploration, as it may be practical for clinical implementation in DCT. Figure 5-41 is a CAD drawing of a potential clinical implementation for our s-DCT system. A hinged PSD assembly is shown mounted to the tube stand to be translated either mechanically or manually, into the FOV.

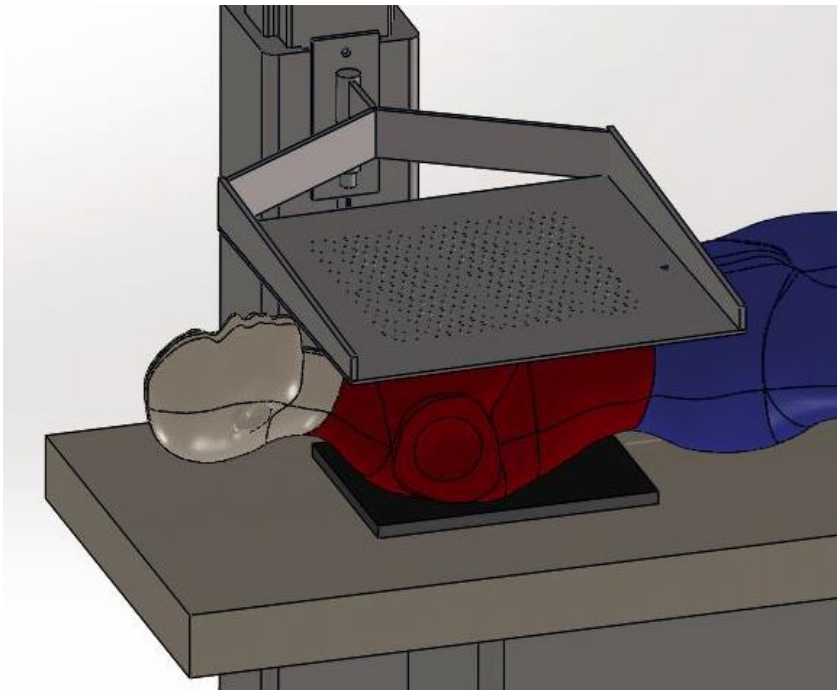

Figure 5-41: CAD model of a potential clinical implementation of the PSD on the s-DCT

5.4 Estimated scatter correction

Scatter maps generated using the PSSC method display some similarities to the original full field projection, with a large degree of blurring and lower intensity. Investigations into scatter estimation were performed using the full field and blank images.

The full field image was blurred via filtration with a Gaussian function in MATLAB. This is similar to the method in which the SPR map is filtered to generate the fSPR map, but using a much larger pixel count. The filtered full field image was then scaled to generate gray levels in the range of the previously calculated scatter maps. This scatter estimation method has been successfully applied to both phantom and patient data sets. Example images of the thoracic phantom are shown in figure 5-42. Figure 5-42a is the calculated scatter map from the central projection image and figure 5-42b is an estimated scatter map of the same image, with an ROI designated for analysis. Corresponding plot profiles of the calculated and estimated ROI are shown in figure 5-42c. The estimated scatter map is a reasonable approximation of the PSSC map and further investigation is warranted to determine if this technique may be a clinically viable solution.

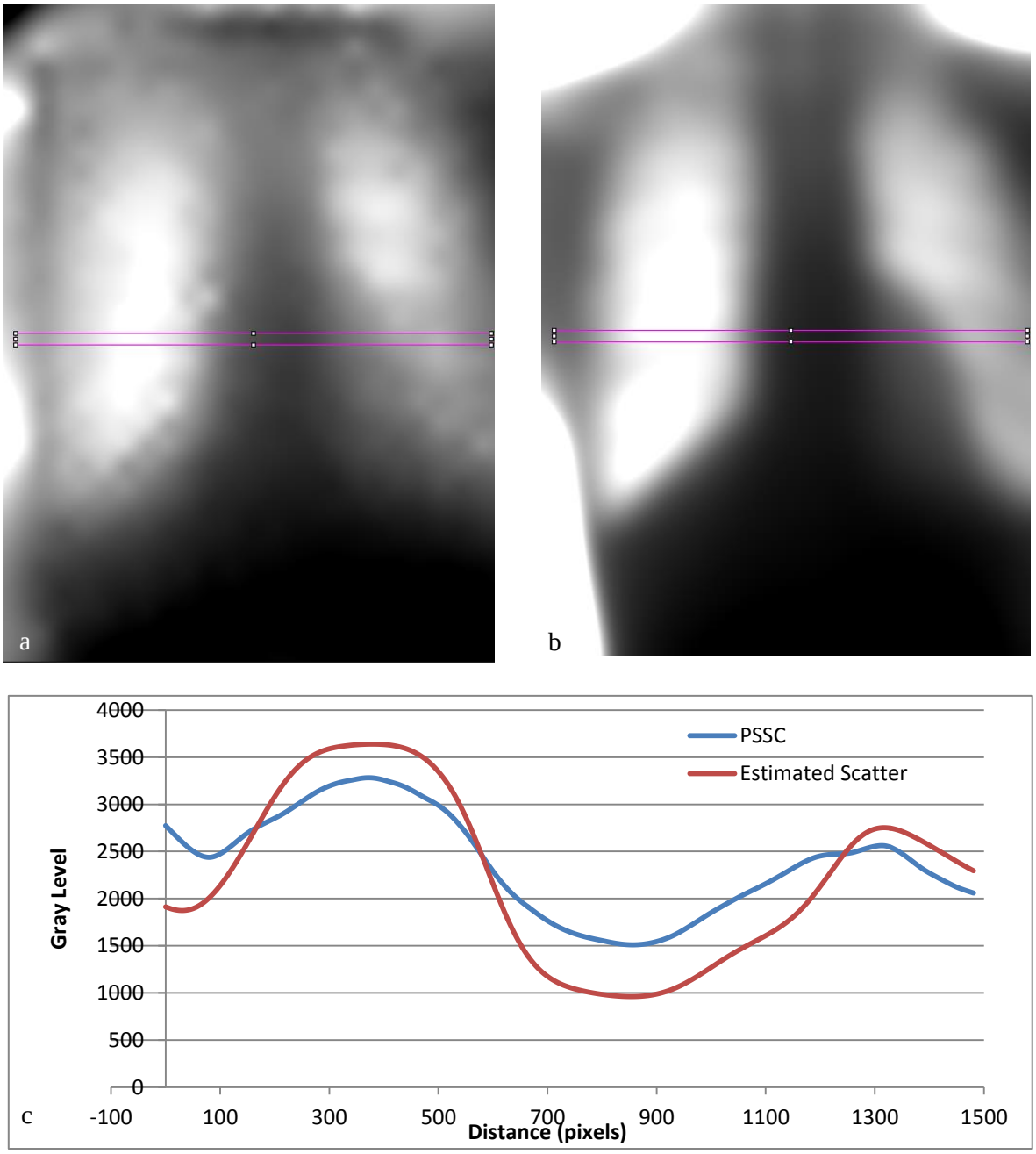

Figure 5-42: PSSC (a) and estimated scatter map (b) for the central projection image of the thoracic phantom. Plot profiles of the ROI (c) indicate that the estimated scatter map accurately conveys the shape of the scatter profile.

5.5 Conclusions and future work

The studies performed in both breast and chest radiography have shown that this technique is well suited for correction of projection images. Corrected images are easier to window and display a larger range of feature visibility than their uncorrected counterparts. Patient dose may be decreased by implementation of the PSSC technique in lieu of use of an anti-scatter grid.

Implementation for tomosynthesis was also successful and demonstrated improved feature conspicuity and contrast. Use of the PSSC technique in tomosynthesis poses some challenges regarding PSD insertion, patient motion, and scan time. The insertion of the PSD can be automated and rapidly placed in the FOV. Potential clinical implementations presented here could be used on our existing tomosynthesis hardware for patient imaging. Patient physiological motion can be addressed by respiratory, and perhaps cardiac, gating, or use of breath holds, which are currently used in clinical tomosynthesis imaging. Global patient motion may be difficult to compensate, but may be a problem for which estimated scatter correction can mitigate. The extension of scan time due to PSD imaging is undesirable, but can be reduced by limiting the number of PSD projections.

The primary sampling scatter correction has been performed with both a scatter interpolation method as well as a filtered scatter-to-primary ratio method. Numerical comparison of these techniques often includes noise reduction, in which the fSPR technique inherently outperforms SI. This reduction of noise comes at the expense of loss of resolution of fine details. The effect of this will vary depending on the application, such as visualization of small microcalcifications. Personal preference of the radiologist will also be a factor, in which some prefer a grainy image to one that is artificially smooth. A reader study of the PSSC technique would include an arm to assess the visibility of various lesion types with SI and fSPR correction.

Promising results of the PSSC studies have prompted pursuit of a human clinical trial for chest tomosynthesis, pending funding and IRB approval.

CHAPTER 6: CONCLUSIONS AND FUTURE WORK

The work presented in this dissertation is the culmination of six years of intermittent work on scatter correction and two years of s-IOT system development and implementation. Though each piece stands alone as individual project with little overlap, the common thread is the propulsion of CNT x-ray technology into multiple clinical modalities.

The development of s-IOT for clinical use has been a rapid process. With initial images acquired and feasibility demonstrated in 2015, only two years passed before the clinical prototype was installed in the UNC SOD. Barring the oppressive paperwork due to conflict of interest, a human image would have been acquired at that time. This fast clinical translation is due to the extensive experience of our lab members and the excellent collaboration we have built with the expert dental radiologists at the SOD. My role in this project was to perform the hard science that led us to final design parameters, then subsequent system characterization, evaluation, and pre-clinical studies.

Future work on s-IOT will involve investigations into additional clinical applications. As the current configuration is strictly for bitewing image acquisition, this will involve construction of new hardware for varying detector positioning and orientation. Investigation into additional applications such as implant site assessment and post-surgical follow up will require development of hardware and imaging protocols, as well as dose optimization.

The idea of using primary sampling for scatter correction was not a new one at the onset of this project. Though demonstrated in breast CT, it had not been developed for tomosynthesis. Several members of our team have been involved with development and/or utilized this technique over the years, but the hardware development and big picture implementation have been my focus. The PSSC method

has been used for multiple applications with positive quantitative results and feedback from our in-house radiologist. The remaining issue of scan time and awkward hardware implementation will be considerations for actual clinical implementation.

Future work on the PSSC method will involve reduction of scan time, with several potential solutions. The acquisition of a subset of projections with estimation of missing data is one approach to investigate. Another approach is to acquire multiple primary samples in a single image and segregate the samples into individual datasets. Investigation into patient imaging with the PSSC method has been incorporated into a recent proposal with good prospects of being funded. If accepted, hardware will be developed to incorporate the PSD image acquisition into our existing chest and/or breast tomosynthesis systems.

The contributions I have been allowed to make to our research team extend far beyond the scope of this thesis project. It has been an honor to assist in the development of CNT x-ray technology and translation into the clinic. I look forward to participating in development of the next generation of CNT device applications.

DISCLOSURES

Otto Zhou has equity ownership and serves on the board of directors of Xintek, Inc. and XinVivo, Inc., to which the technologies used or evaluated in this thesis have been or will be licensed. Jianping Lu has equity ownership in Xintek, Inc. and XinVivo, Inc. Xinray Systems is wholly owned by Xintek, Inc. All of these relationships are under management by the University of North Carolina's Conflict of Interest committee.

REFERENCES

[1] J. Prince and J. Links, Medical Imaging Systems and Signals, Upper Saddle River, NJ: Pearson Prentice Hall, 2006.

[2] R. Behling, Modern Diagnostic X-ray Sources, Boca Raton, FL: CRC Press, 2016.

[3] J. Iannucci and L. Howerton, Dental Radiography: Principles and Techniques, Elsevier, 2012.

[4] B. Cullity and S. Stock, Elements of X-ray Diffraction, Upper Saddle River, NJ: Prentice Hall, 2001.

[5] I. Langmuir, "The electron emission from thoriated tungsten filaments," *Physical Review Journals,* vol. 22, no. 357, 1923.

[6] C. Spindt, "A thin-film field-emission cathode," *Journal of Applied Physics,* vol. 39, p. 3504, 2003.

[7] J. Dobbins III, "Tomosynthesis imaging: At a translational crossroads," *Medical Physics* , vol. 36, no. 6, pp. 1956-1967, 2009.

[8] S. Iijima, "Helical microtubules of graphitic carbon," *Nature,* vol. 354, pp. 56-58, 1991.

[9] Y. Saito, "Structures and Synthesis of Carbon Nanotubes," in *Carbon Nanotube and Related Field Emitters: Fundamentals and Applications*, John Wiley & Sons, 2010, pp. 6-7.

[10] O. Zhou and X. Calderon-Colon, "Carbon Nanotube X-ray Field Emission Technology," in *Carbon Nanotube and Related Field Emitters: Fundamentals and Applications*, John Wiley & Sons, 2010, pp. 418-421.

[11] X. Calderon-Colon, H. Geng, B. Gao, L. An, G. Cao and O. Zhou, "A carbon nanotube field emission cathode with high current density and long term stability," *Nanotechnology*, vol. 20, no. 32, 2008.

[12] D. Bordelon, Z. Zhang, S. Graboski, A. Cox, E. Schreiber, O. Zhou and S. Chang, "A nanotube based elecron microbeam irradiatorfor radiobiology research," *Review of Scientific Instruments,* vol. 79, no. 12, 2008.

[13] Z. Liu, J. Zhang, G. Yang, Y. Cheng, O. Zhou and J. Lu, "Development of a carbon nanotube based microfocus x-ray tube with single focusing electrode," *Review of Scientific Instruments,* vol. 77, no. 054302, 2006.

[14] G. Cao, Y. Lee, R. Peng, Z. Liu, R. Rajaram, X. Calderon-Colon, L. An, P. Wang, T. Phan, S. Sultana, D. Lalush, J. Lu and O. Zhou, "A dynamic micro-CT scanner based on a carbon nanotube field emission x-ray source," *Physics in Medicine and Biology*, vol. 54, no. 8, pp. 2323-2340, 2009.

[15] G. Cao, L. Burk, Y. Lee, X. Calderon-Colon, S. Sultana, J. Lu and O. Zhou, "Prospective-gated cardiac micro-CT imaging of free-breathing mice using carbon nanotube field emission x-ray," *Medical Physics,* vol. 37, no. 10, pp. 5306-5312, 2010.

[16] J. Zhang, G. Yang, Y. Cheng, B. Gao, Q. Qiu, Y. Lee, J. Lu and O. Zhou, "Stationary scanning X-ray source based on carbon nanotube field emitters," *Appl Phys Lett,* vol. 86, no. 184104, 2005.

[17] R. Peng, J. Zhang, X. Calderon-Colon, S. Wang, S. Sultana, P. Wang, G. Yang, S. Chang, J. Lu and O. Zhou, "Design, optimization, and testing of a multi-beam micro-CT scanner based on multi-beam field emission x-ray technology," in *SPIE Medical Imaging*, San Diego, 2010.

[18] S. Wang, X. Calderon-Colon, R. Peng, E. Schreiber, O. Zhou and S. Chang, "A carbon nanotube field emission multipixel x-ray array source for microradiotherapy application," *Applied Physics Letters,* vol. 98, no. 21, 2011.

[19] G. Yang, R. Rajaram, G. Cao, S. Sultana, Z. Liu, D. Lalush, J. Lu and O. Zhou, "Statoinary digital breast tomosynthesis system with a multi-beam field emission x-ray source array," in *SPIE Medical Imaging*, San Diego, 2008.

[20] Z. des Plantes, Selected works of BG Ziedses des Plantes, Amsterdam: Excerpta Medica, 1973.

[21] E. Miller, E. McCurry and B. Hruska, "An infinite number of laminagrams from a finite number of radiographs," *Radiology,* vol. 98, pp. 249-255, 1971.

[22] H. Rosenberg, "Laminography: Methods and applications in oral diagnosis," *J Am Dent Assoc,* vol. 74, pp. 88-96, 1967.

[23] A. Richards, "Dynamic tomography," *Oral Surg Oral Med Oral Path,* vol. 42, no. 5, pp. 685-692, 1976.

[24] D. Grant, "Tomosynthesis: a three-dimensional radiographic imaging technique," *IEEE Trans Biomed Eng,* vol. 19, pp. 20-28, 1972.

[25] A. Tucker, X. Qian, E. Gidcumb, D. Spronk, F. Sprenger, J. Kuo and O. Zhou, "Optimizing configuration parameters of a stationary digital breast tomosynthesis system based on carbon nanotube x-ray sources," in *SPIE Medical Imaging*, San Diego, 2012.

[26] X. Qian, R. Rajaram, X. Calderon-Colon, G. Yang, T. Phan, D. Lalush, J. Lu and O. Zhou, "Design and characterization of a spatially distributed multibeam field emission x-ray source for stationary digital breast tomosynthesis," *Med Phys,* vol. 36, p. 10, 2009.

[27] J. Shan, A. Tucker, Y. Lee, M. Heath, X. Wang, D. Foos, J. Lu and O. Zhou, "Stationary chest tomosynthesis using a CNT x-ray source array: a feasibility study," *Physics in medicine and biology,* vol. 60, no. 1, p. 81, 2014.

[28] A. Tucker, C. Kuzmiak, C. Inscoe, Y. Lee, J. Lu and O. Zhou, "Feasibility of stationary digital breast tomosynthesis as an effective tool for patients with augmentation mammoplasty," in *Proc SPIE 8668*, Orlando, 2013.

[29] X. Qian, A. Tucker, E. Gidcumb, J. Shan, G. Yang, X. Calderon-Colon, S. Sultana, J. Lu, O. Zhou, D. Spronk, F. Sprenger, Y. Zhang, D. Kennedy, T. Farbizio and Z. Jing, "High resolution digital breast tomosynthesis using distributed carbon nanotube x-ray source array," *Medical Physics*, vol. 39, no. 4, pp. 2090-2099, 2012.

[30] A. Tucker, Y. Lee, C. Kuzmiak, J. Calliste, J. Lu and O. Zhou, "Increased microcalcification visibility in lumpectomy specimens using a stationary digital breast tomosynthesis system," in *Proc SPIE 9033*, San Diego, 2014.

[31] A. Terzi, L. Bertolaccini, A. Viti, L. Comello, D. Ghirardo, R. Priotto and M. Grosso, "Lung cancer detection with digital chest tomosynthesis," *Journal of Thoracic Oncology*, vol. 8, no. 6, 2013.

[32] J. Shan, P. Chtcheprov, A. Tucker, Y. Lee, X. Wang, D. Foos, M. Heath, J. Lu and O. Zhou, "Stationary chest tomosynthesis using a CNT x-ray source array," in *SPIE Medical Imaging*, Orlando, 2013.

[33] J. Shan, A. Tucker, Y. Lee, M. Heath, X. Wang, D. Foos, J. Lu and O. Zhou, "Evaluation of imaging geometry for stationary chest tomosynthesis," in *SPIE Medical Imaging*, San Diego, 2014.

[34] A. Mol, L. Gaalaas, E. Platin, A. Tucker, J. Shan, G. Wu, B. Gonzales, J. Lu and O. Zhou, "Intraoral tomosynthesis using carbon nanotube (CNT) X-ray technology: Primary caries detection," in *American Academy of Oral and Maxillorfacial Radiology*, San Francisco, 2015.

[35] J. Shan, A. Tucker, L. Gaalaas, G. Wu, E. Platin, A. Mol, J. Lu and O. Zhou, "Stationary intraoral digital tomosynthesis using a carbon nanotube x-ray source array," *Dentomaxillofacial Radiology*, vol. 44, no. 20150098, 2015.

[36] C. Inscoe, G. Wu, D.-E. Souliouti, E. Platin, A. Mol, L. Gaalaas, M. Regan Anderson, A. Tucker, S. Boyce, J. Shan, B. Gonzales, J. Lu and O. Zhou, "Stationary intraoral tomosynthesis for dental imaging," in *SPIE Medical Imaging*, Orlando, 2017.

[37] R. Bagramian, F. Garcia-Godoy and A. Volpe, "The global increase in dental caries. A pending public health crisi.," *American Journal of Dentistry*, vol. 21, no. 1, pp. 3-8, 2009.

[38] J. Bader, D. Shugars and A. Bonito, "Systematic reviews of selected dental caries diagnostic and management methods," *Journal of Dental Education*, vol. 65, no. 10, pp. 960-968, 2001.

[39] A. Wenzel, "Bitewing and digital bitewing radiography for detection of caries lesions," *Journal of Dental Research*, vol. 83(suppl 1), pp. C72-75, 2004.

[40] A. Tamse, Z. Fuss, J. Lustig and J. Kaplavi, "An evaluation of endodontically treated vertically fractured teeth," *Journal of Endodontics,* vol. 25, no. 7, pp. 506-508, 1999.

[41] E. Rosen, I. Tsesis, A. Tamse, L. Bjorndal, S. Taschieri and N. Givol, "Medico-legal aspects of vertical root fractures in root filled teeth," *International Endodontic Journal,* vol. 45, no. 1, pp. 7-11, 2012.

[42] L. Gaalaas, D. Tyndall, A. Mol, E. Everett and A. Bangdiwala, "Ex vivo evaluation of new 2D and 3D dental radiographic technology for detecting caries," *Dentomaxillofacial Radiology,* vol. 45, no. 3, 2016.

[43] R. Webber, R. Horton, T. Underhill, J. Ludlow and D. Tyndall, "Comparison of film, direct digital, and tuned-aperture computed tomography images to identify the location of crestal defects around endosseous titanium implants," *Oral Surg Oral Med Oral Path,* vol. 81, no. 4, pp. 480-490, 1996.

[44] R. Webber and J. Messura, "An in vivo comparison of diagnostic information obtained from tuned-aperture computed tomography and conventional dental radiographic imaging modalities," *Oral Surg Oral Med Oral Path Oral Radiol Endod,* vol. 88, pp. 239-247, 1999.

[45] M. Nair, U. Nair, A. Seyedain, R. Gassner, N. Piesco, M. Mooney, S. Ganta and S. Agarwal, "Correlation of tuned aperture computed tomography with conventional computed tomography for evaluation of osseous healing in calvarial defects," *Oral Surg Oral Med Oral Path Oral Radiol Endod,* vol. 103, pp. 267-273, 2007.

[46] R. Webber, R. Horton, D. Tyndall and J. Ludlow, "Tuned-aperture computed tomography (TACT). Theory and application for three dimensional dento-alveolar imaging," *Dentomaxillofacial Radiology,* vol. 26, pp. 53-62, 1997.

[47] Y. Harase, K. Araki and T. Okano, "Diagnostic ability of extraoral tuned aperture computed tomography (TACT) for impacted third molars," *Oral Surg Oral Med Oral Path Oral Radiol Endod,* vol. 100, pp. 84-91, 2005.

[48] M. Nair, R. Webber and M. Johnson, "Comparative evaluation of Tuned Aperture Computed Tomography(R) for the detection of mandibular fractures," *Dentomaxillofacial Radiology,* vol. 29, pp. 297-301, 2000.

[49] M. Nair, U. Nair, H.-G. Grondahl and R. Webber, "Accuracy of tuned aperture computed tomography in the diagnosis of radicular fractures in non-restored maxillary anterior teeth- an in vitro study," *Dentomaxillofacial Radiology,* vol. 31, pp. 299-304, 2002.

[50] M. Nair and U. Nair, "Detection of artificially induced vertical radicular fractures using Tuned Aperture Computed Tomography," *European Journal of Oral Sciences,* vol. 109, no. 6, pp. 375-379, 2001.

[51] M. Nair and J. Bezik, "Tuned-aperture computed tomography for detection of induced mid-buccal/lingual alveolar bone defects," *Journal of Periodontology,* vol. 77, pp. 1833-1838, 2006.

[52] M. Nair, D. Tyndall, J. Ludlow and K. May, "Tuned aperture computed tomography and detection of recurrent caries," *Caries Research,* vol. 32, pp. 23-30, 1998.

[53] Y. Harase, K. Araki and T. Okano, "Accuracy of extraoral tuned aperture computed tomography (TACT) for proximal caries detection," *Oral Surg Oral Med Oral Path Oral Radiol Endod,* vol. 101, pp. 791-796, 2006.

[54] M. Nair and D. Tyndall, "The effect of restorative material and location on the detection of simulated recurrent caries. A comparison of dental film, direct digital radiography and tuned aperture computed tomography," *Dentomaxillofacial Radiology,* vol. 27, pp. 80-84, 1998.

[55] X. Shi and P. Han, "Tuned-aperture computed tomography for detection of occlusal caries," *Dentomaxillofacial Radiology,* vol. 30, pp. 45-49, 2001.

[56] D. Tyndall, R. Clifton, R. Webber, J. Ludlow and R. Horton, "TACT imaging of primary caries," *Oral Surg Oral Med Oral Path Oral Radiol Endod,* vol. 84, p. 214, 1997.

[57] L. Li, Z. Chen, Z. Zhao and D. Wu, "X-ray intra-oral tomosynthesis for quasi-three-dimensional imaging: system, reconstruction algorithm, and experiments," *Optical Engineering,* vol. 52, no. 1, p. 013201, 25 October 2013.

[58] C. Ziegler, M. Franetzki, T. Denig, J. Muhling and H. Hassfeld, "Digital tomosynthesis - experiences with a new imaging device for the dental field," *Clinical Oral Investigations,* vol. 7, pp. 41-45, 16 September 2003.

[59] M. Cho, H. Kim, H. Youn and S. Kim, "A feasibility study of digital tomosynthesis for volumetric dental imaging," *Journal of Instrumentation,* vol. 7, 2012.

[60] M. Franetzki, W. Guenther and J. Ploetz, "X-ray diagnostics installation". US Patent 5,598,454, 28 January 1997.

[61] O. Zhou, J. Lu, J. Shan, A. Tucker, P. Chtcheprov, E. Platin, A. Mol, L. Gaalaas and G. Wu, "Intraoral tomosynthesis systems, methods, and computer readable media for dental imaging". United States of America Patent 9782136, 10 October 2017.

[62] NCT02873585, "ClinicalTrials.gov," NIH, 16 June 2017. [Online]. Available: https://clinicaltrials.gov/ct2/show/NCT02873585. [Accessed 1 August 2017].

[63] B. Gonzales, D. Spronk, Y. Cheng, A. Tucker, M. Beckman, O. Zhou and J. Lu, "Rectangular fixed-gantry CT prototype: Combining CNT X-ray sources and accelerated compressed sensing-based reconstruction," *IEEE Access,* vol. 2, pp. 971-981, 2014.

[64] X. Pan, E. Sidky and M. Vanniew, "Why do commercial CT scanners still employ traditional, filtered back-projection for image reconstruction?," *Inverse Problems,* vol. 25, no. 12, p. 123009, 2009.

[65] IEC, "International Standard 60336," IEC, Geneva, 2005.

[66] E. Samei, M. Flynn and D. Reimann, "A method for measuring the presampled MTF of digital radiographic systems using an edge test device," *Medical Physics,* pp. 102-113, 1998.

[67] N. C. A. Code, "10A NCAC 15 .0604 General requirements for all diagnostic systems," 2015.

[68] S. Mauriello, E. Platin, A. Broome, C. Inscoe, A. Mol and J. Patel, "Use of Stationary Digital Intraoral Tomosynthesis (sIOT) for Bitewing Radiography," in *IADR,* London, 2018.

[69] M. Yester, G. Barnes and M. King, "Experimental measuremements of the scatter reduction obtained in mammography with a scanning multiple slit assembly," *Medical Physics,* vol. 8, pp. 158-162, 1981.

[70] Z. Jing, W. Huda and J. Walker, "Scattered radiation in scanning slot mammography," *Medical Physics,* vol. 25, pp. 1111-1117, 1998.

[71] J. Boone, J. Seibert, C. Tang and S. Lane, "Grid and slot scan scatter reduction in mammography: Comparison using monte carlo techniques," *Radiology,* vol. 222, pp. 519-527, 2002.

[72] J. Park, E. Franken, M. Garg, L. Fajardo and L. Niklason, "Breast Tomosynthesis: Present Considerations and Future Applications," *RadioGraphics,* vol. 27, pp. 231-240, 2007.

[73] S.-H. Chou, G. Kicska, S. Pipavith and G. Reddy, "Digital Tomosynthesis of the Chest: Current and Emerging Applications," *RadioGraphics,* vol. 34, pp. 359-372, 2014.

[74] Philips Healthcare, "Photon Counting White Paper," 2011. [Online]. Available: www.philips.com/healthcare.

[75] M. Aslund, B. Cederstron, M. Lundqvist and M. Danielsson, "Scatter rejection in multislit digital mammography," *Medical Physics,* vol. 33, p. 933, 2006.

[76] G. Barnes, "Contrast and scatter in x-ray imaging," *RadioGraphics,* vol. 11, pp. 307-323, 1991.

[77] E. Samei, J. Lo, T. Yoshizumi, J. Jesneck, J. Dobbins III, C. Floyd Jr, H. McAdams and C. Ravin, "Comparative scatter and dose performance of slot-scan and full-field digital chest radiography systems," *Radiology,* vol. 235, pp. 940-949, 2005.

[78] S. Feng and I. Sechopoulos, "A software-based x-ray scatter correction method for breast tomosynthesis," *Medical Physics,* vol. 38, p. 6643, 2011.

[79] S. Feng, C. D'Orsi, M. Newell, R. Seidel, B. Patel and I. Sechopoulos, "X-ray scatter correction in breast tomosynthesis with a precomputed scatter map library," *Medical Physics,* vol. 41, no. 3, 2014.

[80] D. Zhang, X. Li and B. Liu, "Multi-resolution analysis of scatter in digital breast tomosynthesis imaging," in *SPIE Medical Imaging*, Orlando, 2013.

[81] X. Liu, C. Shaw, M. Altunbas and T. Wang, "A scanning sampled measurement (SSM) technique for scatter measurement and correction in cone beam breast CT," *Medical Physics,* vol. 32, p. 2093, 2005.

[82] T. Niu and L. Zhu, "Scatter correction for a full-fan volumetric CT using a stationary beam blocker in a single full scan," *Medical Physics,* vol. 38, p. 6027, 2011.

[83] K. Yang, G. Burkett Jr. and J. Boone, "An object-specific and dose-sparing scatter correction approach for a dedicated cone-beam breast CT system using a parallel-hole collimator," in *SPIE Medical Imaging*, San Diego, 2012.

[84] I. Sechopoulos, "X-ray scatter correction method for dedicated breast computed tomography," *Medical Physics,* vol. 39, p. 2896, 2012.

[85] K. Yang, G. Burkett Jr. and J. Boone, "A breast-specific, negligible-dose scatter correction technique for dedicated cone-beam breast CT: a physics-based approach to improve Hounsfield Unit accuracy," *Physics in Medicine and Biology,* vol. 59, p. 6487, 2014.

[86] C. Inscoe, A. Tucker, O. Zhou and J. Lu, "Demonstration of a scatter correction technique in digital breast tomosynthesis," in *SPIE Medical Imaging*, Orlando, 2013.

[87] C. Inscoe, G. Wu, J. Shan, Y. Lee, O. Zhou and J. Lu, "Low dose scatter correction for digital chest tomosynthesis," in *SPIE Medical Imaging*, Orlando, 2015.

[88] G. Wu, C. Inscoe, J. Calliste, J. Shan, Y. Lee, O. Zhou and J. Lu, "Estimating scatter from sparsely measured primary signal," *Journal of Medical Imaging,* vol. 4, no. 1, 2017.

[89] C. Puett, C. Inscoe, Y. Lee, O. Zhou and J. Lu, "A phantom-based study exploring the effects of different scatter correction approaches on the reconstructed images generated by contrast-enhanced stationary digital breast tomosynthesis," *Journal of Medical Imaging,* vol. 5, no. 1, 2018.